AD-A187 053 A COMPARISON BETWEEN THEORY AND EXPERIMENT FOR THE YAW MOMENT INDUCED BY A..(U) ARMY BALLISTIC RESEARCH LAB ABERDEEN PROVING GROUND MD W P D'AMICO DEC 86 1/1

UNCLASSIFIED BRL-MR-3577 1L162618AH80 F/G 19/1 NL

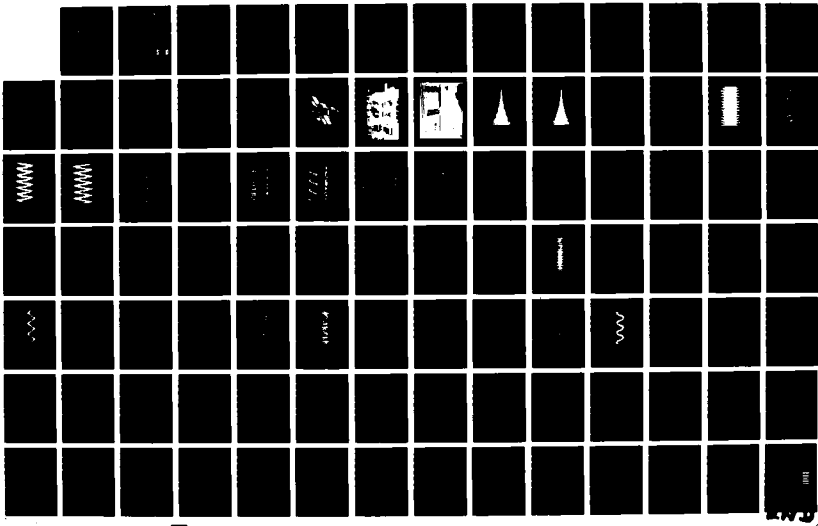

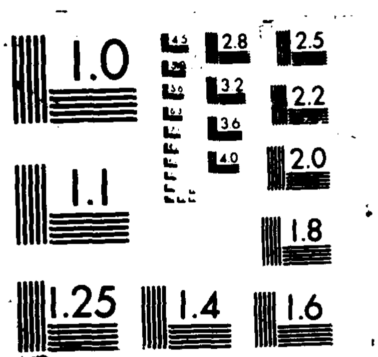
1.0
2.8
2.5
3.2
2.2
3.6
2.0
4.0
1.1
1.8
1.25
1.4
1.6

MEMORANDUM REPORT BRL-MR-3577

A COMPARISON BETWEEN THEORY AND EXPERIMENT FOR THE YAW MOMENT INDUCED BY A LOOSE INTERNAL PART

WILLIAM P. D'AMICO, JR.

OCTOBER 1987

APPROVED FOR PUBLIC RELEASE; DISTRIBUTION UNLIMITED.

US ARMY BALLISTIC RESEARCH LABORATORY
ABERDEEN PROVING GROUND, MARYLAND

UNCLASSIFIED

SECURITY CLASSIFICATION OF THIS PAGE

REPORT DOCUMENTATION PAGE

Form Approved OMB No 0704-0188 Exp. Date Jun 30, 1986

1a. REPORT SECURITY CLASSIFICATION UNCLASSIFIED	1b. RESTRICTIVE MARKINGS
2a. SECURITY CLASSIFICATION AUTHORITY	3. DISTRIBUTION/AVAILABILITY OF REPORT Approved for public release; distribution is unlimited.
2b. DECLASSIFICATION/DOWNGRADING SCHEDULE	
4. PERFORMING ORGANIZATION REPORT NUMBER(S) BRL-MR-3577	5. MONITORING ORGANIZATION REPORT NUMBER(S)
6a. NAME OF PERFORMING ORGANIZATION U.S. Army Ballistic Research Laboratory 6b. OFFICE SYMBOL (If applicable) SLCBR-LF	7a. NAME OF MONITORING ORGANIZATION
6c. ADDRESS (City, State, and ZIP Code) Aberdeen Proving Ground, MD 21005-5066	7b. ADDRESS (City, State, and ZIP Code)
8a. NAME OF FUNDING/SPONSORING ORGANIZATION U.S. Army Ballistic Research Laboratory 8b. OFFICE SYMBOL (If applicable) SLCBR-DD-T	9. PROCUREMENT INSTRUMENT IDENTIFICATION NUMBER
8c. ADDRESS (City, State, and ZIP Code) Aberdeen Proving Ground, MD 21005-5066	10. SOURCE OF FUNDING NUMBERS PROGRAM ELEMENT NO. 62618A PROJECT NO. 1L162618AH80 TASK NO. MG(L) WORK UNIT ACCESSION NO

11. TITLE (Include Security Classification)
A COMPARISON BETWEEN THEORY AND EXPERIMENT FOR THE YAW MOMENT INDUCED BY A LOOSE INTERNAL PART

12. PERSONAL AUTHOR(S)
D'Amico, William P.

13a. TYPE OF REPORT	13b. TIME COVERED	14. DATE OF REPORT (Year, Month, Day)	15. PAGE COUNT
Final	FROM ______ TO ______	1986 December	98

16. SUPPLEMENTARY NOTATION
This report supersedes IMR 825, dated September 1984.

17. COSATI CODES			18. SUBJECT TERMS (Continue on reverse if necessary and identify by block number)
FIELD	GROUP	SUB-GROUP	Flight Stability
01	01		Gyroscope
			Loose Payload

19. ABSTRACT (Continue on reverse if necessary and identify by block number) (bja)

Spin stabilized projectiles often employ internal parts that are loose. Typical examples are safety mechanisms within fuzes, payload components, or submunitions. A series of tests were conducted where a loose internal part was driven by the rotor of a freely-gimballed gyroscope. The motion of the loose part is not identical to that of the gyroscope and will cause the gyroscope yaw to grow. The gyroscope yaw history and the orbital motion of the loose part were measured to determine the phase angle between the motion of the loose part and the yawing motion of the gyroscope. The experimental data were used as input parameters to a theory that predicts moments (and, therefore, the yaw growth rate) induced by a loose internal part. Where the assumptions of the theory were appropriately modeled by the experiment, comparisons of theoretical and experimental yaw growth rates were consistent.

20. DISTRIBUTION/AVAILABILITY OF ABSTRACT ☐ UNCLASSIFIED/UNLIMITED ☒ SAME AS RPT ☐ DTIC USERS	21. ABSTRACT SECURITY CLASSIFICATION UNCLASSIFIED
22a. NAME OF RESPONSIBLE INDIVIDUAL William P. D'Amico, Jr.	22b. TELEPHONE (Include Area Code) (301)-278-2926 22c. OFFICE SYMBOL SLCBR-LF-A

DD FORM 1473, 84 MAR

83 APR edition may be used until exhausted
All other editions are obsolete

SECURITY CLASSIFICATION OF THIS PAGE
UNCLASSIFIED

ACKNOWLEDGMENTS

The author is indebted to Mr. Geoffrey Markovic for his patience and dedication in the reduction of the raw and final data. Most of the plots and data files used for plotting were generated by Mr. Markovic. Mr. Steven Kushubar provided excellent support on the Launch and Flight Division, Ballistic Research Laboratory (BRL), Aberdeen Proving Ground, Maryland, VAX 11/780. Finally, without the cooperation and dedication of Messrs. R. Cornell and T. Morgan of Lawrence Livermore National Laboratories (LLNL), Livermore, California, and Mr. A. Hodapp of Sandia National Laboratories (SNL), Albuquerque, New Mexico, this entire experimental program would not have been a success.

TABLE OF CONTENTS

LIST OF FIGURES

LIST OF FIGURES (Continued)

LIST OF FIGURES (Continued)

I. INTRODUCTION

1. OBJECTIVE

Modern projectile systems typically have fuze, submunition, or payload components that are not rigidly fixed. For example, small caliber ammunition often employ fuzes with safe and arming devices that utilize a spherical rotor. This rotor can reduce the fast-mode precessional damping characteristics of a projectile system.[1-3] In another case, an artillery projectile experienced high yaw levels and large spin decays.[4] Presently, improved convention munitions (ICM) systems carry base-ejected submunitions and canisters. These payloads must be assembled and keyed with the projectile body, but small amplitude, internal motions are still possible.

Analytical investigations by Murphy[5-6] have explained much of the phenomena that was observed in References 1-4, and he has provided fundamental models that predict the magnitudes of the yaw and spin moments induced by loose internal parts. Experimental tests using a spin fixture were performed by Bush to determine the despin moments produced by a loose ring on a circular shaft.[7] The present report describes a series of tests where the motions of a loose internal part and the supporting gyroscope were measured. Phase and orbital data were used to compare theory and experiment.

2. BACKGROUND

The model suggested by Murphy assumes that the motion of the projectile has both slow and fast precessional modes. These two motions are decoupled and treated in a quasi-linear fashion. For practical applications, only the fast precessional mode is destabilized (this has been verified with yawsonde-determined flight data). If the motion of the loose part is assumed, then the response of the projectile system can be determined. Two types of motion for the loose part were considered: (1) a forced precession about its own spin axis at the fast frequency of the projectile, or (2) a circular motion of the center of mass of the loose part at the fast frequency of the projectile.

If the loose part center-of-mass (cm) motion has a radius ε and a phase angle ϕ_ε with respect to the angle-of-attack plane and the precessional motion has a cone angle γ and a phase angle ϕ_γ with respect to the angle-of-attack plane, then the relations for the fast precessional frequency ($\dot\phi_1$), the fast precessional damping (λ_1), and the change in the spin moment (ΔM_{spin}) are given below:[5]

$$\dot\phi_1/\dot\phi_{1r} = 1 - C_1/[K_1\ (2\ I_t\ \dot\phi_{1r} - L_{a0})] \quad (1)$$

$$(\lambda_1 - \lambda_t)\ K_1 = \dot\phi_1\ S_1/(2\ I_t\ \dot\phi_1 - L_{a0}) \quad (2)$$

$$\Delta M_{spin} = -\dot{\phi}_1 K_1 S_1 \quad (3)$$

$$L_{a0} = I_{ab}\, p + I_{ac}\, p_c \quad (4)$$

$$S_1 = (I_{ac}\, p_c - I_{tc}\, \dot{\phi}_1)\, \gamma \sin \phi_\gamma - m_c\, x_c\, \dot{\phi}_1\, \varepsilon \sin \phi_\varepsilon \quad (5)$$

$$C_1 = (I_{ac}\, p_c - I_{tc}\, \dot{\phi}_1)\, \gamma \cos \phi_\gamma - m_c\, x_c\, \dot{\phi}_1\, \varepsilon \cos \phi_\varepsilon \quad (6)$$

The model also assumes that the yawing motion of the projectile has an amplitude that is larger than the orbital motion of the loose part, i.e., $K_1 > \max(\gamma, \varepsilon/x_c)$. It is important to note that the initial or starting motion for the projectile or the loose part is not considered within this model. Also, if the motion of the loose part is not at the precessional frequency of the projectile, then a prediction of yaw or spin moments is not possible. The amplitudes and phase angles of the two types of assumed motion must be provided as inputs to the theory. If these are not known, then nominal values must be chosen. Previously, maximum physical clearances or tolerances were normally selected to determine the orbits, while phase angles of 90-45 degrees were assumed.

3. INITIAL CONCEPTS FOR THE GYROSCOPE EXPERIMENT

For the purposes of this experiment, it is assumed that a freely gimballed gyroscope will produce angular motions that realistically simulate the yawing motion of a projectile about its trajectory. The loose part is partially restrained within the gyroscope and will be referred to as the PRIM (partially restrained internal member). The motion of the PRIM within a gyroscope may have many components, but logically it will attempt to move independently as a gyroscope within a gyroscope or to respond as a forced oscillator to the motion of the gyroscope. Assuming the PRIM is forced to rotate at the spin frequency of the gyroscope, then the following types of motion can exist:

a. Precessional motion based upon the PRIM inertial properties;

b. Circular motion of the PRIM cm at the spin frequency;

c. Precessional motion of the PRIM at the gyroscope precession frequency;

d. Circular motion of the PRIM cm at the gyroscope precession frequency.

It is important to recall that the theoretical model[5] only considers the last two types of motions. This is reasonable, since only motions of the PRIM at the precessional frequencies of the gyroscope (or a projectile) would destabilize the precessional (or yawing) motion. PRIM motion at other frequencies would require subharmonic or ultraharmonic responses.[8] During the course of the gyroscope experiments, these four types of behavior were observed.

4. DESCRIPTION OF GYROSCOPE

A freely gimballed gyroscope was used as a test platform to conduct PRIM experiments. Figure 1 shows a schematic of the PRIM/gyroscope (without support base), important instrumentation locations, and a physical coordinate system. Flexural pivots were used within the gimbal system and were instrumented with strain gages. The yaw amplitude was calibrated as a function of the output voltage of a bridge circuit. The orbit of the PRIM was monitored by non-contact inductive sensors (commonly called displacement transducers) that were mounted within the inner gimbal frame. The shaft and PRIM were driven by a DC motor, which was mounted below the inner gimbal. The spin of the shaft and PRIM remained constant during a data trial. A tachometer system was available for speed control, but it was not used. Even under this open loop condition, despin of the rotor/PRIM assembly was not observed during the data trials. The precessional frequency of the gyroscope was controlled through the placement of non-spinning weights on a stem that was mounted to the top of the inner gimbal (not shown in Figure 1). The position of these weights determined the transverse moment of inertia of the gyroscope (I_t). The fast precessional frequency of the gyroscope was controlled by selection of I_t. The axial moment of inertia (I_a) was a constant since all of the various shafts were similar. The experiment was conceptually designed in a joint effort by Lawrence Livermore National Laboratories (LLNL), Livermore, California, Sandia National Laboratory (SNL), Albuquerque, New Mexico, and the Ballistic Research Laboratory (BRL), Aberdeen Proving Ground, Maryland. The hardware and instrumentation for the PRIM experiments were built and assembled by LLNL, while the tests were conducted by LLNL in cooperation with BRL. A large series of tests were performed;[9-10] however, this report will primarily consider comparisons between round shaft experiments and theory. In the present experiments, the orbital motion and phase angle were measured directly. These, as well as other measured quantitites, were used as inputs to the theory to provide a comparison between experiment and theory. Figures 2 and 3 show the actual gyroscope/PRIM experimental set-up at the BRL. All data were recorded in an analog form for post processing of data.

The damping of the flexural pivots within the gimbals and the location of the cm of the gyroscope produces a motion that is dominated by the fast precessional mode ($\dot{\phi}_1/p$ is approximately I_a/I_t). During the course of the experiments some slow mode precession was observed, but this motion was rapidly damped when the fast precessional mode became unstable. Hence, for simplicity, the terminology "fast precession" will be abbreviated to "precession" or "yaw."

II. DATA REDUCTION TECHNIQUES

The length and character of the data records required the use of both analog and digital reduction procedures. Often, data were reduced by two independent techniques to provide additional confidence.

1. YAW DATA

The output of the flexural pivot/strain gage system gave a continuous projection of the yaw in the X and Y planes. The data in the Y plane were not reliable due to mechanical vibrations in the gimbals (probably excited by the motion of the PRIM). Normally, the data in the X plane (data from sensor SX) were reliable and were used. A series of data trials were conducted where the PRIM was fixed to the shaft. These tare runs were taken at various combinations of spin and precession frequencies to determine the natural yaw damping (λ_t) and the yaw frequency ($\dot{\phi}_{1r}$) of the total gyroscope/PRIM assembly when all the components were fixed. These tare data are required as inputs to Equations (1) and (2).

Both the tare and PRIM yaw data were reduced to obtain a log decrement type of growth rate. The yaw frequency was determined by the average number of zero crossings over several seconds of data. The data have not been processed to identify slow variations within the yaw frequency. In this form the yaw growth rate has units of 1/s. The growth rate data will be tabulated in this form, but could be scaled by either the precessional or spin frequencies to obtain a dimensionless form. A typical tare data run showing raw SX data, high pass filtered SX data, and a tare damping reduction are shown in Figures 4, 5, and 6.

2. PRIM MOTION DATA

The orbit of the PRIM was continuously monitored by four displacement transducers, DX1 and DX2 in the X-plane and DY1 and DY2 in the Y-plane (as shown in Figure 1). Sensors could also be mounted in the top support of the inner gimbal, but these positions were not normally utilized. Data from the displacement sensors were of very high quality and clearly indicated the motion of the PRIM. Typical outputs from a displacement transducer will be shown and discussed in following sections.

A primary objective of this PRIM experiment was to determine the phase angle between the yawing motion of the gyroscope and the motion of the PRIM. This phase angle was defined in Reference 5 in terms of the two types of motion assumed in the model (phase angles for a precession of the PRIM (ϕ_γ) or for a cm motion of the PRIM (ϕ_ε)). Using these definitions, the natural phase relationships of all of the data transducers can be determined for the special case of precession (no cm motion) when $\phi_\gamma = 0$. These inherent phase delays must be used to correct the raw data and to properly identify ϕ_γ. A detailed discussion of the natural phase angles is given in Appendix A.

III. GYROSCOPE TEST RESULTS

1. DESCRIPTION OF PRIM PARTS AND TEST CONDITIONS

A large test matrix was performed. A sectioned view of the inner gimbal, PRIM, shaft, and transducers is shown in Figure 7. Shafts with round and octagonal hubs were tested (the upper hubs of all shafts were round). Six shafts were fabricated with the following radial clearances (stated in inches) between the PRIM and the shaft hubs: round-0.005, 0.010, 0.015 and octagonal-0.005, 0.010, and 0.020. (The 0.020 octagonal shaft was not tested.) LLNL personnel conducted a few tests with Belville washers (essentially very stiff springs) on the upper hub of the shaft (see Figure 7). Also, LLNL tested shafts with a combined radial offset and radial clearance. This report only addresses the round shaft tests and the 0.005 octagonal shaft test. A counterweight was used on the gyroscope and was located at three positions, nominally called top (T), middle (M), and bottom (B). Spin frequencies were typically in the 85 to 60 Hz range. The physical characteristics of the gyroscope/PRIM parts were measured at the BRL Transonic Range and are given in Table 1. The overall length of the PRIM is 5 inches, and the center of mass of the PRIM was essentially at the geometric center. Note that the PRIM is almost an inertial sphere, i.e., $I_{aPRIM}/I_{tPRIM} = 0.850$. The differences between I_x and I_y were assumed to be small and the gyroscope was assumed to have a single transverse moment of inertia ($I_t=(I_x+I_y)/2$) for a particular counterweight position. Tare data were taken to determine the natural damping characteristics of the system and are discussed in Appendix B.

TABLE 1. Physical Characteristics for the Gyroscope/PRIM Test.

Transverse Moments of Inertia of Fixed Parts - I_t ($kg \cdot cm^2$)

Counterweight Position	I_x	I_y
TOP	1,935	1,879
MIDDLE	1,777	1,717
BOTTOM	1,613	1,559

Axial Moment of Inertial of Fixed Parts: $I_a = 0.737\ kg \cdot cm^2$

(Motor Armature & Typical Shaft)

Transverse Moment of Inertia of the PRIM: $I_{tPRIM} = 87.1\ kg \cdot cm^2$

Axial Moment of Inertial of the PRIM: $I_{aPRIM} = 74.0\ kg \cdot cm^2$

The ratio of the rigid body (or tare) coning and spin frequencies ($\dot{\phi}_{1r}/p$) should be approximately equal to I_a/I_t for a small gravity moment. For the counterweight located at the middle position, $I_a/I_t = 0.0429$. Measured values of $\dot{\phi}_{1r}$ and p (for $p > 70$ Hz) yielded an average value for $\dot{\phi}_{1r}/p$ of 0.0435. Hence, the gyroscope/fixed-PRIM model is essentially independent of gravity effects.

2. ROUND SHAFT PHASE DATA

Appendix C provides a listing of the experiment run names and detailed descriptions of the experimental set-up and conditions, i.e., shaft radial clearances, spin rates, coning frequencies, etc. Figures and written discussions within the report will normally reference the experiment number. Appendix C should be used as a cross reference to establish all pertinent run conditions.

The round shaft data showed three distinct types of behavior. Only one of these types of motion is reasonably approximated by the theory. When the gyroscope was released at zero yaw with no disturbance, the motion of the PRIM was a combination of both a precessional motion controlled by its own ratio of moments of inertia and a center of mass (cm) motion at the spin rate. Very little of the total motion was at the gyroscope yaw frequency. Under these conditions, the dominant PRIM motion is that of a free gyroscope. The fast precessional frequency of the PRIM ($\dot{\phi}_{1PRIM}/\dot{\phi}$) is approximately equal to I_{aPRIM}/I_{tPRIM}. It would not be anticipated that this initial PRIM motion would provide a destabilizing torque to the gyroscope since very little of the motion is at the gyroscope yaw frequency. However, in many instances, the gyroscope yaw did grow. At intermediate yaw levels, the response of the PRIM was essentially random and aperiodic. A transition between a free oscillator and a forced oscillator was in progress. When the yaw of the gyroscope was well established, the PRIM motion was then dominated by a precessional motion at the gyroscope coning frequency. During this final stage of behavior, a component of the motion at the spin frequency was still present. For comparisons between data and experiment, it will be necessary to separate the individual components by frequency. Only the motion component (phase and amplitude) at the gyroscope yaw frequency should be compared to the theory.

Figures 8a, 8b, and 8c show some of the important features of typical displacement transducer data. Figure 8a shows DY2 versus time. Note that the peak-to-peak (PTP) amplitude slightly exceeds 0.010 inch. This corresponds to the diametrical clearance (twice the radial clearance of 0.005 in) plus a response due to the flats that were machined on the PRIM end caps. These data were low pass filtered (10 Hz cut frequency) and are shown in Figure 8b. Note that the amplitude of the motion is quite small (PTP magnitude of 0.0003 in). The data in Figure 8c are at a larger yaw amplitude (longer time) for the same data trial. The data in Figure 8c are typical of the final stage of motion. Raw (dashed line) and low passed (solid line) data are superimposed to demonstrate that the digital filtering that was utilized did not introduce phase delay.

When examining the data in Figure 8c, it is important to note that the amplitude of the PRIM motion at the yaw frequency was only 65% of the PTP motion. This is the only frequency component considered in the theory and previously the amplitude of this component was simply equated to the total radial clearance. This is clearly not the case, and all round shaft data indicated that roughly 75% of the total PRIM motion was at the yaw frequency (a similar trend was demonstrated for the octagonal shafts).

When the PRIM motion had a frequency and form that was representative of the assumptions of the theory, a phase angle was determined. It is necessary to determine from the displacement data whether a precession or a cm motion of the PRIM is present. If a cm motion exists (at a frequency of $\dot{\phi}_1$), then the displacement data from DX1 and DX2 (or DY1 and DY2) would be in phase and would not follow the conventions established in Appendix A. Figures 8c and 8d show data for DY1 and DY2 (raw and low pass filtered). These data are out of phase by 180 degrees and indicate that the motion of the PRIM at this time is precessional. The measured ϕ_Y values were typically between 150 and 170 degrees. Figures 9a and 9b show the variation of phase angle versus yaw amplitude for several of the round shaft experiments. Note that the theory does not account for variable phase angles or changes in the PRIM radial orbit. These quantities are assumed to be steady.

3. OCTAGON SHAFT PHASE DATA

The character of the octagon shaft data was dramatically different from the round shaft data. The motion of the PRIM was not centered about the PRIM cm. This can be easily observed from the raw analog data at DX1 and DX2. Figure 10a, taken at an early time (small yaw amplitude), shows a slightly periodic motion for both transducers. Clearly, the data are only vaguely similar in form, while they are drastically different in amplitude (PTP amplitude for DX1 is 1.5 volts, while PTP amplitude for DX2 is 0.5 volts). Figure 10b shows the same sensors at a later time (larger amplitude). The outputs are not similar at all in either character or amplitude. The top of the PRIM, which has a round hub, has a precessional motion. However, the bottom of the PRIM, which has the octagonal hub, primarily has a cm motion at the spin frequency. It could be assumed that the octagon hub acted like a hinge point and that the precessional motion of the PRIM is centered about the lower hub. This would reduce the cant angle, ϕ_Y, by a factor of two since the cm of the PRIM is at its geometric center. The orbital motion should be determined using data from three displacement transducers. However, using the same methods as in the round shaft experiments, data from DX1 or DY1 will be used to determine orbit and phase data. The phase angles for the 0.005 in octagonal shaft were always less than 90 degrees and usually below 30 degrees. This was determined by using data from DX1, since DX2 had little or no precessional motion. Figure 11 shows the phase angle, ϕ_Y, versus the yaw amplitude for the octagon shaft.

IV. COMPARISONS BETWEEN EXPERIMENT AND THEORY

A realistic validation of the theory can be conducted by using the experimentally determined values of yaw growth rate, phase angle, and cant angle. Such comparisons have not been previously made and will be explained here. Equations (1) and (2) are restricted to a precessional motion of the PRIM. Appendix C contains a listing of all experimental parameters that were directly measured or derived from the raw data. These data were used to evaluate the theory.

Within Equation (2), the yaw growth rate and tare damping are combined into a single quantity and identified as the experimental yaw growth rate. The other remaining term within Equation (2) is essentially the theoretical estimation of yaw growth rate (although it does require experimentally determined values of phase angle and cant angle) and is labeled the theoretical yaw growth rate. The experimental yaw growth rate can be nondimensionalized by the coning frequency. The dimensionless growth rates will be identified as ε_{exp} and ε_{theory}. The quantity $2\pi\varepsilon_{exp}$ (or $2\pi\varepsilon_{theory}$) is approximately the fractional change in K_1 (the yaw amplitude) for each cycle of the yaw frequency, $\dot{\phi}_1$. The loose part also affects the yaw frequency of the gyroscope/PRIM system. The change in the yaw frequency is presented as a ratio of the gyroscope/PRIM frequency to the tare coning frequency, which is considered to be the rigid body coning frequency. As was the case with the yaw growth rate, the terms in Equation (1) are separated into experimental and theoretical values and presented as a ratio of the coning frequencies, $\dot{\phi}_1/\dot{\phi}_{1r}$.

Comparisons of experiment and theory are provided in Appendices E-I and E-II. Comparisons were made at discrete times during a data run. Often the motion of the PRIM was not that which was assumed within the theory (under these circumstances asterisks are shown in the time column within Appendix E) but comparisons between data and theory are provided for reference. Comparisons for yaw growth rate (labeled growth rate and given in ε_{exp} and ε_{theory} formats) between experiment and theory are plotted in Figures 12a-c. The theoretical and experimental values for yaw growth rate were plotted as open and closed symbols, respectively. At early times, comparisons should be poor since the assumptions of the theory are not met by the experiment. Any agreement at these times should be considered as fortuitous. Also, comparisons with the octagonal were made simply to indicate if large differences would occur.

Primarily, comparisons will be made between experiment and theory for yaw growth rates. These comparisons are critically dependent upon the measurement of the phase angle. The coordinate system established within Reference 5 was centered upon the missile symmetry axis, while the coordinate system of the PRIM experiments was centered about the vertical (or for the flight case, the trajectory). However, in both theory and experiment, the relative angle between the angle of attack plane and the cant plane of the loose part is the same. Orientation of the transducers indicated that a phase angle of nearly 180 degrees would orient the PRIM away from the vertical (or the trajectory) and this is consistent with the definition established within Reference 5. Further comparisons to validate the phase measurements can be made by examining the frequency behavior of the round and octagonal shaft experiments. Graphical representations of the frequency ratio comparisons are not made since frequency resolution was substantially reduced when zero crossing algorithms and long time averages were used. The comparisons for the frequency data are listed in Appendices E-I and E-II, however. Normally, the observed $\dot{\phi}_1/\dot{\phi}_{1r}$ ratio was greater than unity for the round shafts and less than unity for the octagonal shafts. This reflects the phase angle behavior for the round shafts (cos $\phi_Y < 0$) and for the octagonal shafts (cos $\phi_Y > 0$), as indicated by Equations (1) and (6). Hence, a qualitative comparison between theoretical and experimental $\dot{\phi}_1/\dot{\phi}_{1r}$ values was consistent.

Figures 12a-c show comparisons between 0.005 inch round shaft data and theory. In Figure 12a, theory and experiment are consistent except for the highest yaw level of Run 4P2A. Appendix D-I shows that at that time, the orbit of the PRIM reduced abruptly, thus, potentially leading to the poor comparison. Figure 12b indicates differences between experiment and theory of roughly 20%, while Figure 12c approaches 50%. Again, in these cases (Runs 6P1 and 6P2), Appendix D-I indicates that the orbit of the PRIM was still growing. Figures 12d-e give comparisons between 0.010 inch round shaft data and theory. Comparisons are consistent for Run 8P2A2, but they are poor for Run 8P1A2. However, the comparisons on Figure 12e differed only by a few percent.

Figures 12f and 12g show comparisons between round shaft theory and 0.005 octagon shaft data. Differences of 30-40% are exhibited for larger angles, but in these cases the round shaft theory gave conservative estimates and perhaps could be used as a design guide.

Only a single 0.015 inch round shaft was reduced for comparison between experiment and theory. In this single case, run 10P32, the motion of the PRIM was not modeled well by the theory until very late in the test. At this point the yaw dramatically grew and, as before, the last yaw level yielded a consistent comparison between theory and experiment (4%).

V. CONCLUSIONS

A series of gyroscope experiments were conducted to study the destabilizing effects of a loose internal part. Non-contact displacement transducers were used to determine the orbital amplitude of the loose part and the phase difference between its motion and that of the gyroscope. Comparisons between the experimentally determined gyroscope yaw growth rates and theoretically predicted yaw growth rates were made. When the assumptions of this steady state theory were closely approximated, the comparisons were consistent. Often, however, the motion of the loose part was not steady and then the assumptions of the theory were restrictive. Phase angle and orbit measurement indicated that maximum and/or nominal values for these quantities should not be used as inputs to the theory. The effective, steady state phase angles were either close to 10° or 170°, while the component of the orbital motion at the gyroscope yaw frequency was typically less than 75% of the maximum available mechanical clearance.

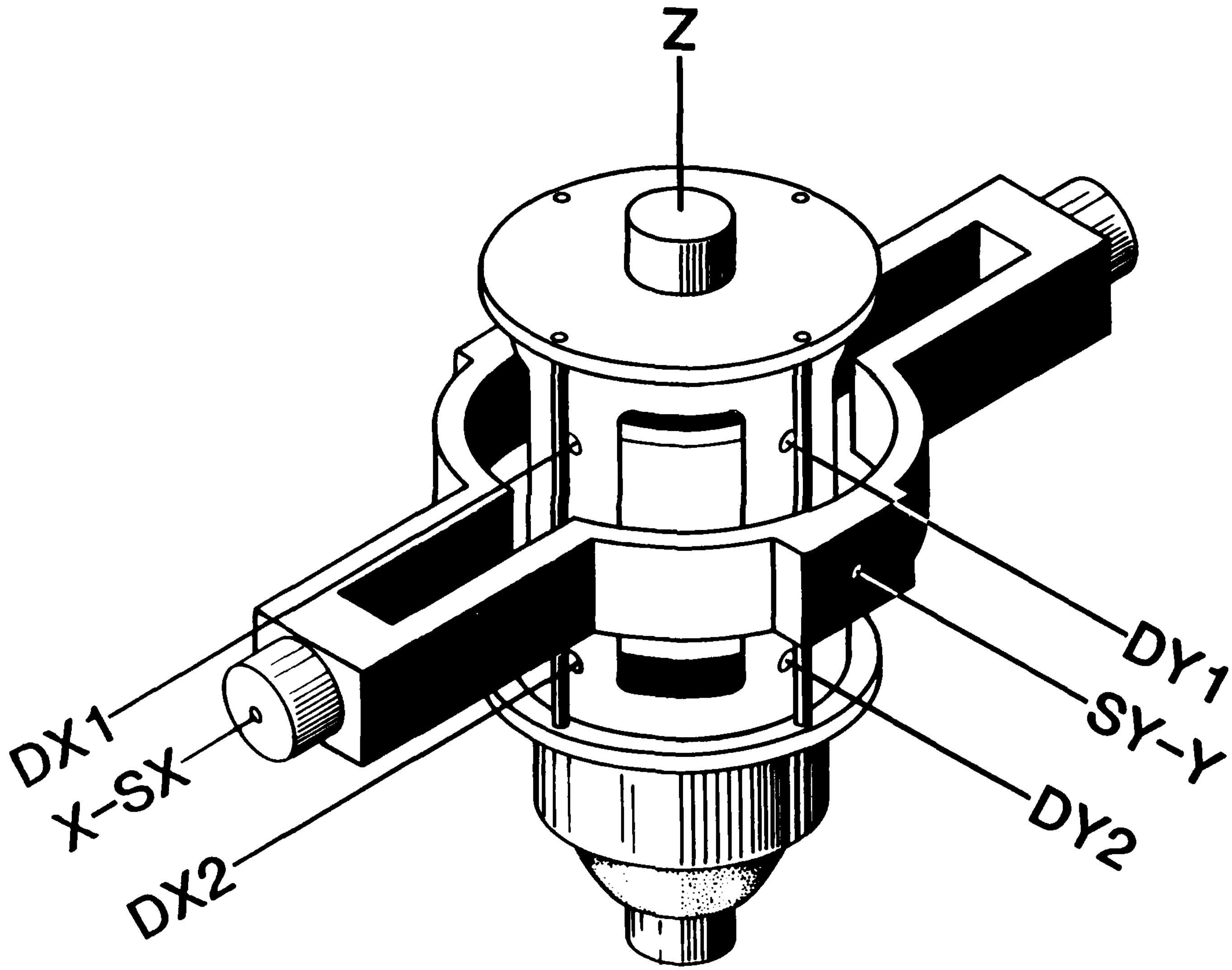

Figure 1. Axis system and transducers for PRIM experiment.

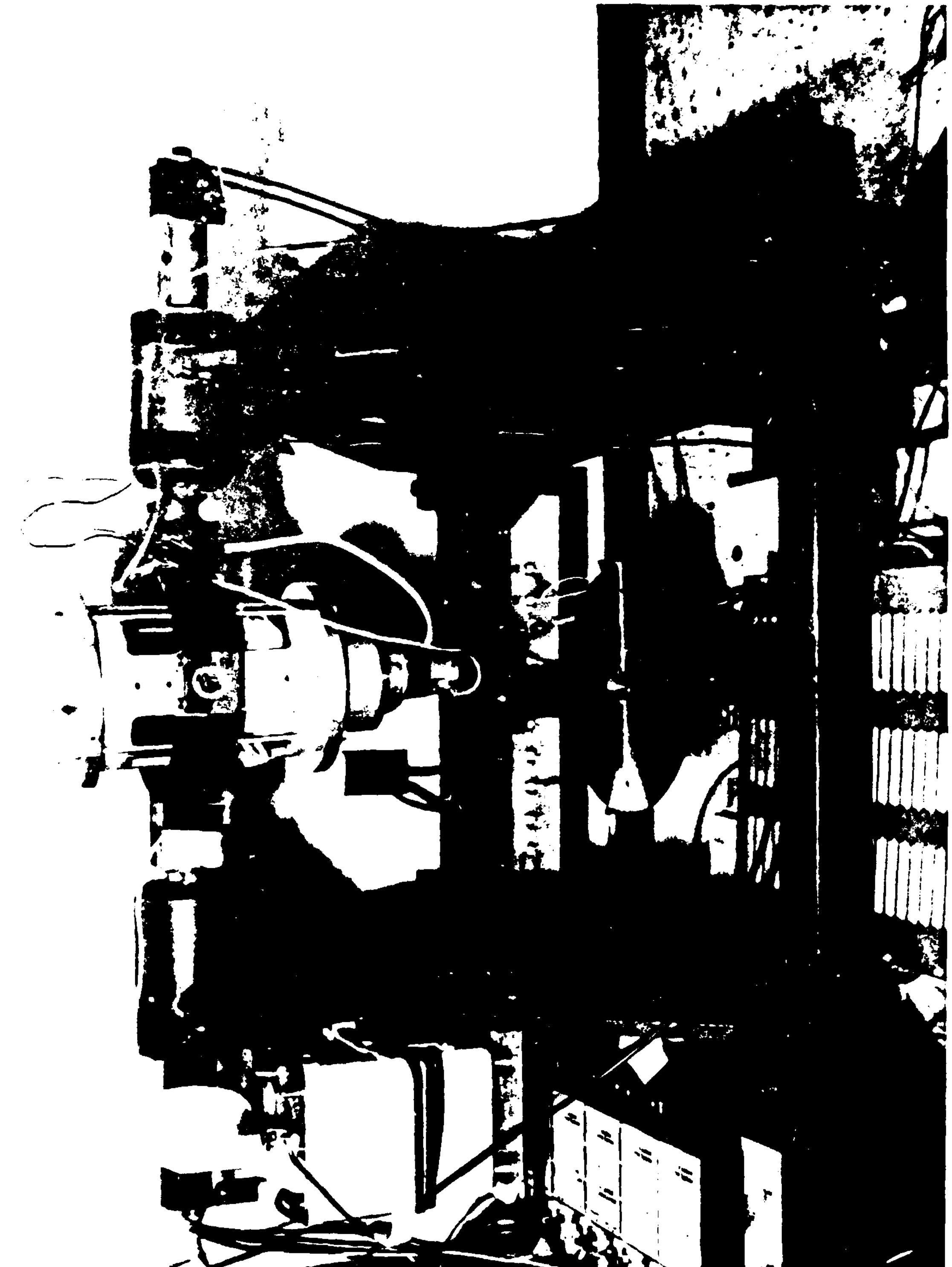

Figure 2. PRIM gyroscope model.

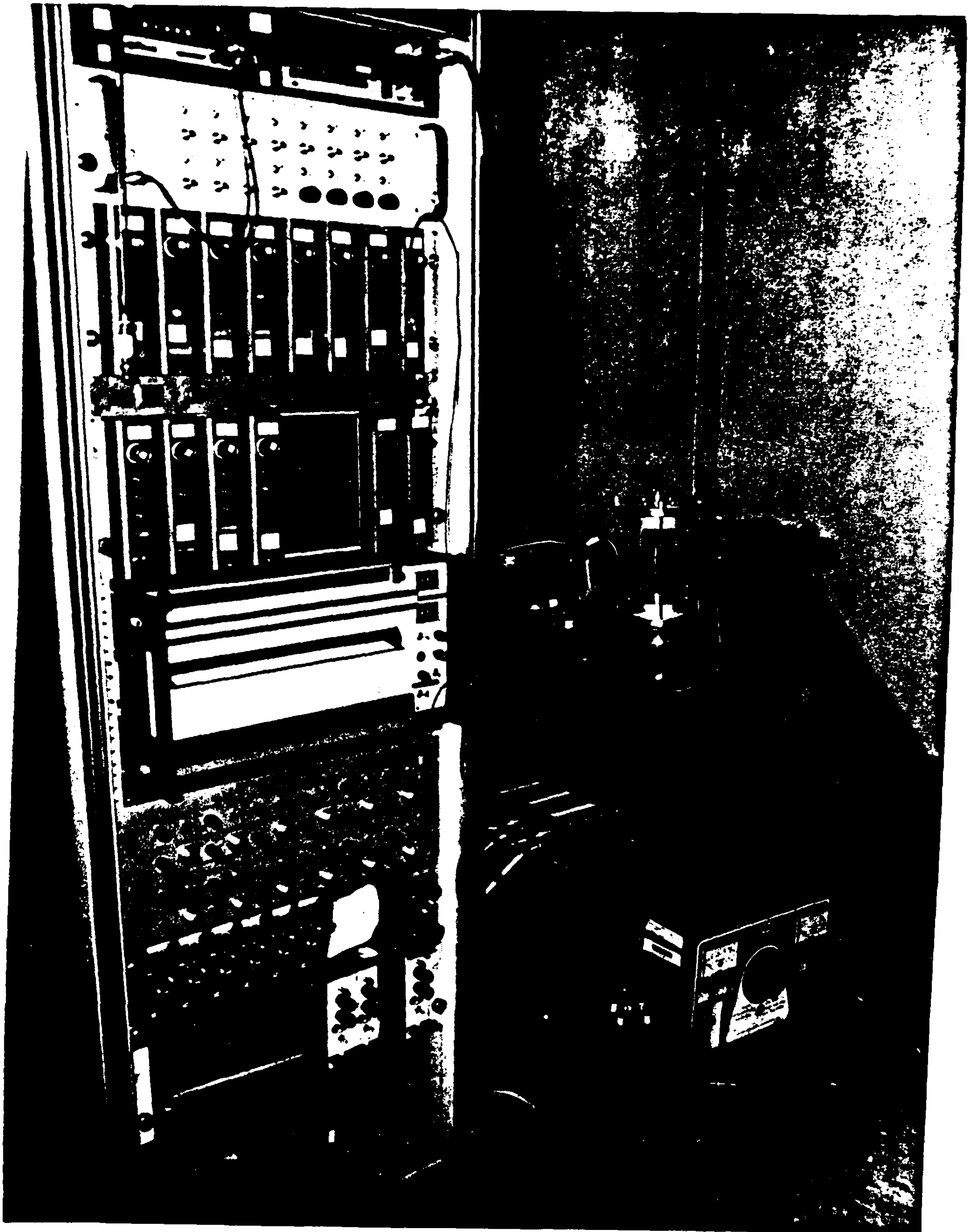

Figure 3. PRIM instrumentation system.

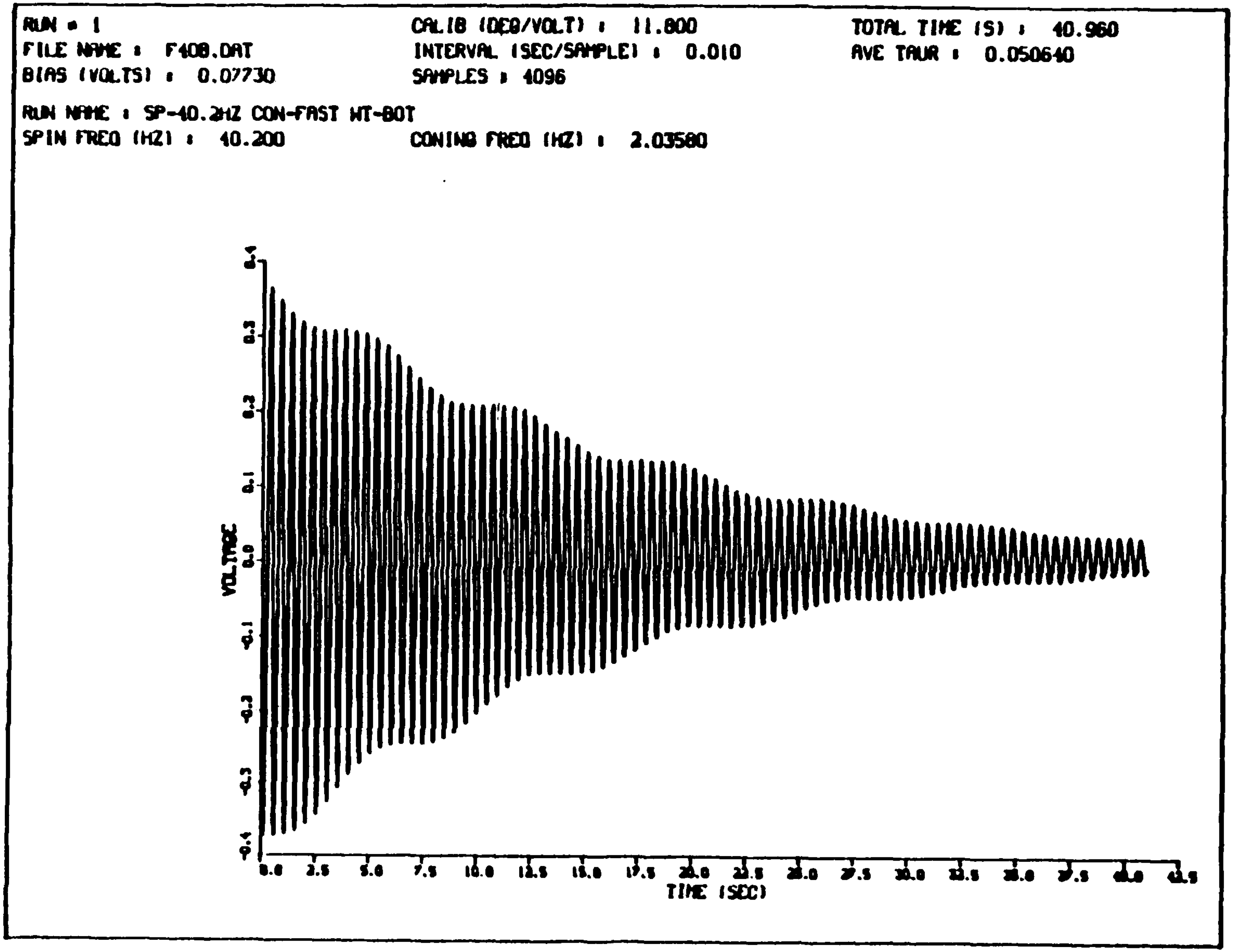

Figure 4. Raw analog SX record.

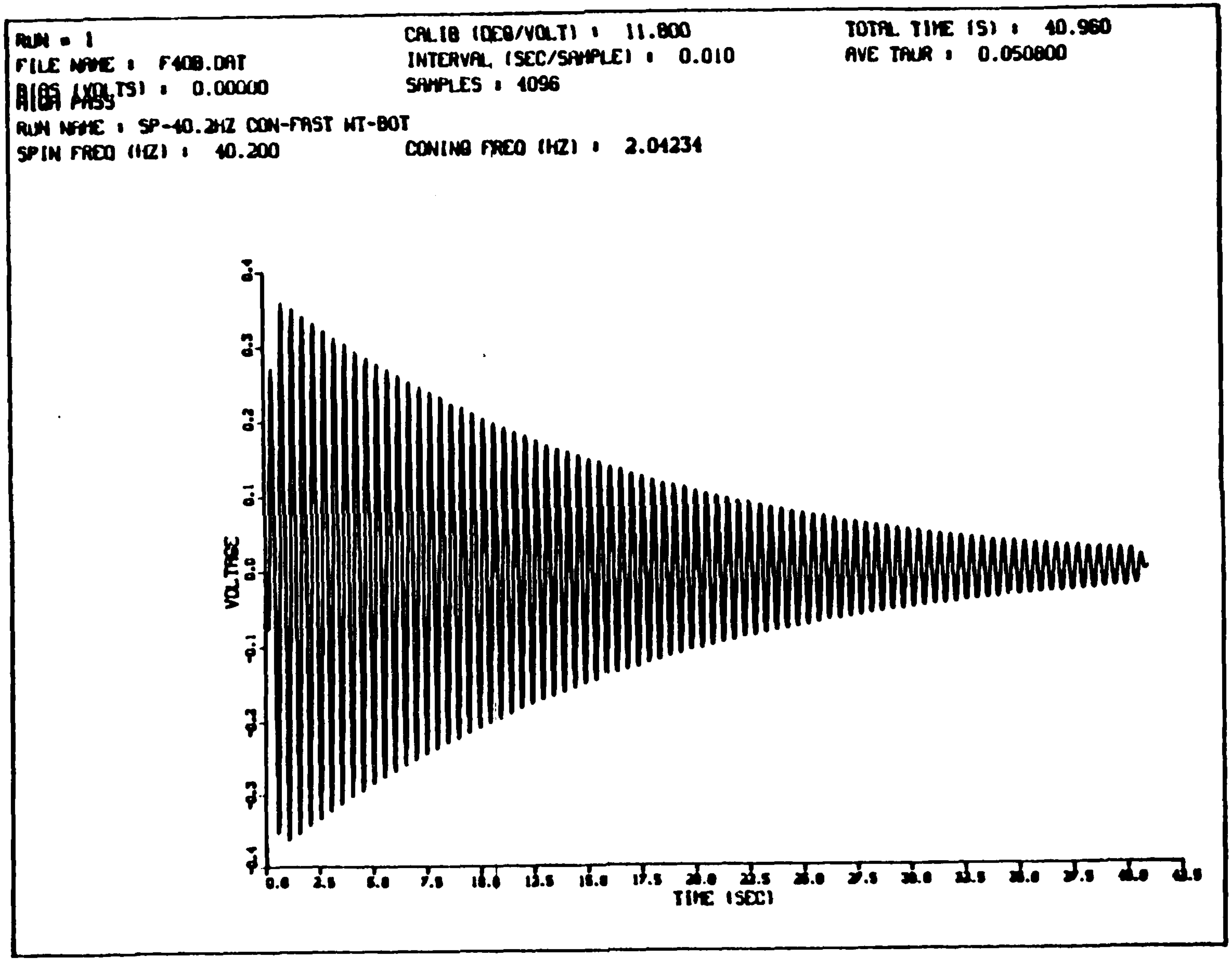

Figure 5. High pass filtered SX record.

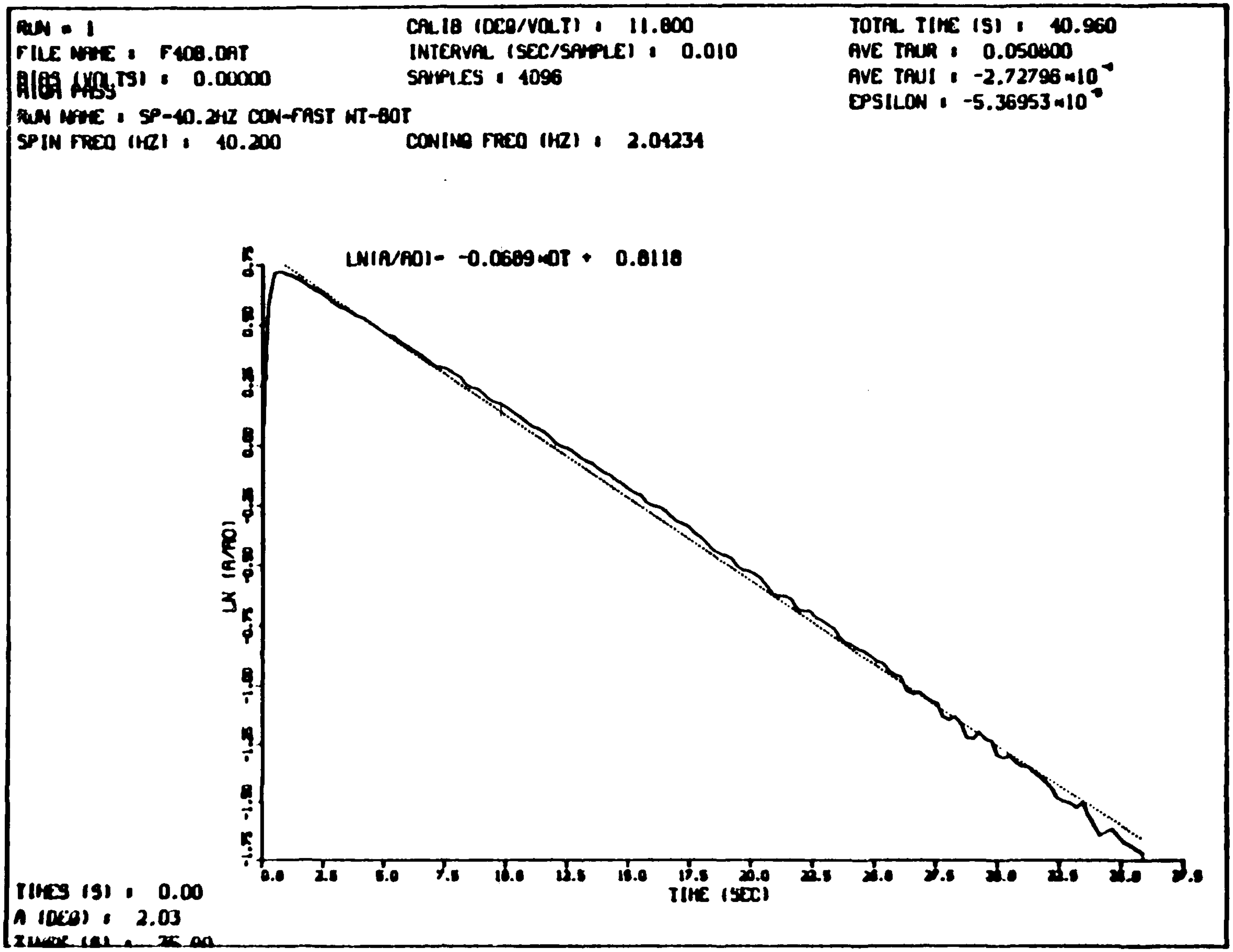

Figure 6. Determination of tare damping.

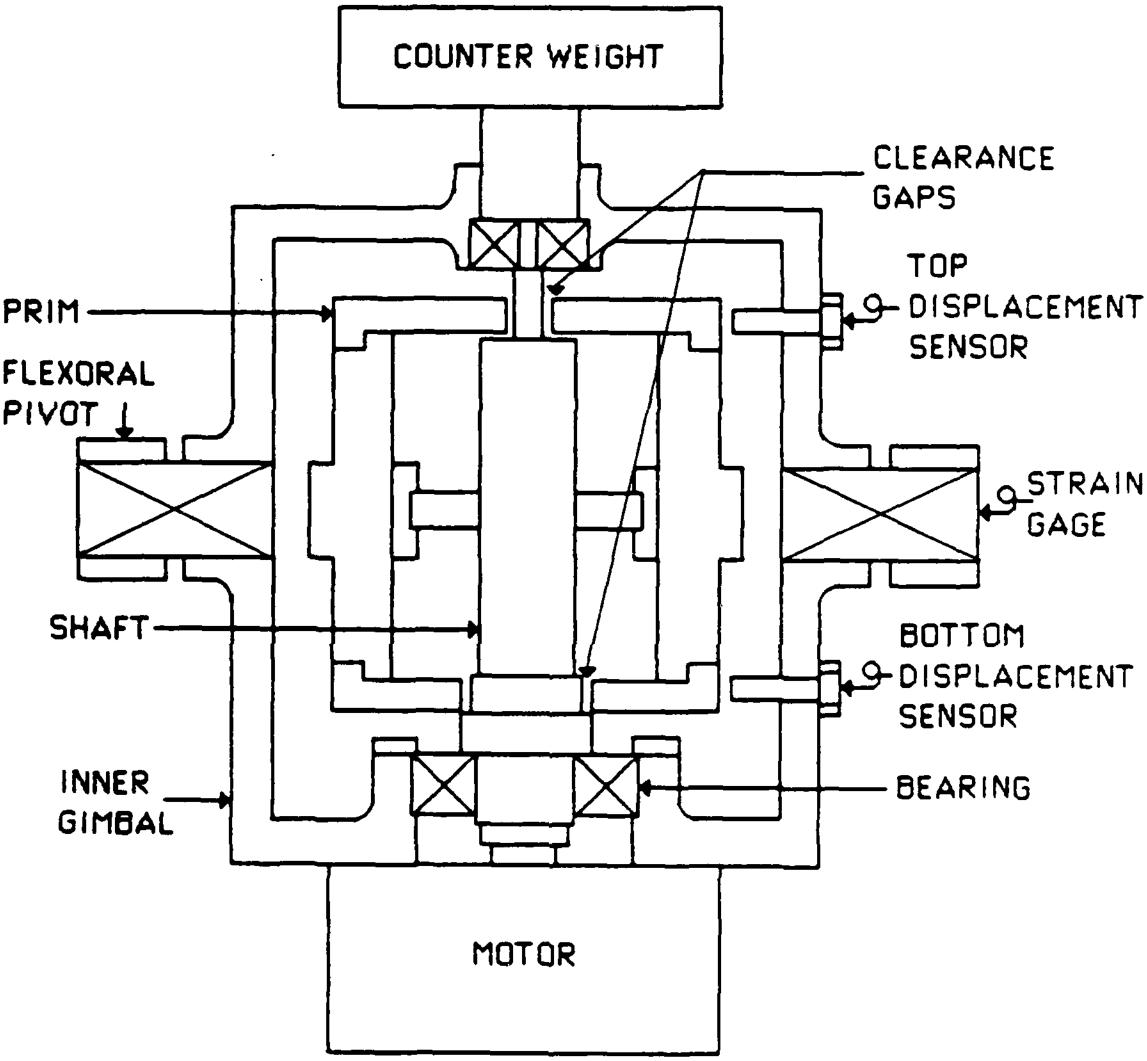

Figure 7. Sectioned view of the gyroscope/PRIM experiment.

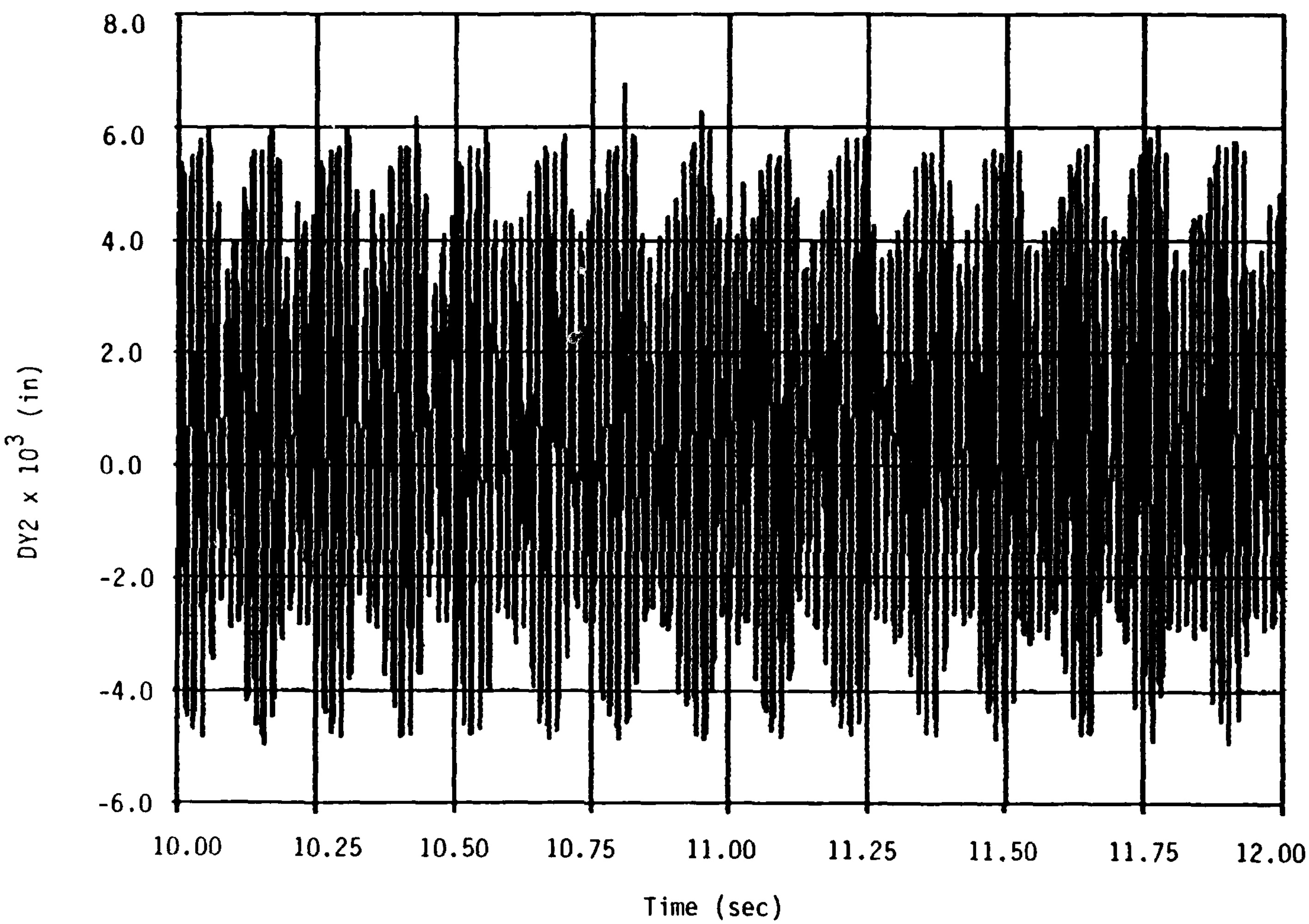

Figure 8a. Digitized DY2 data for Run 4P0.

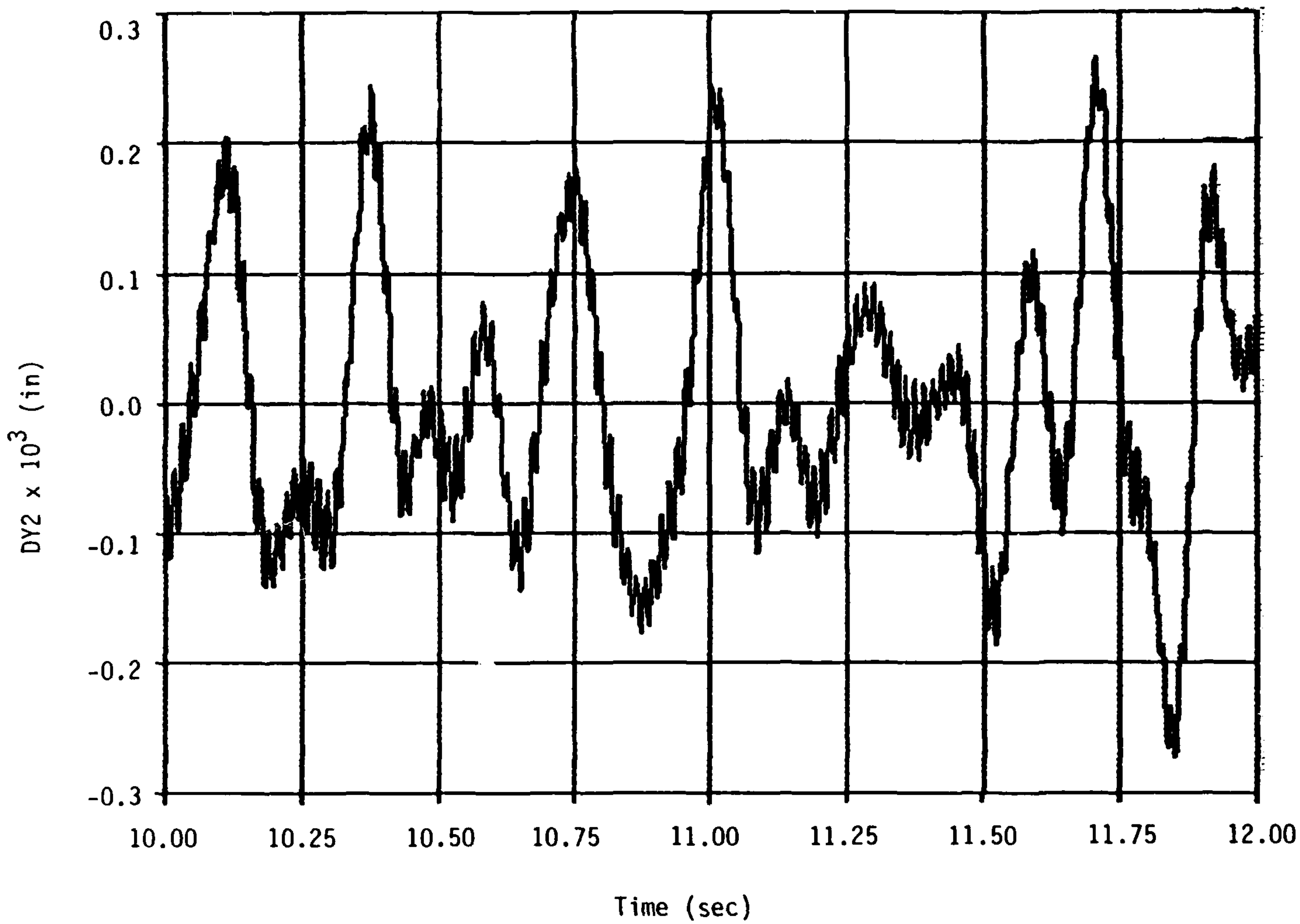

Figure 8b. Low pass filtered DY2 data for Run 4PO (10 Hz cut frequency).

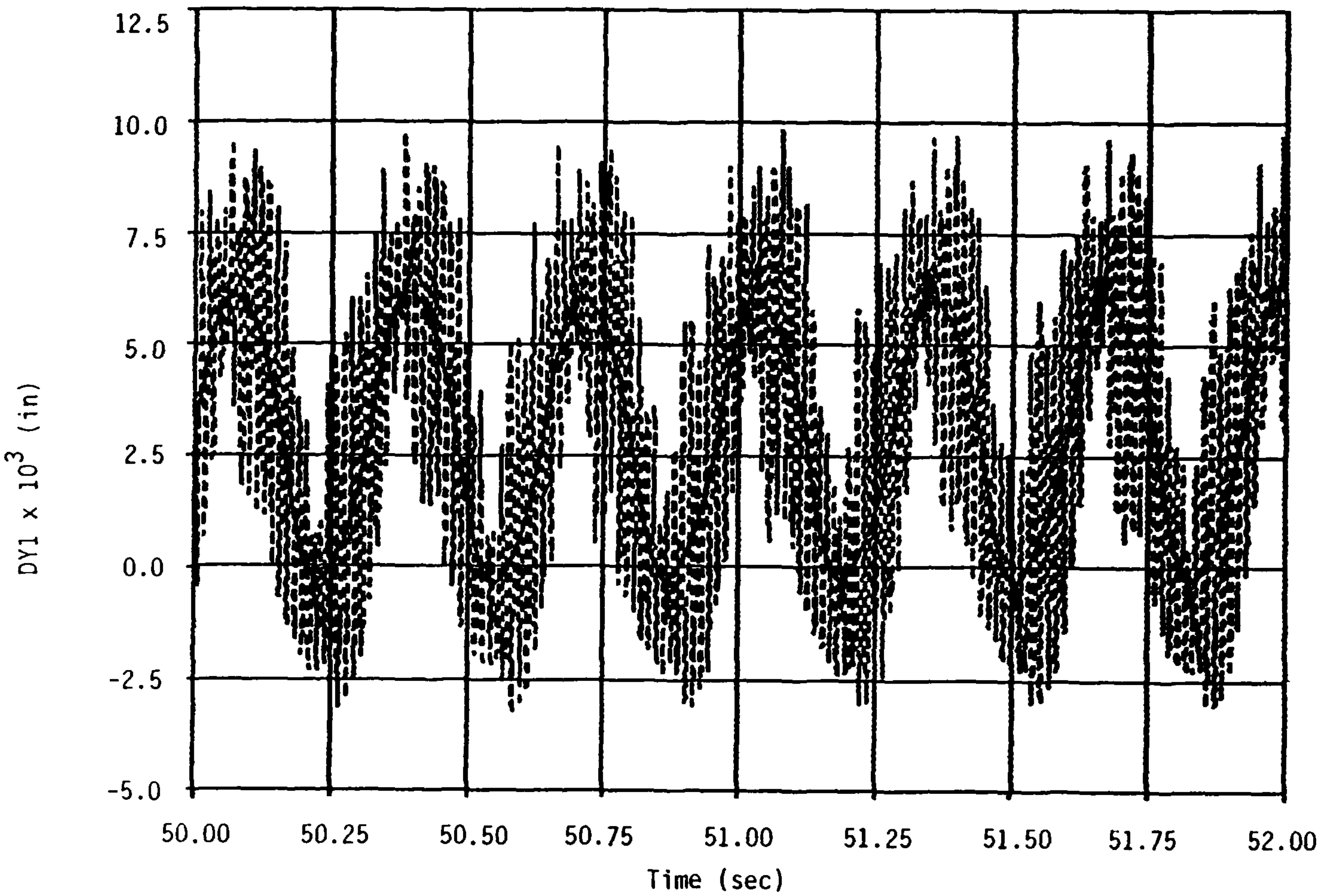

Figure 8c. Digitized DY1 data for Run 4P0 - raw and low pass filtered (10 Hz cut frequency).

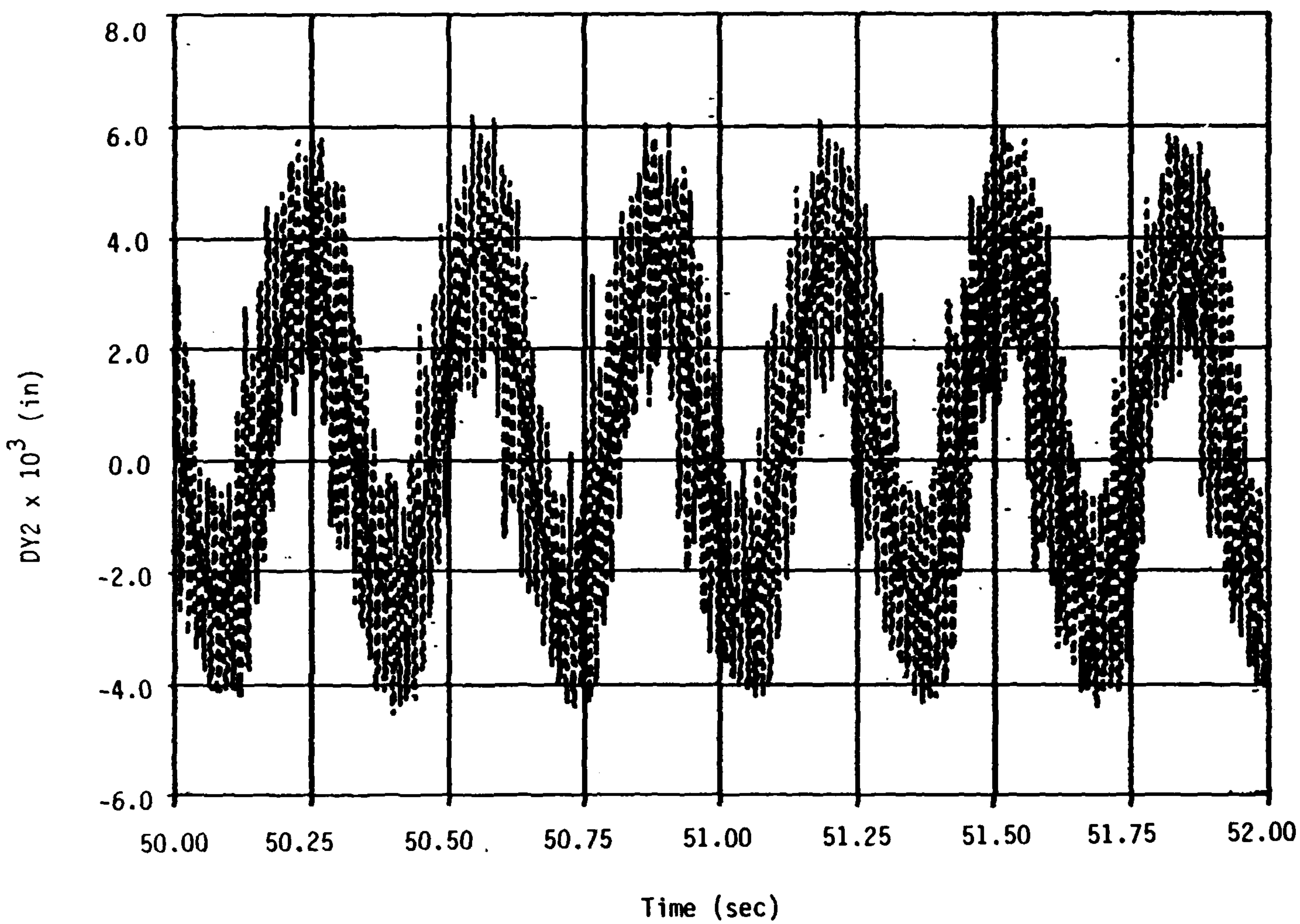

Figure 8d. Digitized DY2 data for Run 4PO - raw and low pass filtered (10 Hz cut frequency).

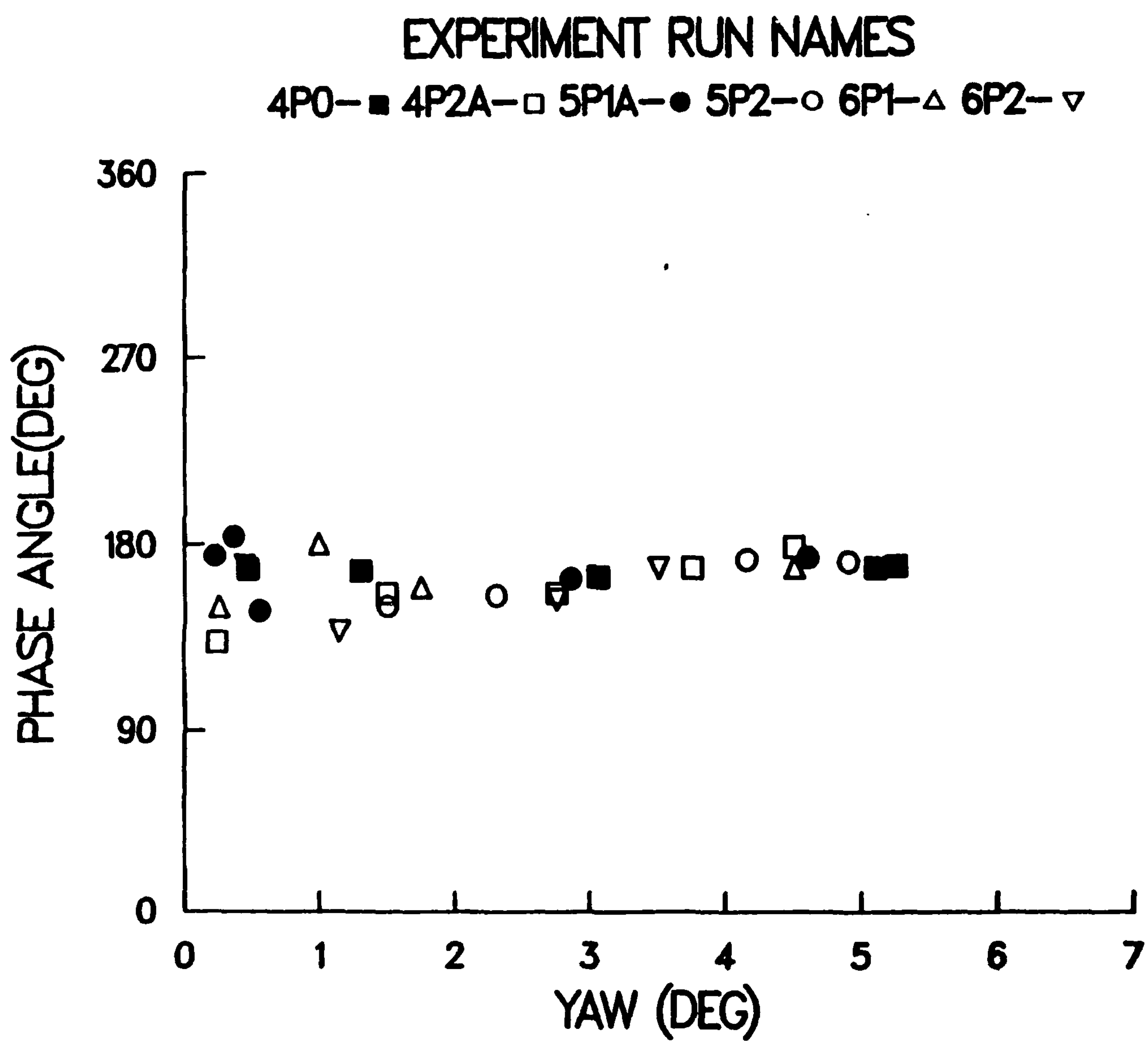

Figure 9a. Phase angle data for 0.005 inch round shafts.

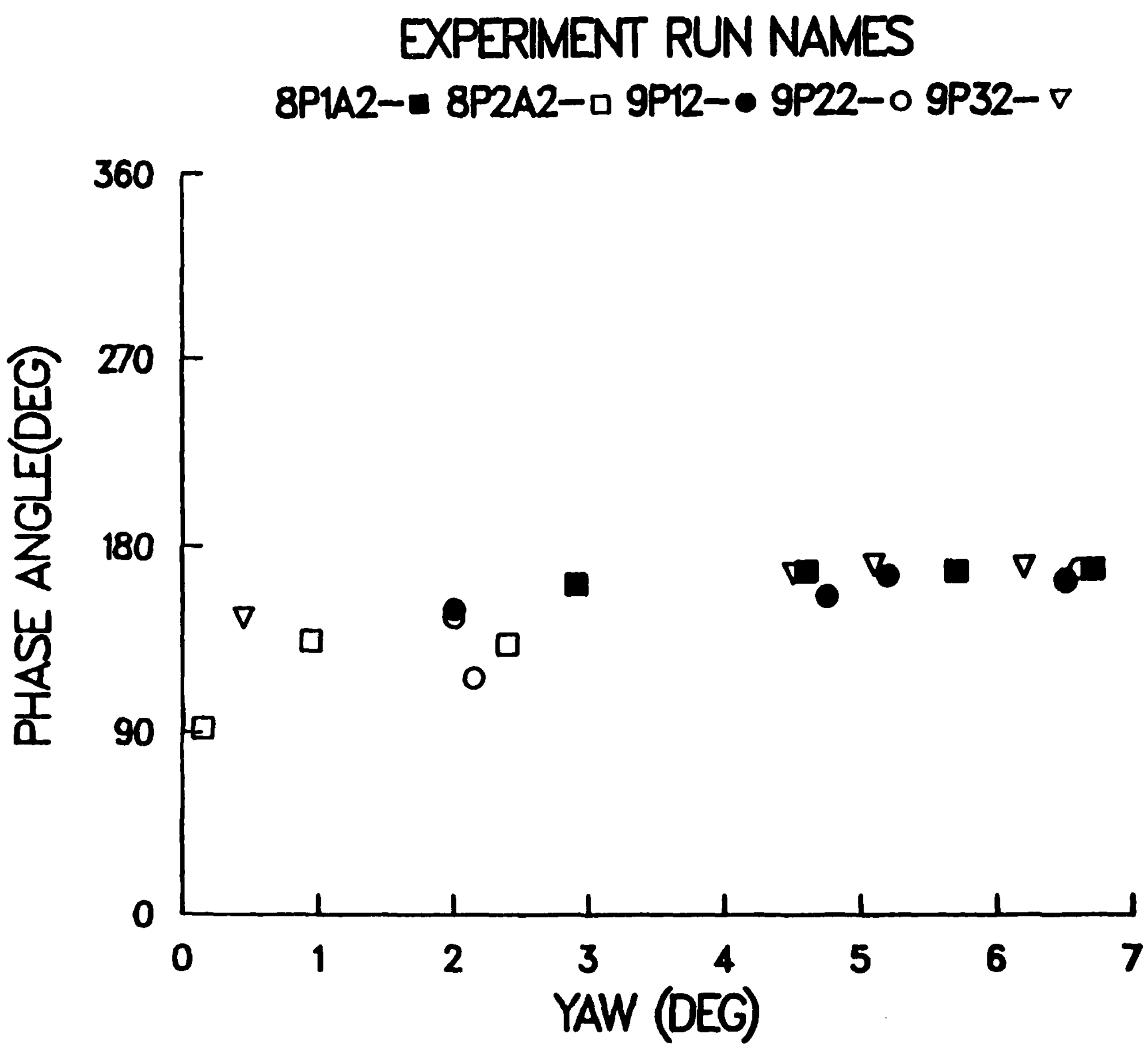

Figure 9b. Phase angle data for 0.010 inch round shafts.

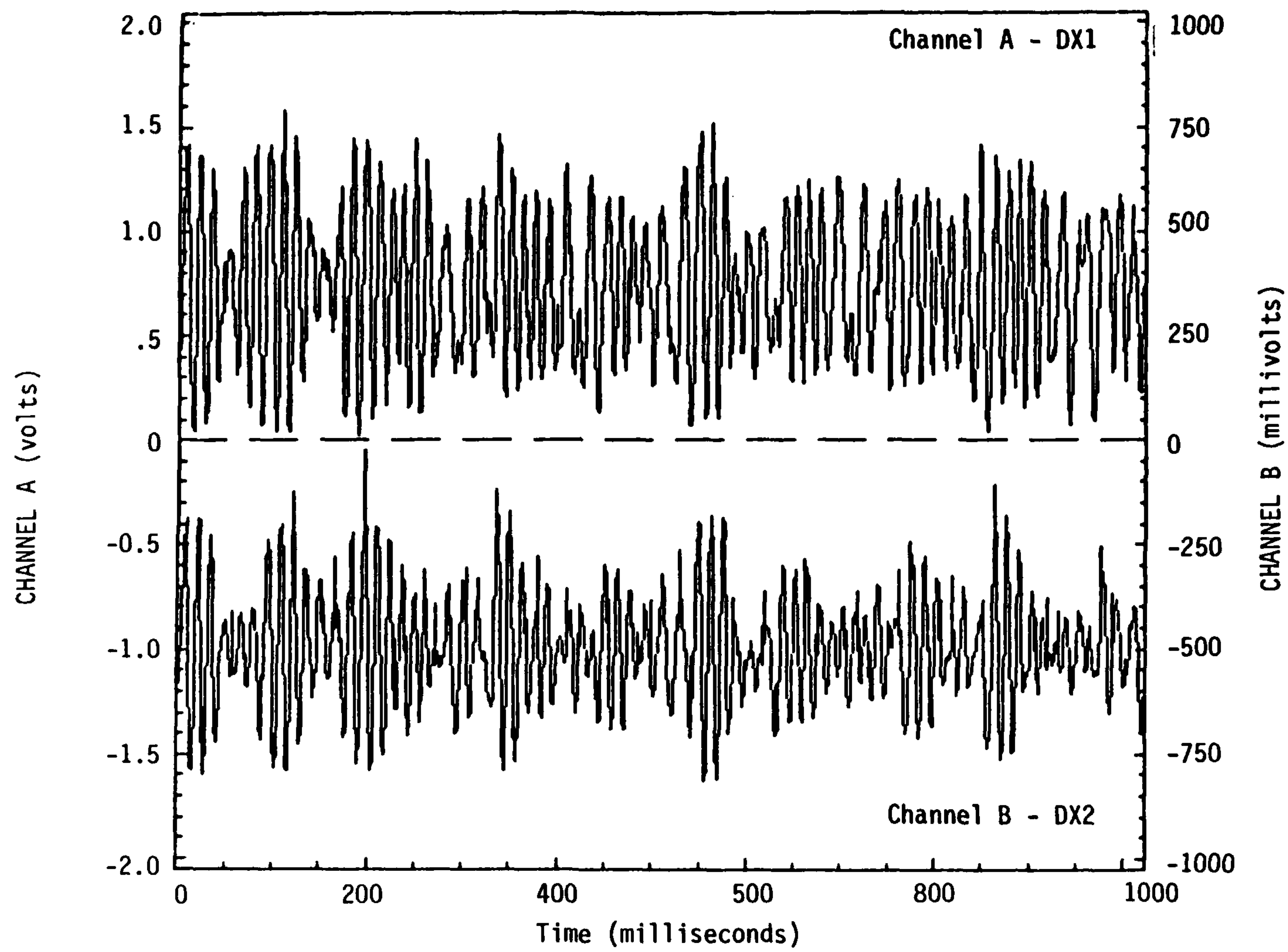

Figure 10a. Comparison of DX1 and DX2 data at early times (Run 13P2A).

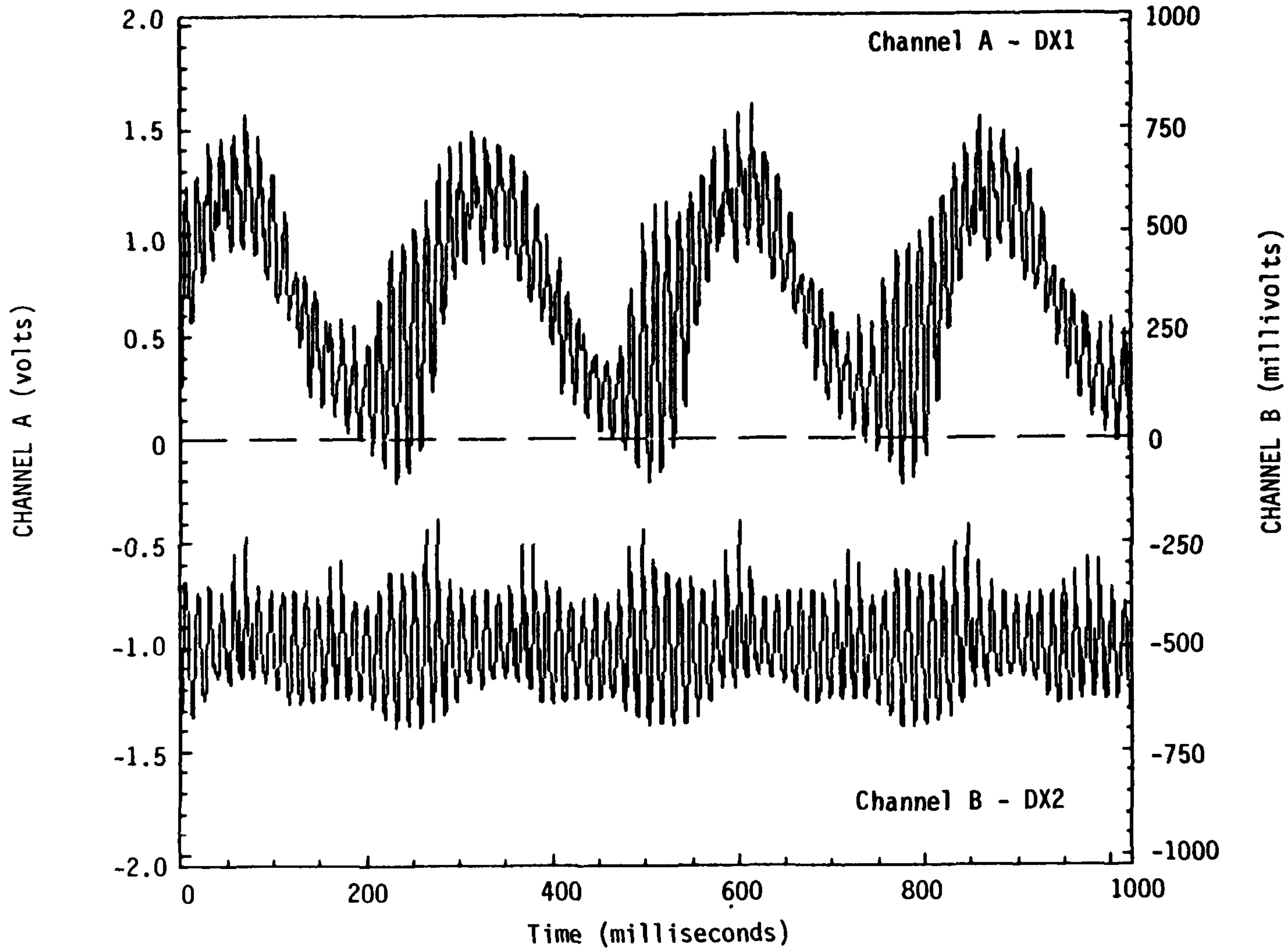

Figure 10b. Comparison of DX1 and DX2 data at late times (Run 13P2A).

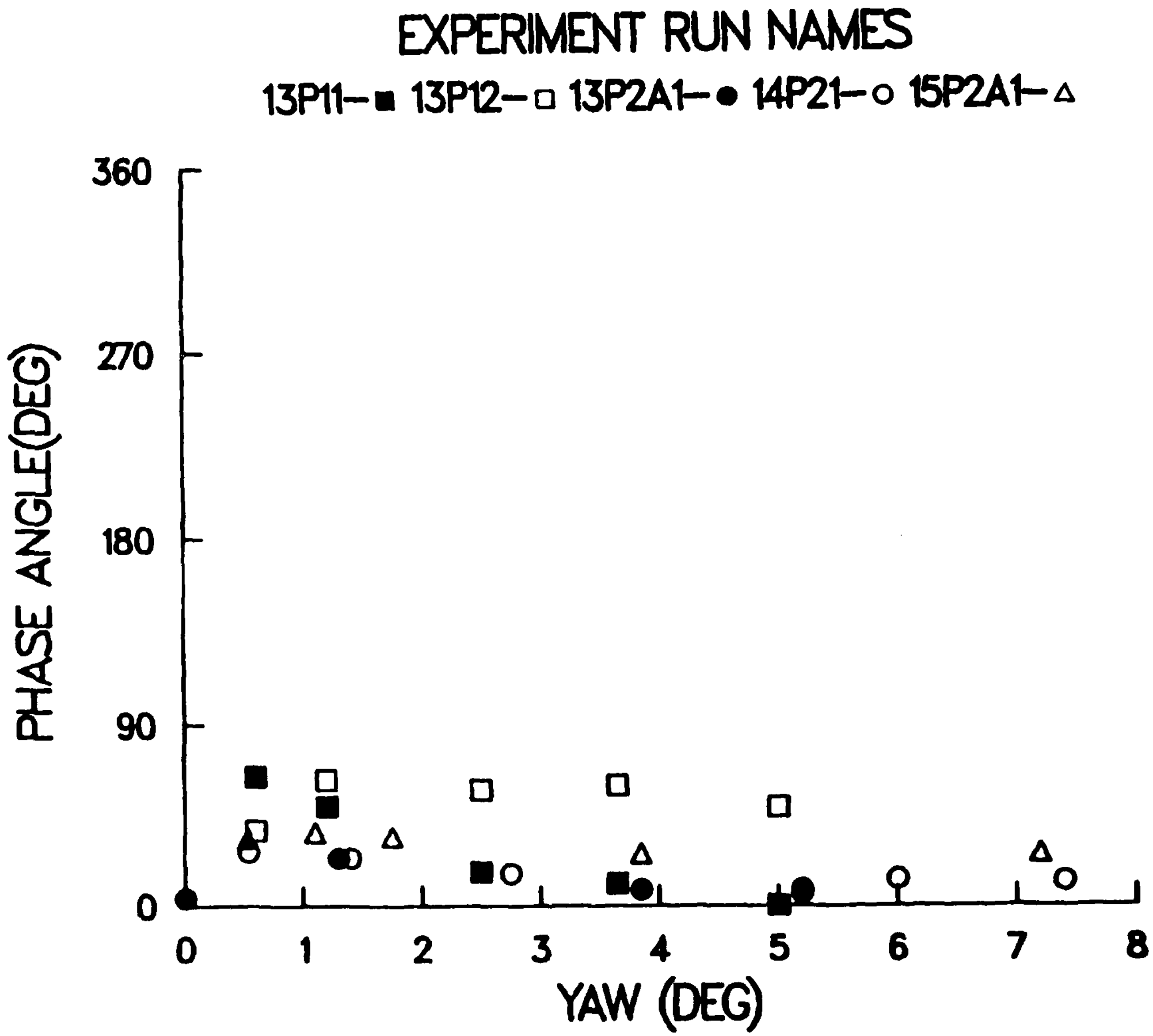

Figure 11. Phase angle data for 0.005 inch octagon shaft.

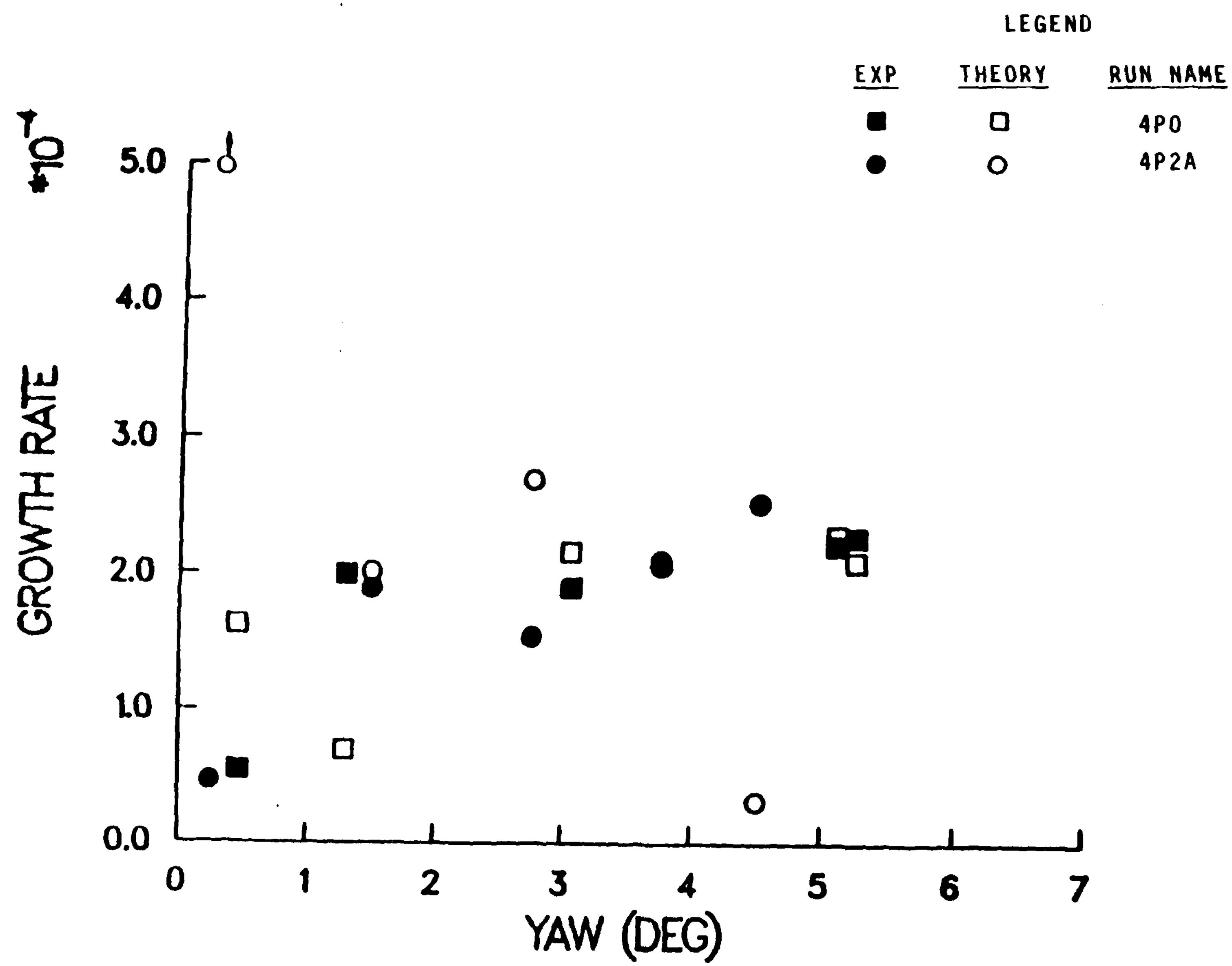

Figure 12a. Comparison of theory and experiment for 0.005 inch round shaft (Runs 4P0 and 4P2A).

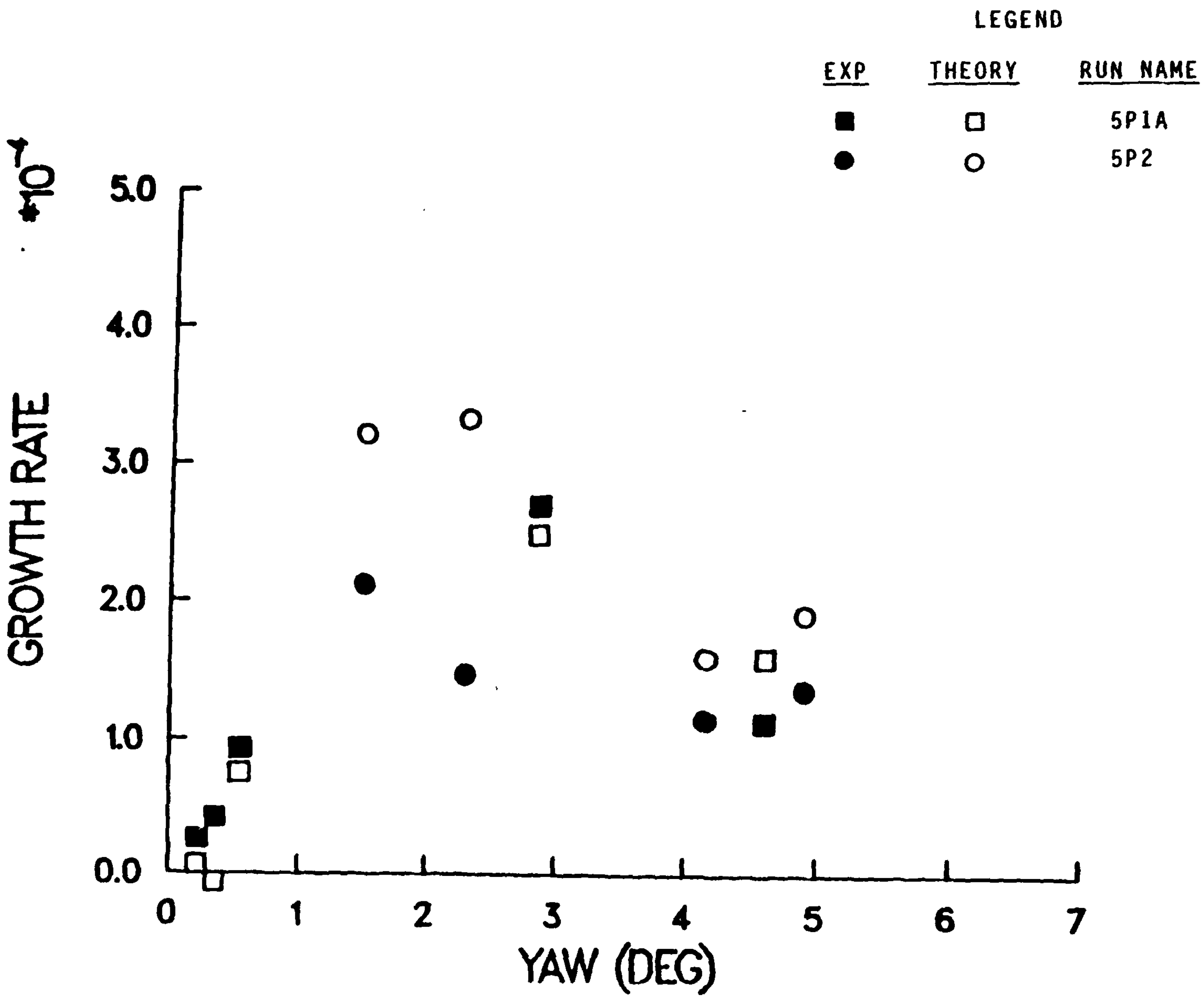

Figure 12b. Comparison of theory and experiment for 0.005 inch round shaft (Runs 5P1A and 5P2).

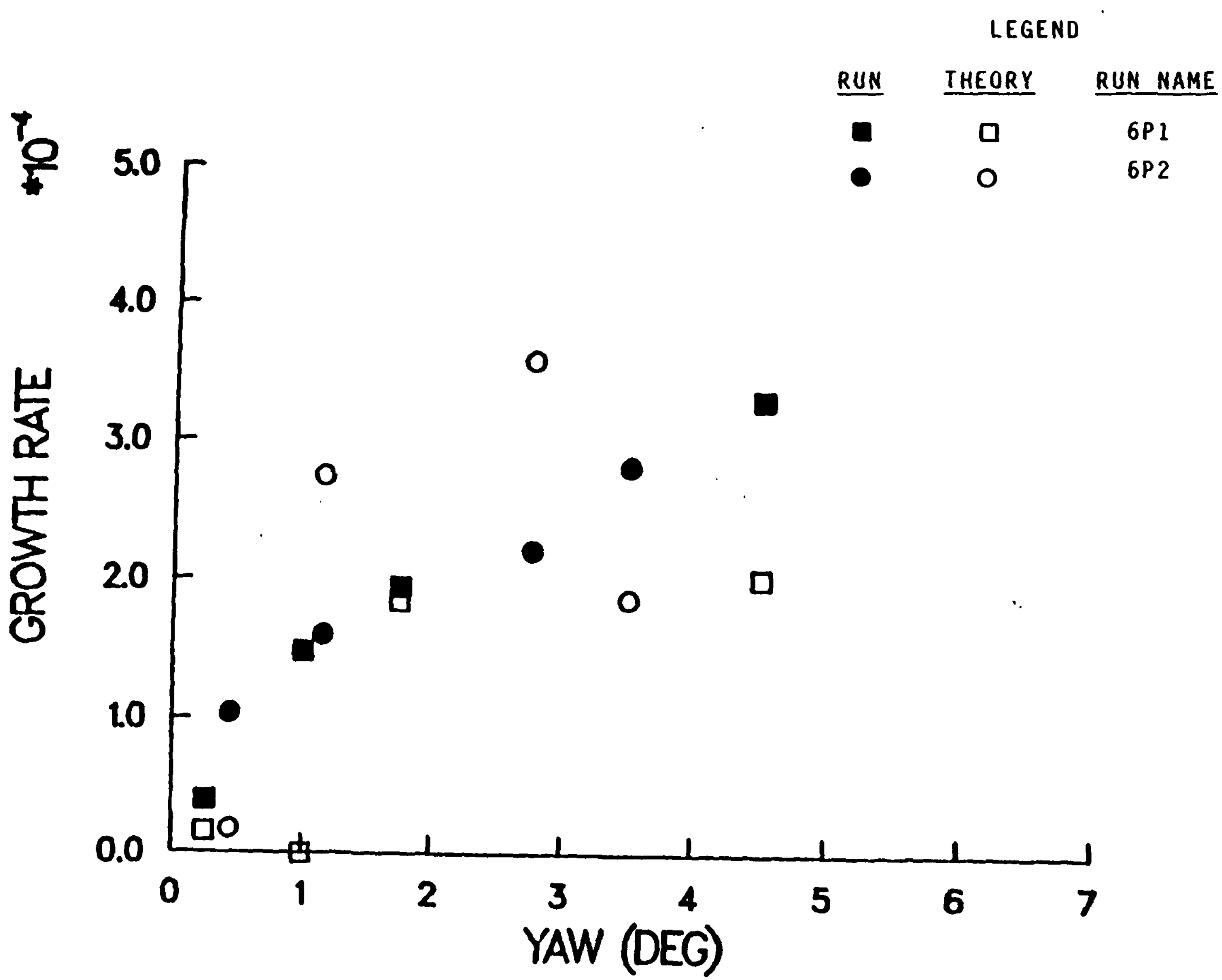

Figure 12c. Comparison of theory and experiment for 0.005 inch round shaft (Runs 6P1 and 6P2).

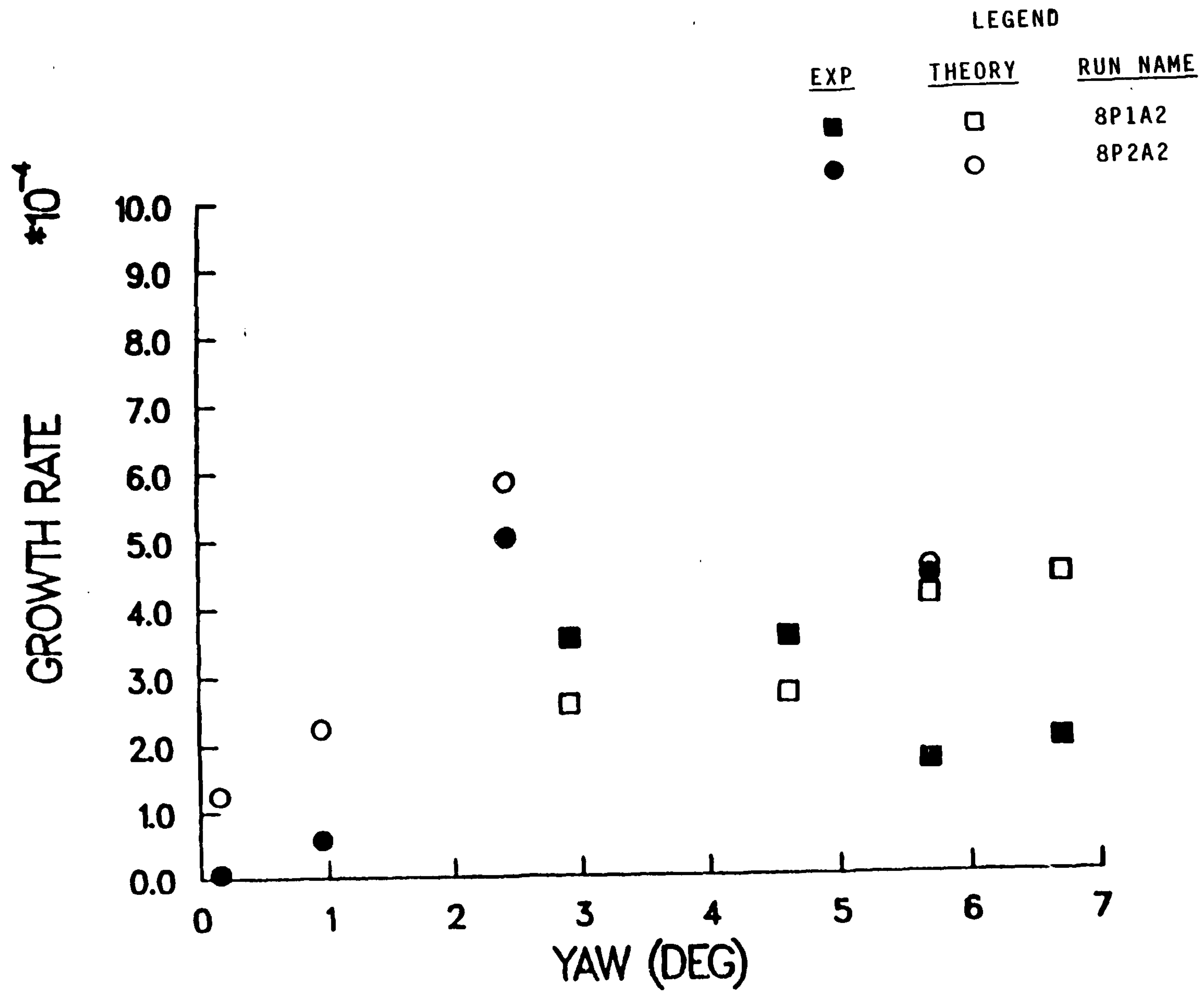

Figure 12d. Comparison of theory and experiment for 0.010 inch round shaft (Runs 8P1A2 and 8P2A2).

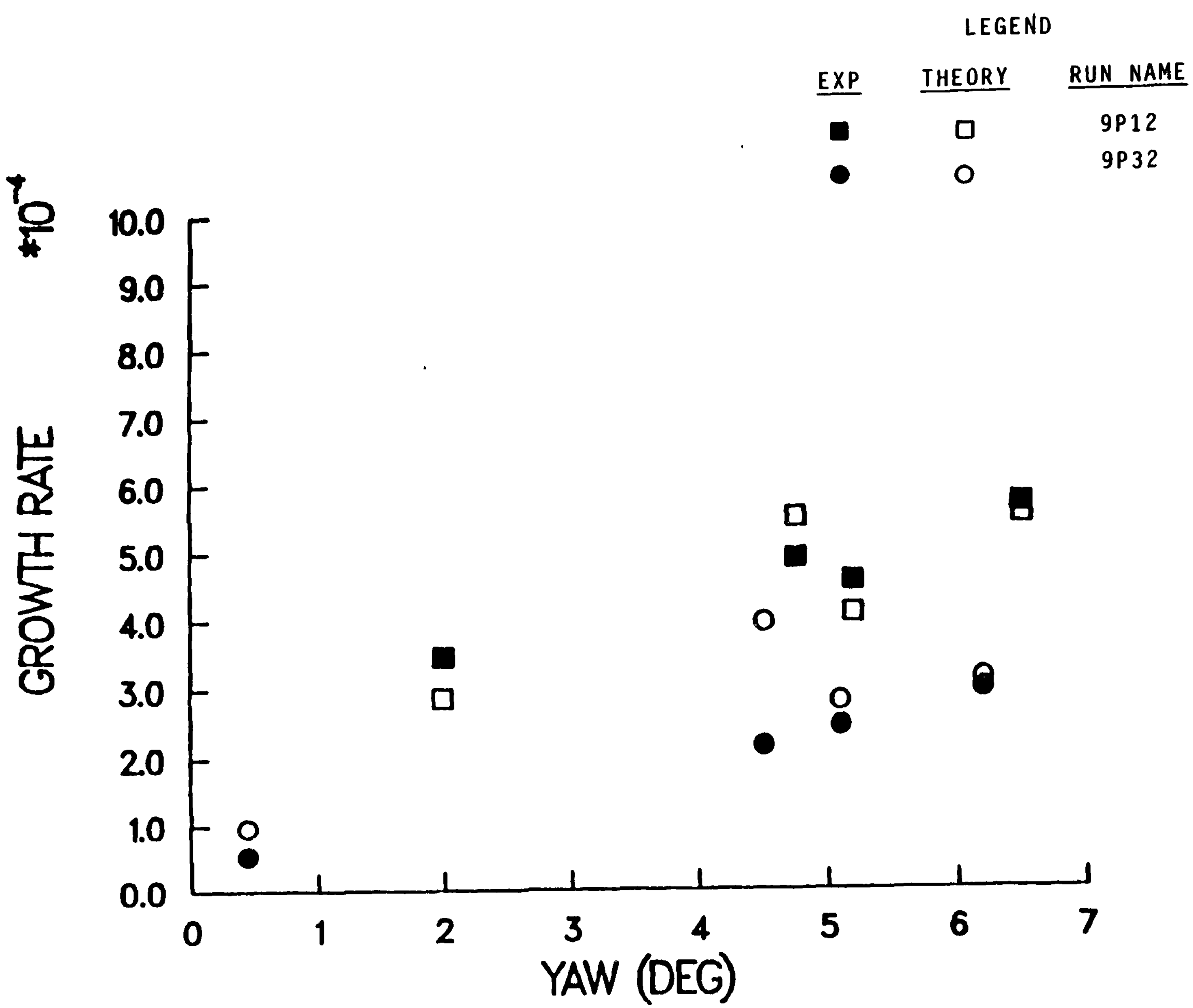

Figure 12e. Comparison of theory and experiment for 0.010 inch round shaft (Runs 9P12 and 9P32).

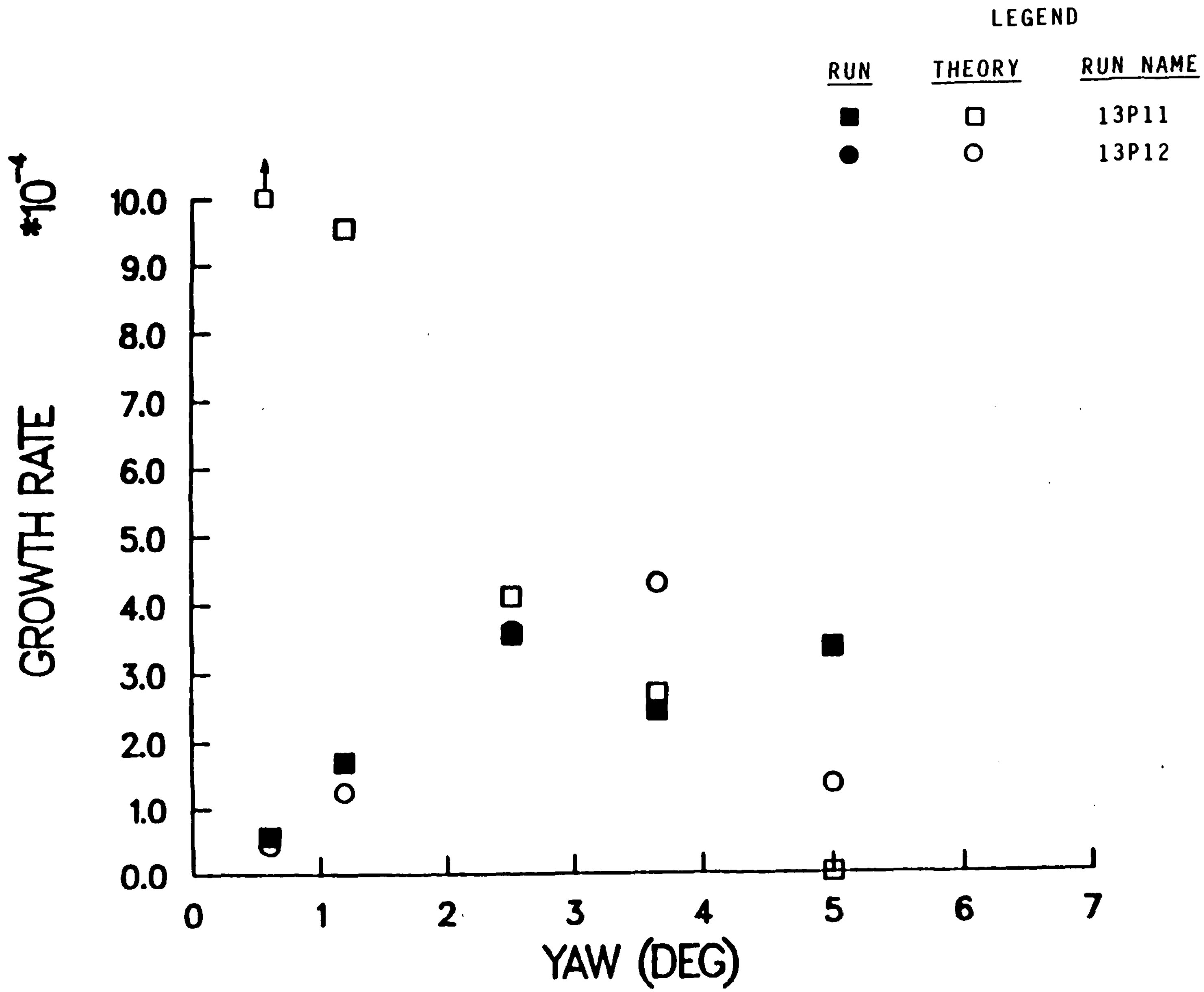

Figure 12f. Comparison of round shaft theory and experiment for 0.005 inch octagon shaft (Runs 13P11 and 13P12).

LIST OF SYMBOLS

K_1	fast precessional amplitude
I_{ab}, I_{ac}	axial (spin) moments of inertia of the gyroscope body and component, respectively
I_{tb}, I_{tc}	pitch moments of inertia of the gyroscope body and component, respectively
I_a	$= I_{ab} + I_{ac}$
I_t	$= I_{tb} + I_{tc} + m_b x_b^2 + m_c x_c^2$
m_b, m_c	masses of the body and component, respectively
x_b, x_c	axial distances between the gyroscope cm and the body cm or the component cm
p, p_c	gyroscope spin, component spin
γ_1	angle for precessional motion of PRIM
ε	radius for cm motion of PRIM
ε_{exp}, ε_{theory}	yaw growth rates for experiment or theory
σ	$(1 - 1/s_g)^{1/2}$, where s_g is the gyroscopic stability factor
$\dot{\phi}_{1r}$	fast precessional frequency for a rigid gyroscope $= \frac{I_a}{2I_t}[1 + \sigma]\,p$
$\dot{\phi}_{2r}$	slow precessional frequency for a rigid gyroscope $= \frac{I_a}{2I_t}[1 - \sigma]\,p$

LIST OF SYMBOLS (continued)

ϕ_ε	phase angle for cm motion of PRIM
ϕ_γ	phase angle for precessional motion of PRIM
λ, λ_t	yaw damping, tare damping

APPENDIX A

DETERMINATION OF PHASE ANGLES

APPENDIX A. DETERMINATION OF PHASE ANGLES

A primary objective of this PRIM experiment was to determine the phase angle between the yawing motion of the gyroscope and the motion of the PRIM. This phase angle was defined in Reference 5 in terms of the two types of motion assumed in the model (phase angles for a precession of the PRIM (ϕ_Y) or for a cm motion of the PRIM (ϕ_ε)). Using these definitions, the natural phase relationships of all of the data transducers must be established for the simple case of in-phase motion of the PRIM and the gyroscope. Figures A1a and A1b show data from SX and SY and indicate that SX leads SY by 90 degrees. This convention is used to determine the phase difference between the yaw and PRIM motions. For $\phi_Y = 0$, Figures A2a and A2b show the position of the PRIM and the inner gimbal with respect to the sensors located in the X-plane. Figure A2a depicts the position of the inner gimbal and the PRIM when the plane of the PRIM motion is aligned with the X-plane. For Figures A2a and A2b the output of SX is zero. In Figure A2a the output of DX1 is a minimum, while DX2 is a maximum. In Figure A2b the output of DX1 becomes a maximum, while DX2 is now a minimum. Therefore, for precession of the PRIM at the coning frequency of the gyroscope, DX1 and DX2 are out of phase by 180 degrees. (If the PRIM were in a cm motion, either at the spin rate or the coning frequency of the gyroscope, then DX1 and DX2 would be in phase.) Similar relations can be established for the Y-plane transducers. A complete phase diagram for all transducers is shown in Figure A3 when $\phi_Y = 0$. Some of the transducers are in-phase (SX to DY2 and SY to DX1), but typically the raw data must be corrected for any natural phase orientations in order to properly determine ϕ_Y.

1. TRANSFER FUNCTION METHODOLOGY TO DETERMINE PHASE

The phase angle between the plane of the PRIM motion and the yaw plane must be determined in a convenient and reliable fashion. Data from three displacement transducers can be used to completely define the motion of the PRIM. However, this requires that the data be pre-processed or filtered to remove components of the motion not at the yaw frequency of the gyroscope. If the motion of the PRIM is well behaved, i.e., the motion is similar at all four displacement transducers, then the data from only one displacement transducer and a flexural pivot could be used to determine ϕ_Y. This can be accomplished by using a transfer function phase measurement between SX and DX1, for example. This phase measurement when corrected by the relationships in Figure A3 would then yield ϕ_Y. The transfer function could be obtained by analog or digital methods. It was convenient to use a Hewlett-Packard 3582A spectrum analyzer (SA) for phase measurements. The SA provides the phase across the entire bandwidth, which was typically selected as 100-0 Hz (since the spin was less 100 Hz). This type of measurement requires a sampling time of 5.0 seconds to determine the phase and perform anti-aliasing functions. The accuracy of the phase angles obtained with the SA is ±5 degrees. It is possible to increase the length of the time record to compute an "averaged phase" for that given sampling period. It is highly probable that the gyroscope/PRIM parts produce a yaw growth rate that is based upon an average rather than instantaneous phase angle. Hence, this scheme for the determination of phase is quite realistic. At times, the frequency versus phase plots were quite random in appearance. Under these cases, an "instantaneous phase" measurement was made by digitizing and plotting both the yaw and displacement data and measuring the time delay between the wave forms to obtain the phase. Comparisons of the phase using these two measurement techniques were consistent.

The SA can also be operated in an RMS averaging mode. In this mode, a cross-power spectrum is computed to statistically increase the confidence level of the transfer function measurement.[A-1] This averaging process does not impact the measurement accuracy of the SA, however. A short explanation of the properties of the coherence function follows. The coherence function is a dimensionless, frequency-domain function whose range is from 0 to +1. For a particular frequency, the value of the coherence function represents the fraction of the output power to the input power (for our case a flexural pivot was the input, while a displacement transducer was the output).

The coherence function behaves as a cross-correlation function in the frequency domain. Hence, for a selected number of averages and for a coherence function of unity (or nearly unity), the phase measurement at that frequency is highly reliable. For a typical data trial when the yaw was less than one degree, the motion of the PRIM and the gyroscope yaw were not highly coherent, i.e., the coherence function was not unity at any frequency. At later times in a data run, the coherence function was unity only at the gyroscope coning frequency. Such a measurement indicates that the PRIM and the gyroscope had similar motions for that time frame but were simply out of phase.

A sequence of plots will now be shown for the raw analog signals (SX and DX1). Fourier spectra of these signals, phase transfer functions, and coherence functions are also included. Figure A4a shows raw (unfiltered) analog data for SX and DX1 for a round shaft experiment. Frequency spectra for DX1 and SX are shown in Figures A4b and A4c, respectively. Note that the Fourier amplitudes (the voltages) of the signals at 3.2 Hz (approximately equal to the coning frequency) are approximately the same for SX and DX1. Due to the large dynamic range of the SA, even these low amplitude signals can be properly analyzed for phase, as shown in Figure A4d. Since the phase measurement across the entire bandwidth (100 - 0 Hz) appears to be random, the coherence function can be used to provide confidence in the measurement process. The coherence function, shown in Figure A4e, has a value of 0.98 (labeled as 0.98 cf) for a frequency of 3.2 Hz. Similar plots are shown in Figures A5a-e for the same data trial but at larger amplitudes of yaw and longer times (approximately 20 seconds later). Raw analog data are shown in Figure A5a, while the associated spectra are shown in Figures A5b and A5c. The phase measurement and coherence function are shown in Figures A5d and A5e, where it is noted that the phase angle and coherence function at 3.2 Hz have changed only slightly. However, from the analog data shown in Figures A4a and A5a, one would expect the coherence function to be radically different; but it is not. This is an indication of the utility of the transfer function method and the resolution of the SA. Similar data sets are provided for an octagonal shaft at small and large amplitudes (Figures A6a-e and Figures A7a-e, respectively). The character of the PRIM motion at small (Figure A6a) or large (Figure A7a) amplitudes of yaw is quite different. This is reflected by the coherence functions at 4.0 Hz (0.86 cf in Figure A4e versus 1.00 cf in Figure A5e).

2. DIGITIZATION AND DIGITAL FILTERING

The raw analog data were digitized at a sampling rate of 1.66 kHz using a VAX 11/780 system (analog filtering was not used since phase delays would be introduced). This sampling rate is sufficiently fast to properly resolve the highest frequency component of the data, which is the spin rate (maximum spin rate = 100 Hz). This sampling rate is not sufficiently high to accurately reproduce the signals produced by the flats that were machined on the end caps of the PRIM. These flats will produce sharp spikes in the output of the displacement transducers and have a frequency content of at least 2 KHz. In many instances, these spikes would need to be removed (by filtering) so as not to contaminate the displacement data. Since the spikes produced by the flats were not required for data reduction or interpretation, a slower sampling rate was used.

Raw SX and SY data often exhibited an unacceptable amount of noise. The source of this noise was attributed to the mechanical vibrations induced by the PRIM. A zero-delay (no phase delay) digital filter was used to process the digitized data files. The SX and SY data required repeated filtering since simple peak-to-peak and zero-crossing techniques were used to determine coning frequency and yaw growth rate. Also, digital filtering was used to separate the total PRIM motion into frequency components. This was very useful in understanding the many types of possible motion.

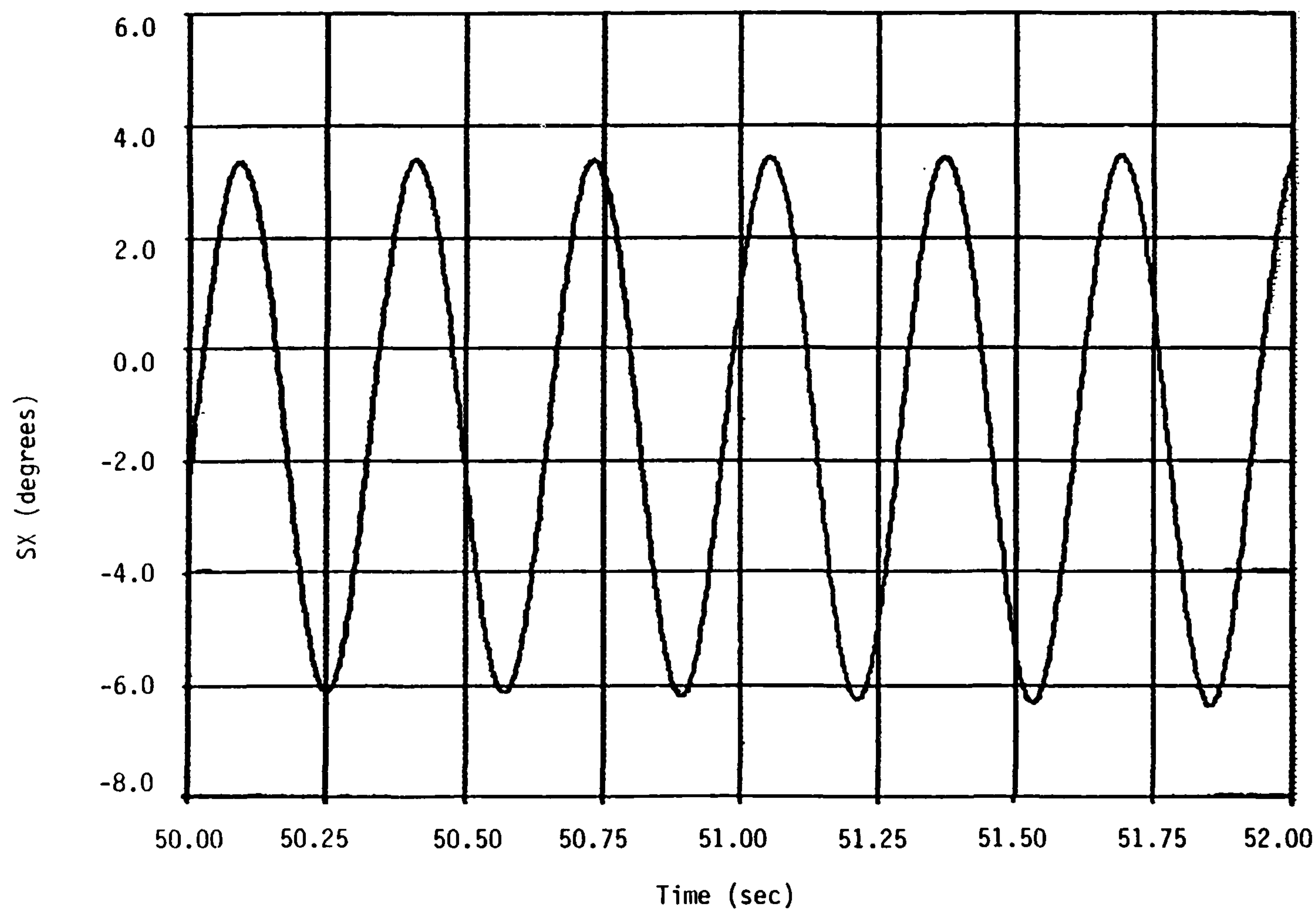

Figure A1a. SX versus time.

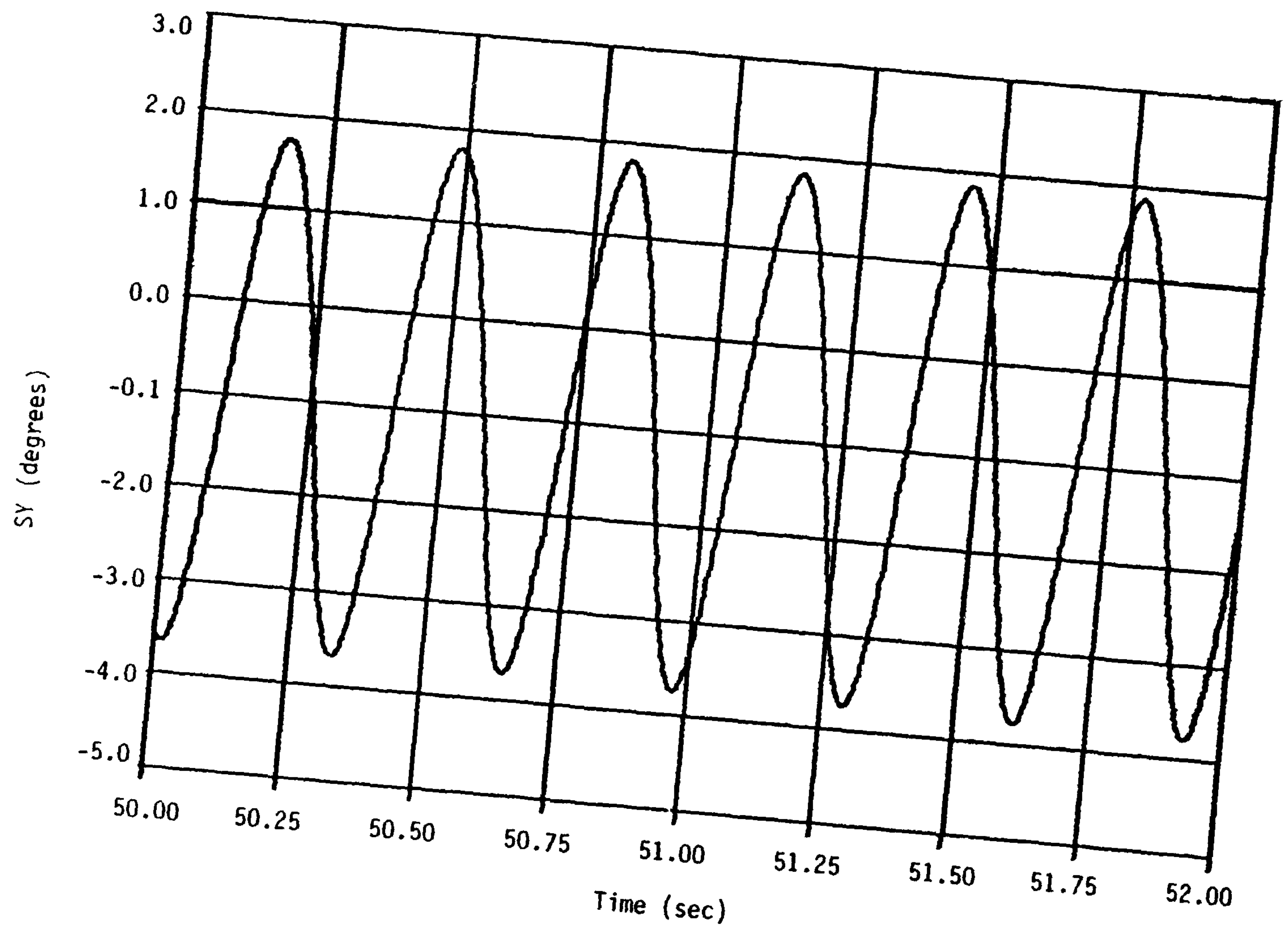

Figure A1b. SY versus time.

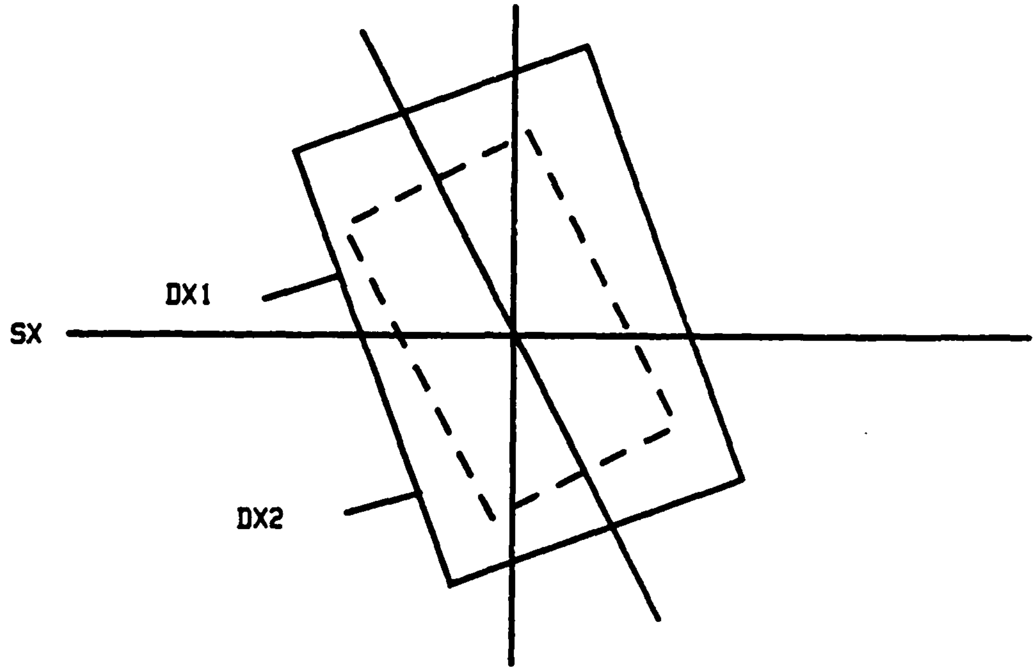

Figure A2a. Sensor outputs: SX = 0, DX1 = minimum, DX2 = maximum.

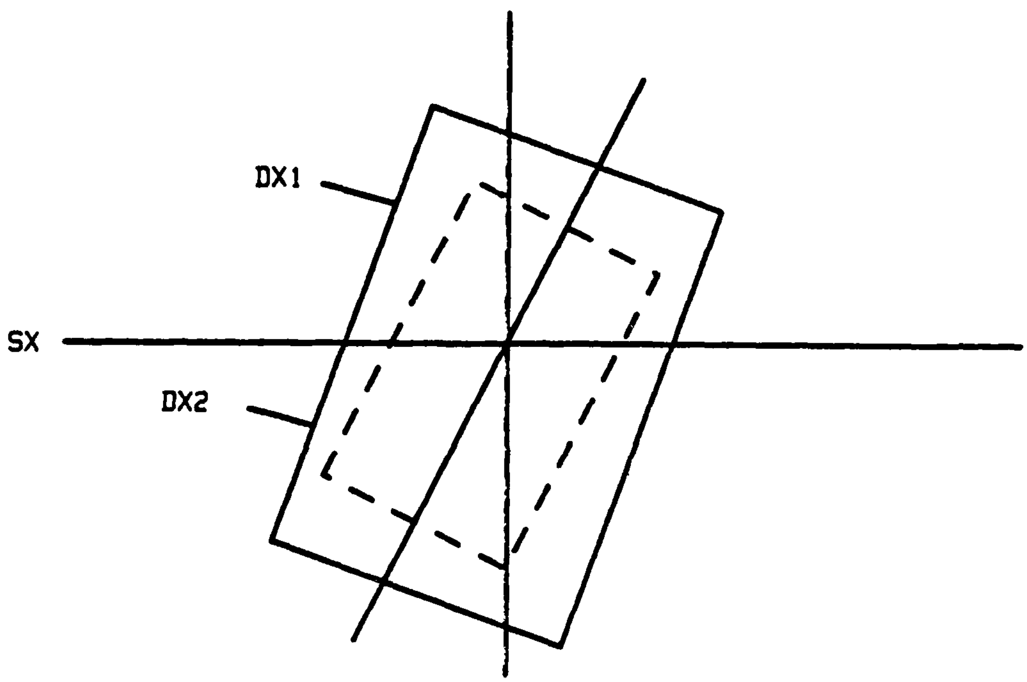

Figure A2b. Sensor outputs: SX = 0, DX1 = maximum, DX2 = minimum.

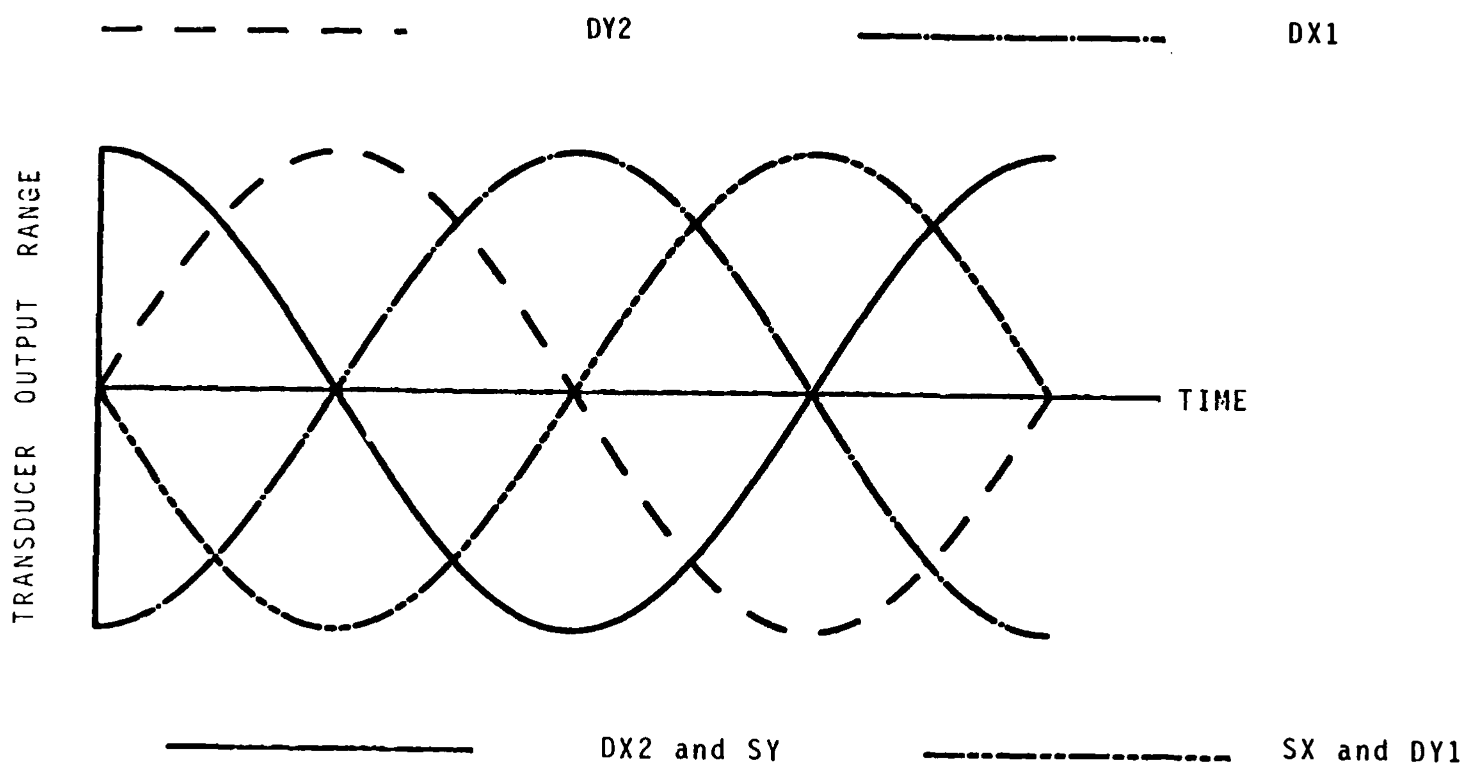

Figure A3. Phase relations for $\phi_\gamma = 0$.

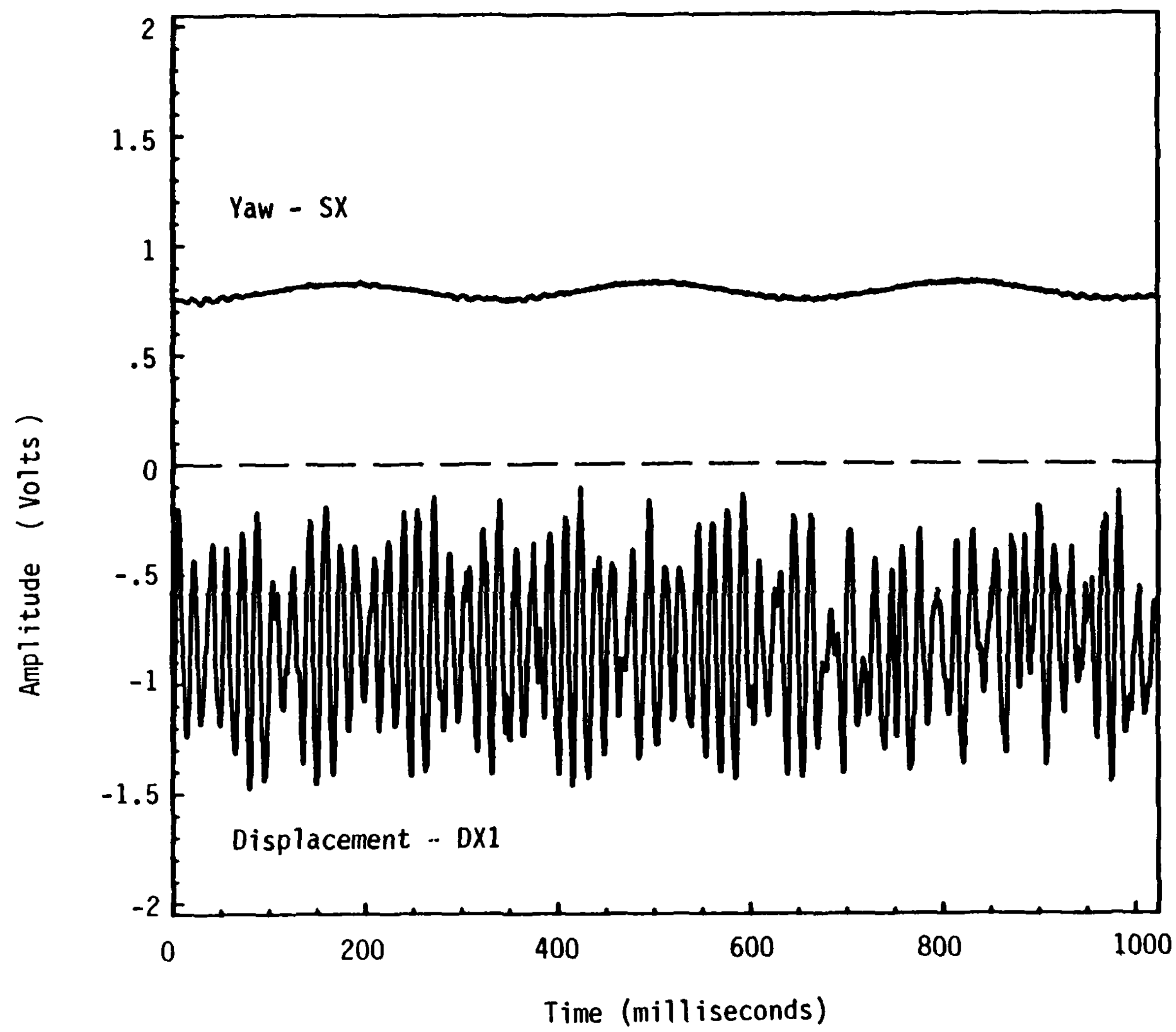

Figure 4Aa. Typical raw analog data for a round shaft at small yaw amplitudes (p = 71.5 Hz, $\dot{\phi}_1$ = 3.31 Hz).

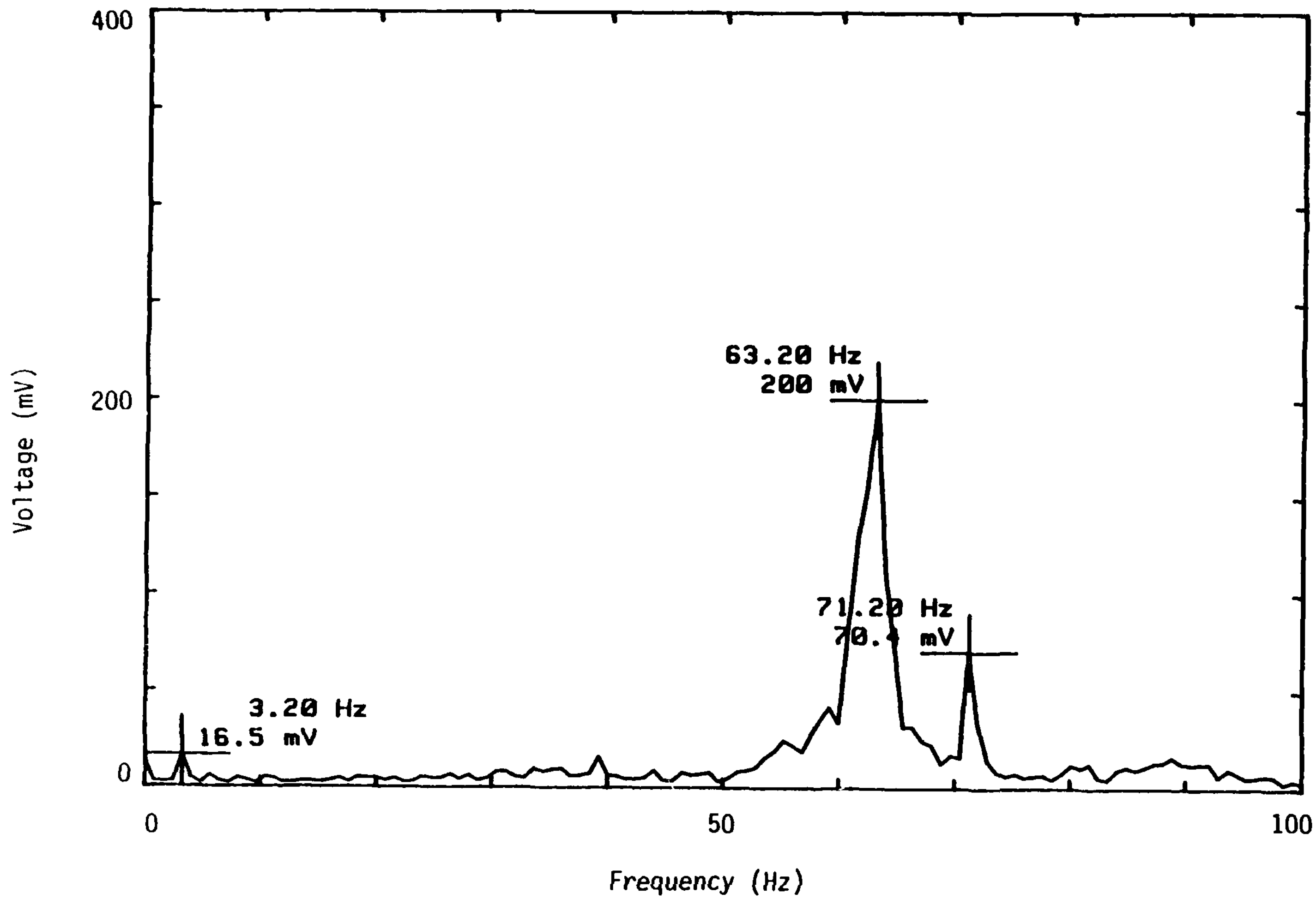

Figure A4b. Frequency spectrum for displacement transducer (DX1).

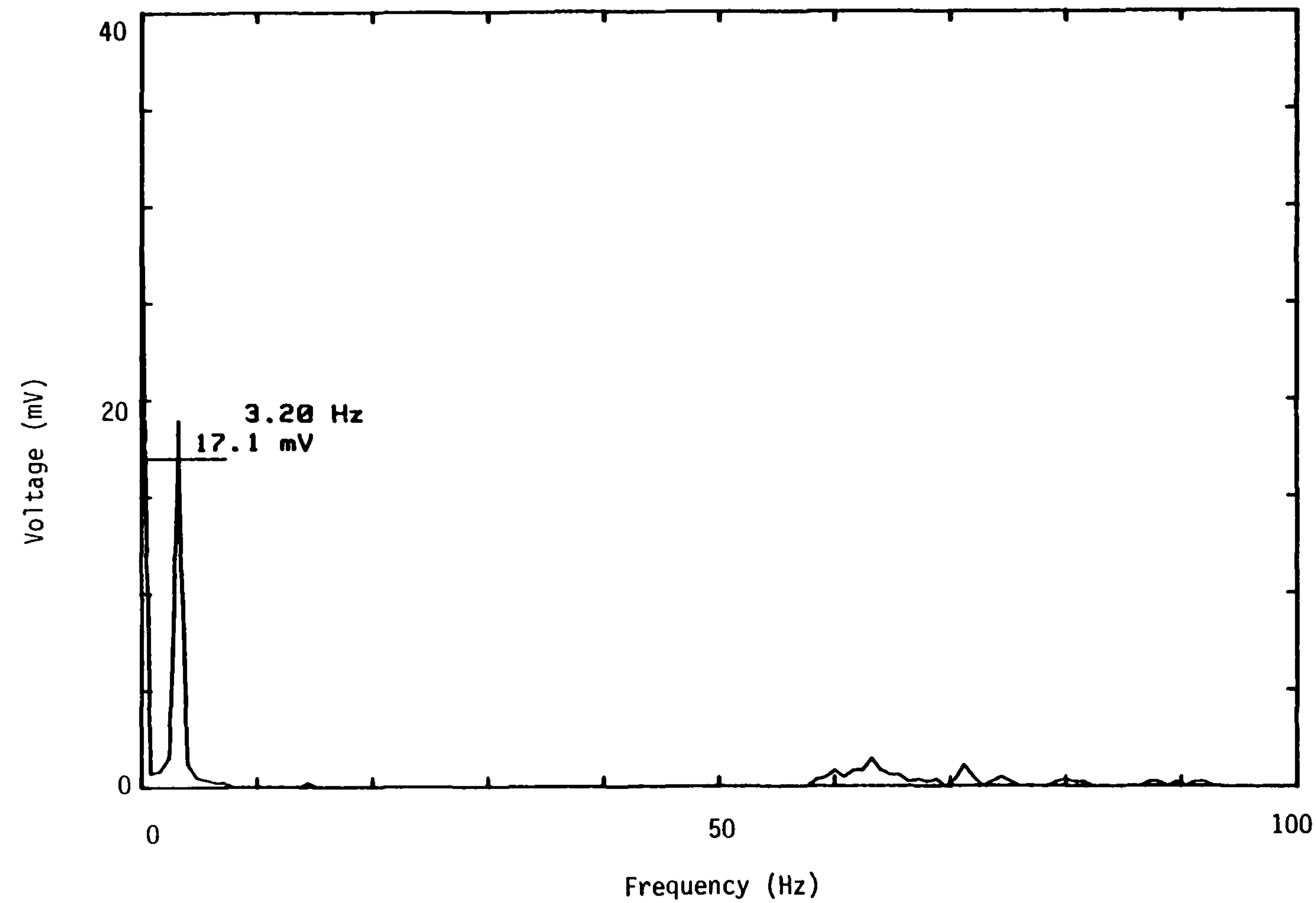

Figure A4c. Frequency spectrum for flexural pivot (SX).

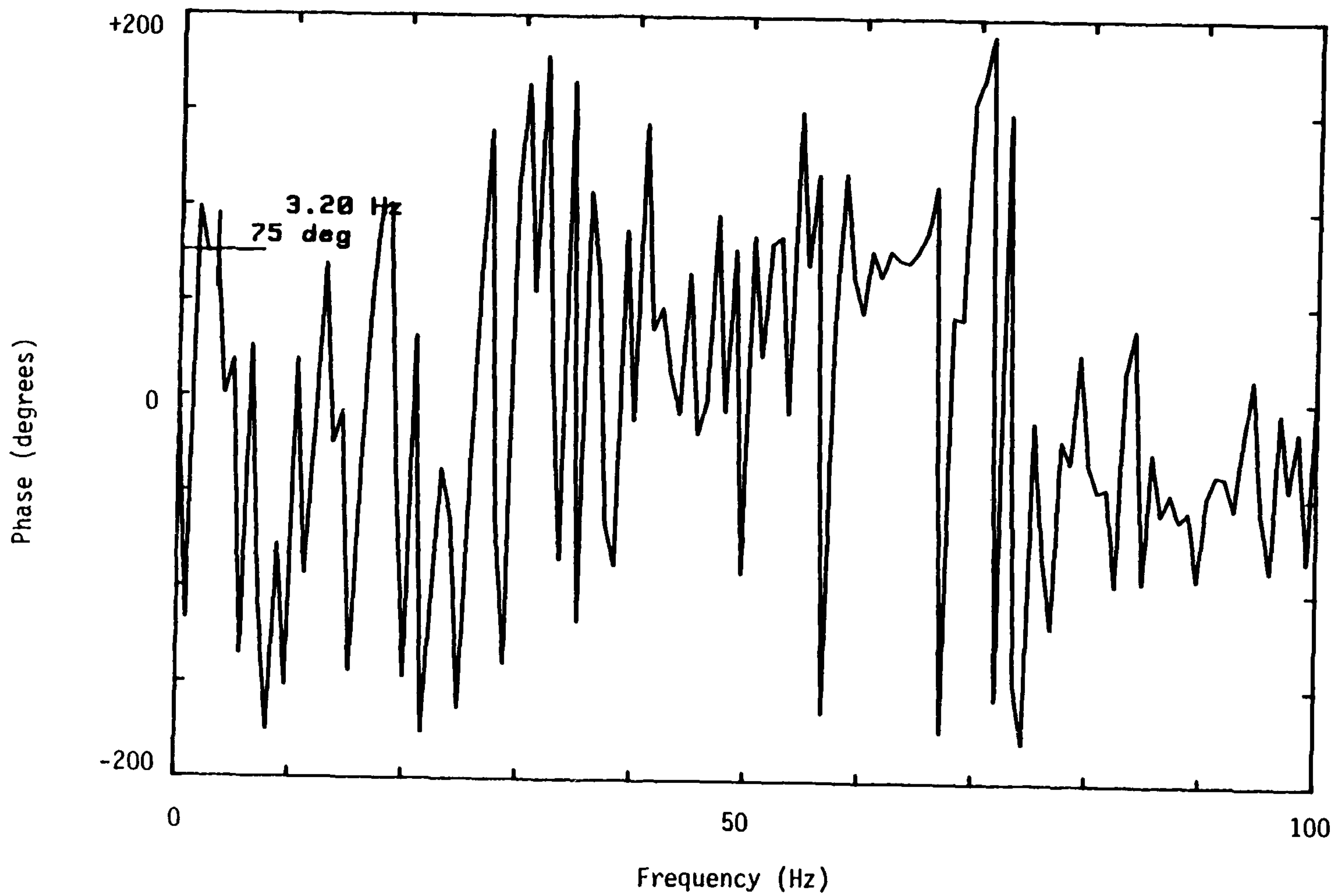

Figure A4d. Phase of DX1 relative to SX via transfer function method.

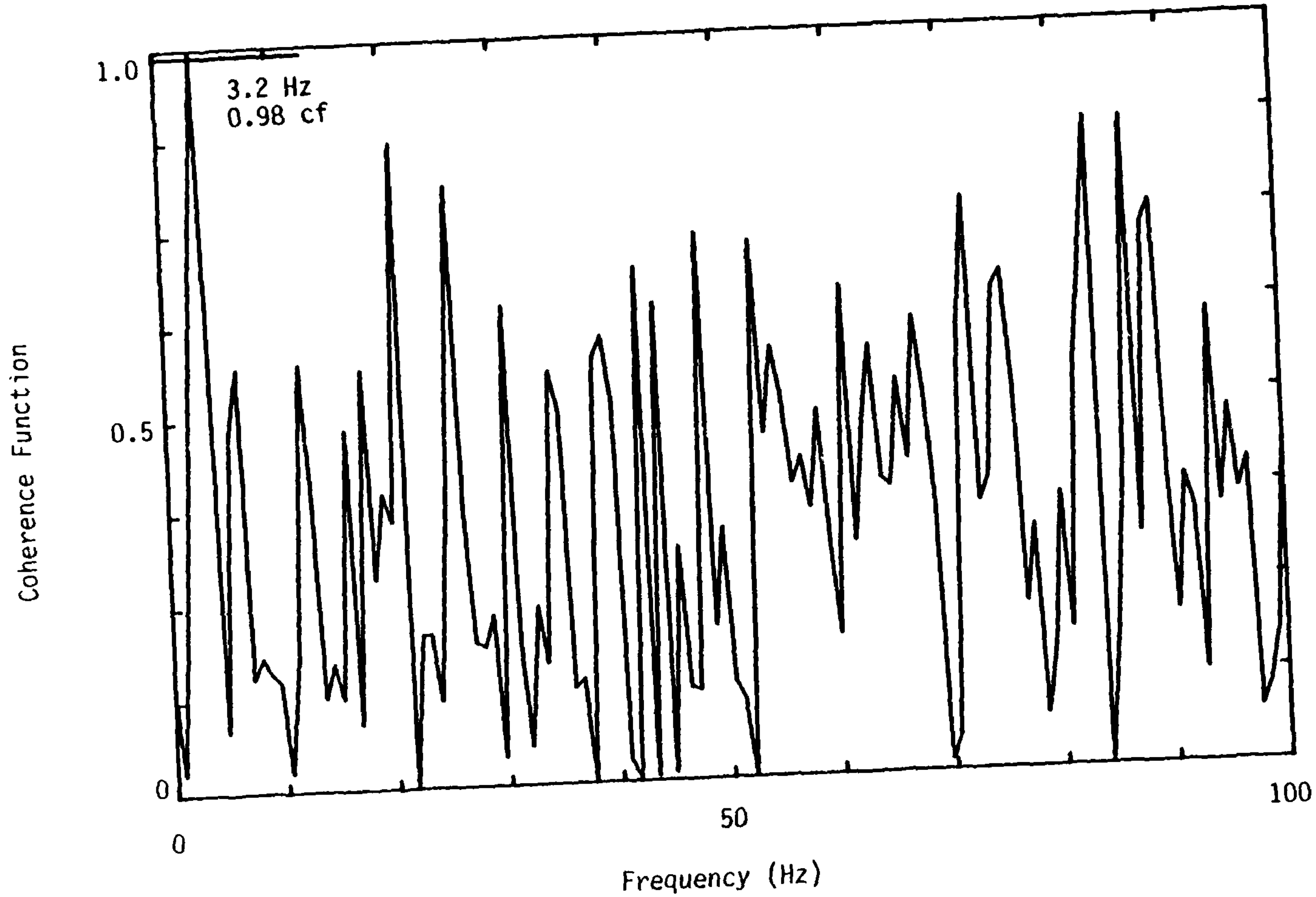

Figure A4e. Coherence function.

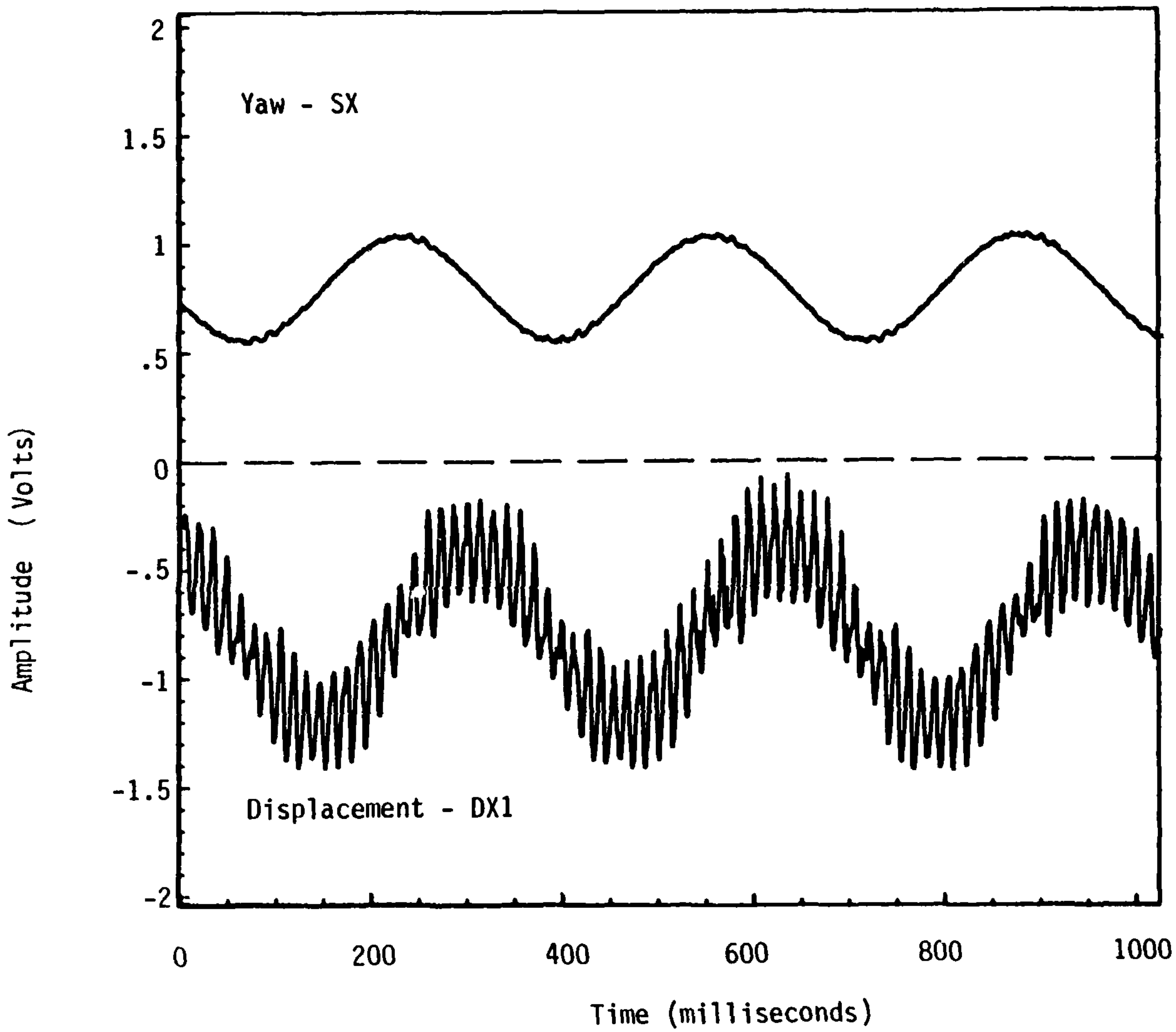

Figure A5a. Typical raw analog data for a round shaft at large yaw amplitudes (p = 71.5 Hz, $\dot{\phi}_1$ = 3.31 Hz).

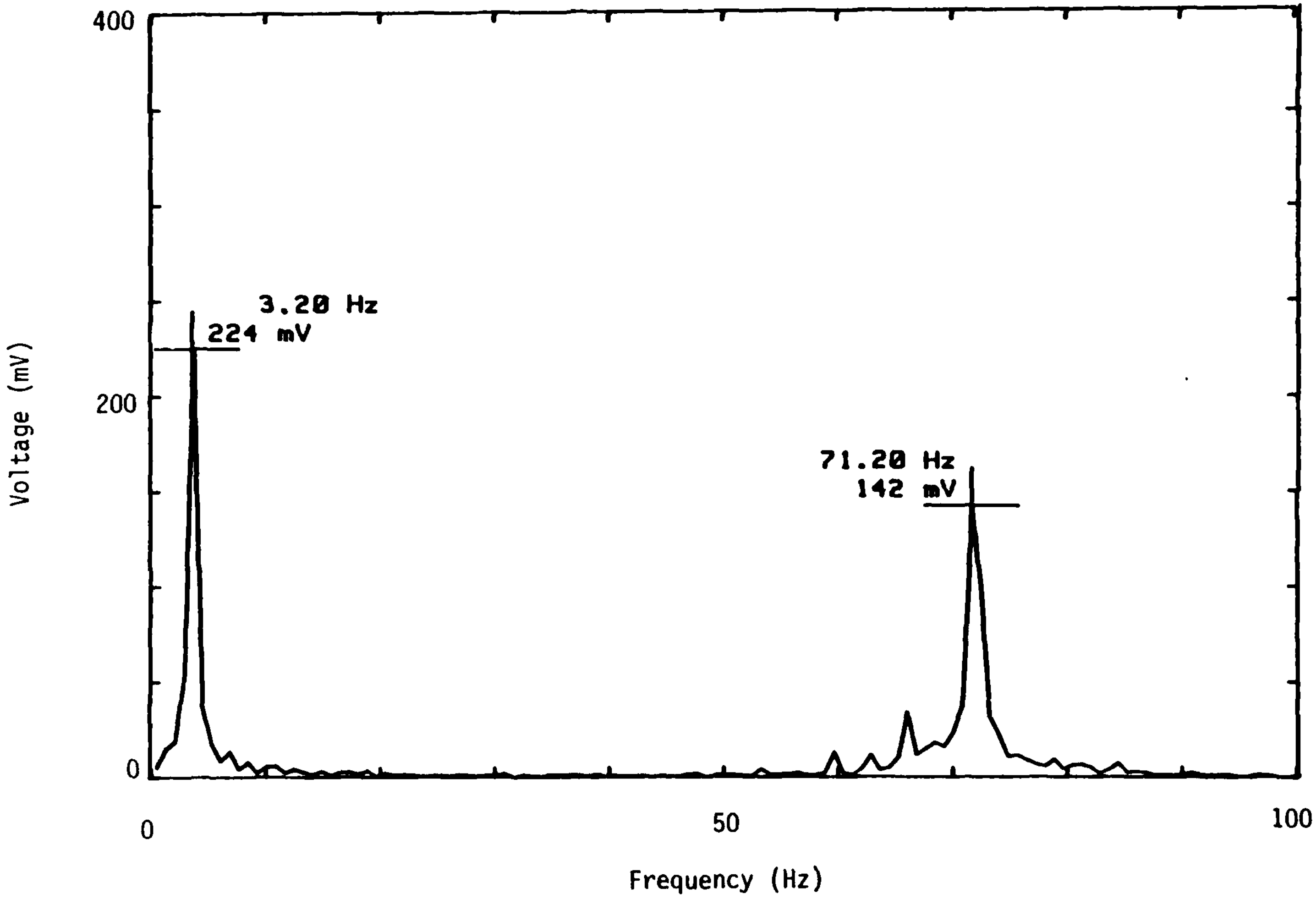

Figure A5b. Frequency spectrum for displacement transducer (DX1).

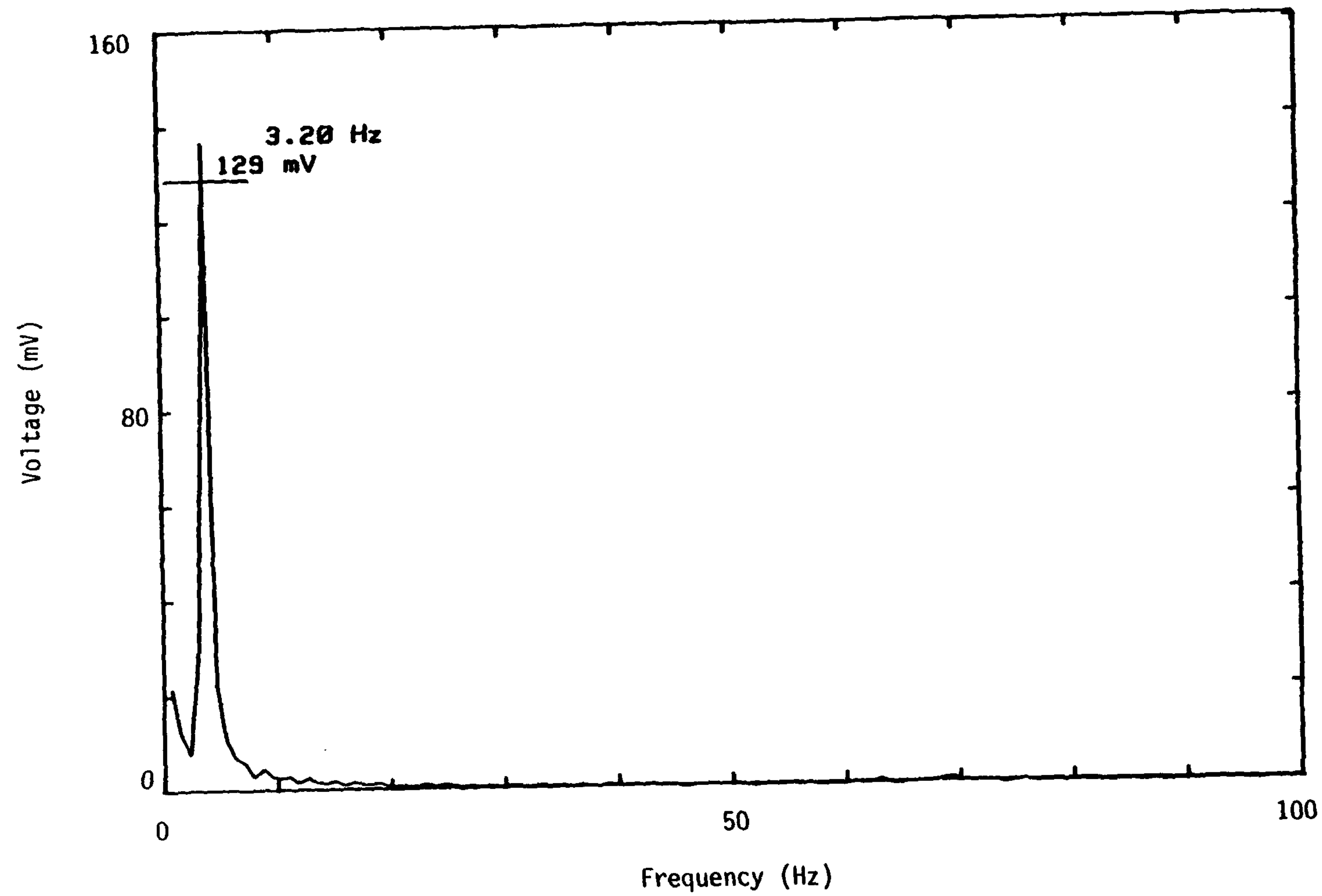

Figure A5c. Frequency spectrum for flexural pivot (SX).

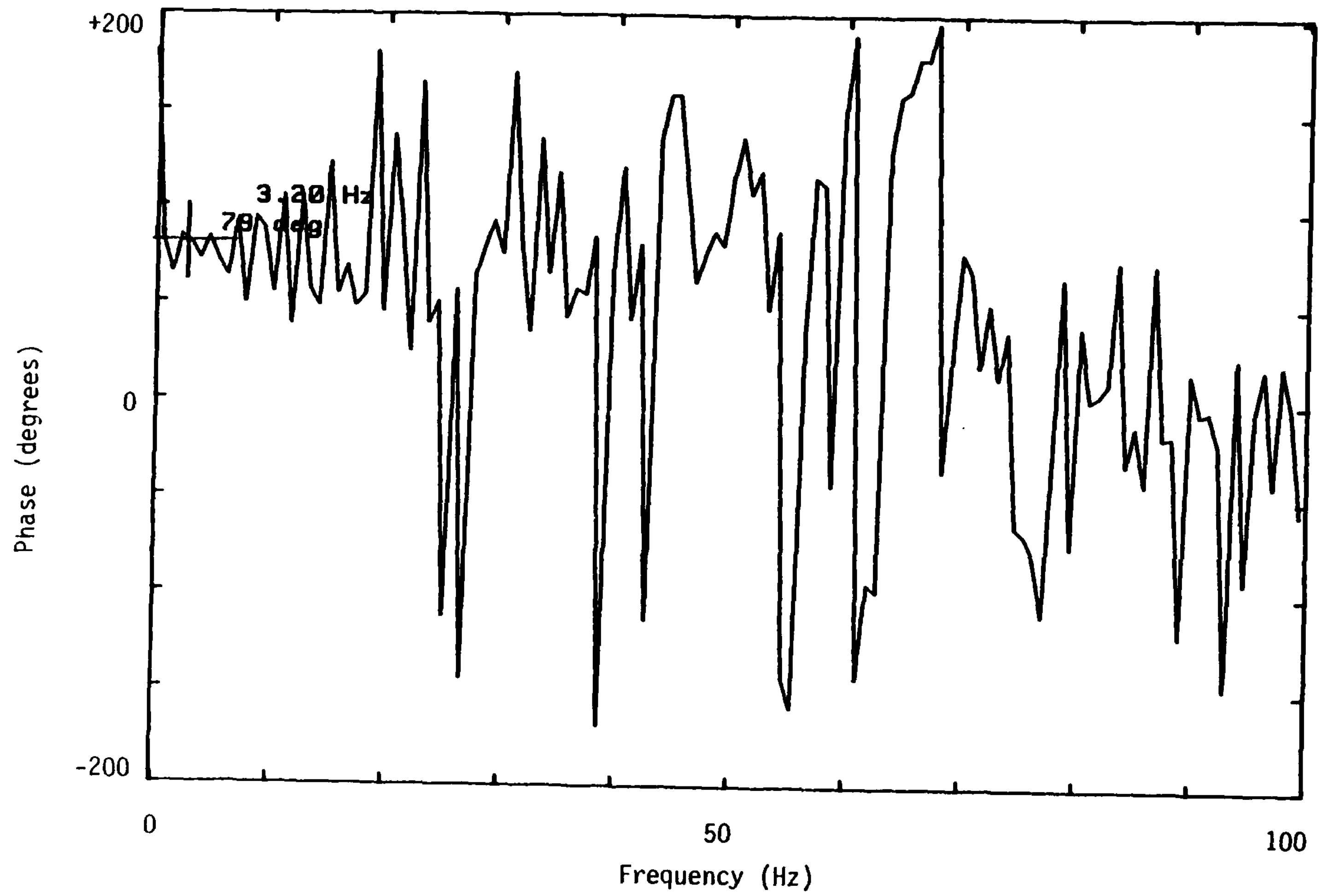

Figure A5d. Phase at DX1 relative to SX via transfer function method.

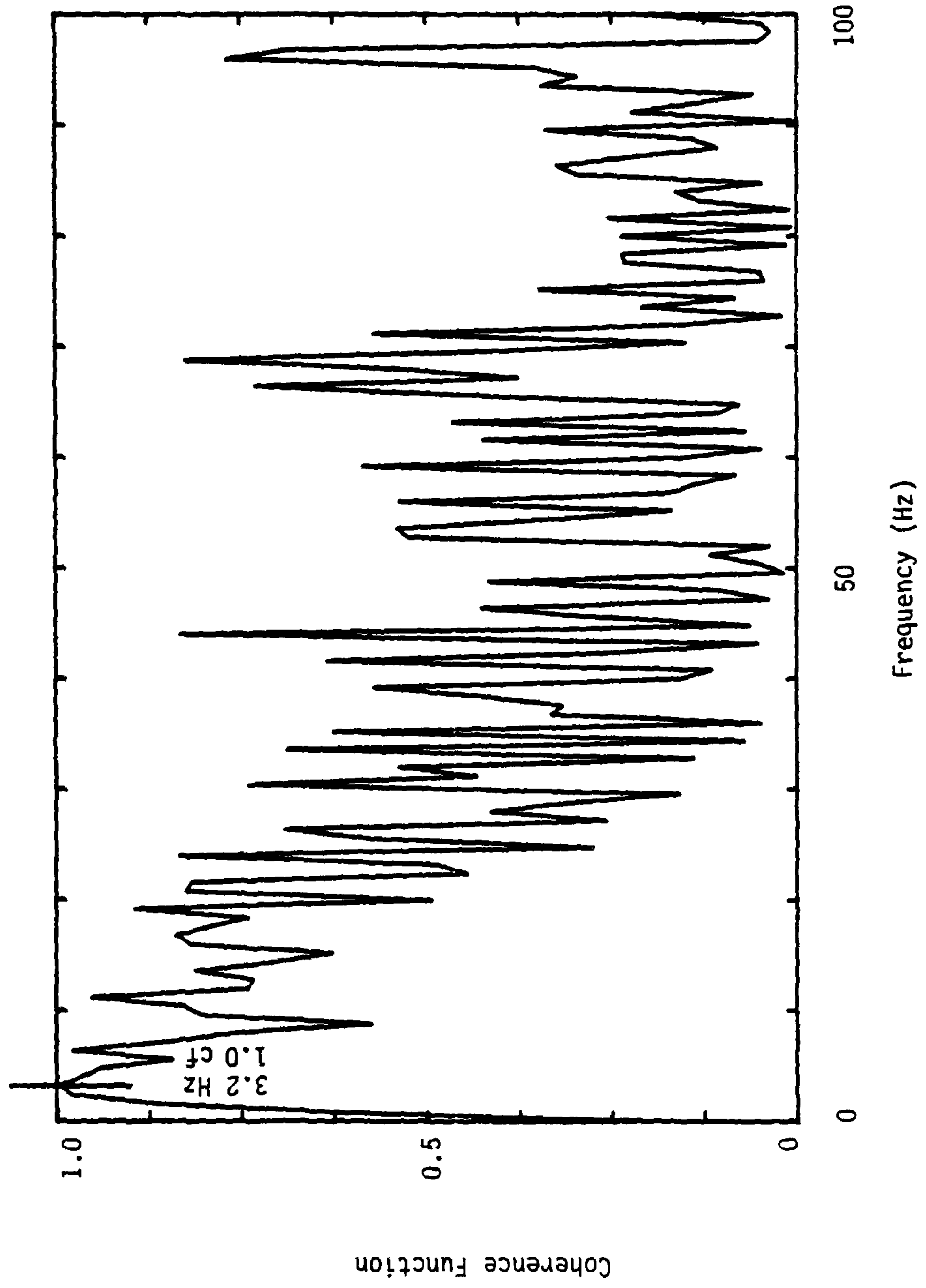

Figure A5e. Coherence function.

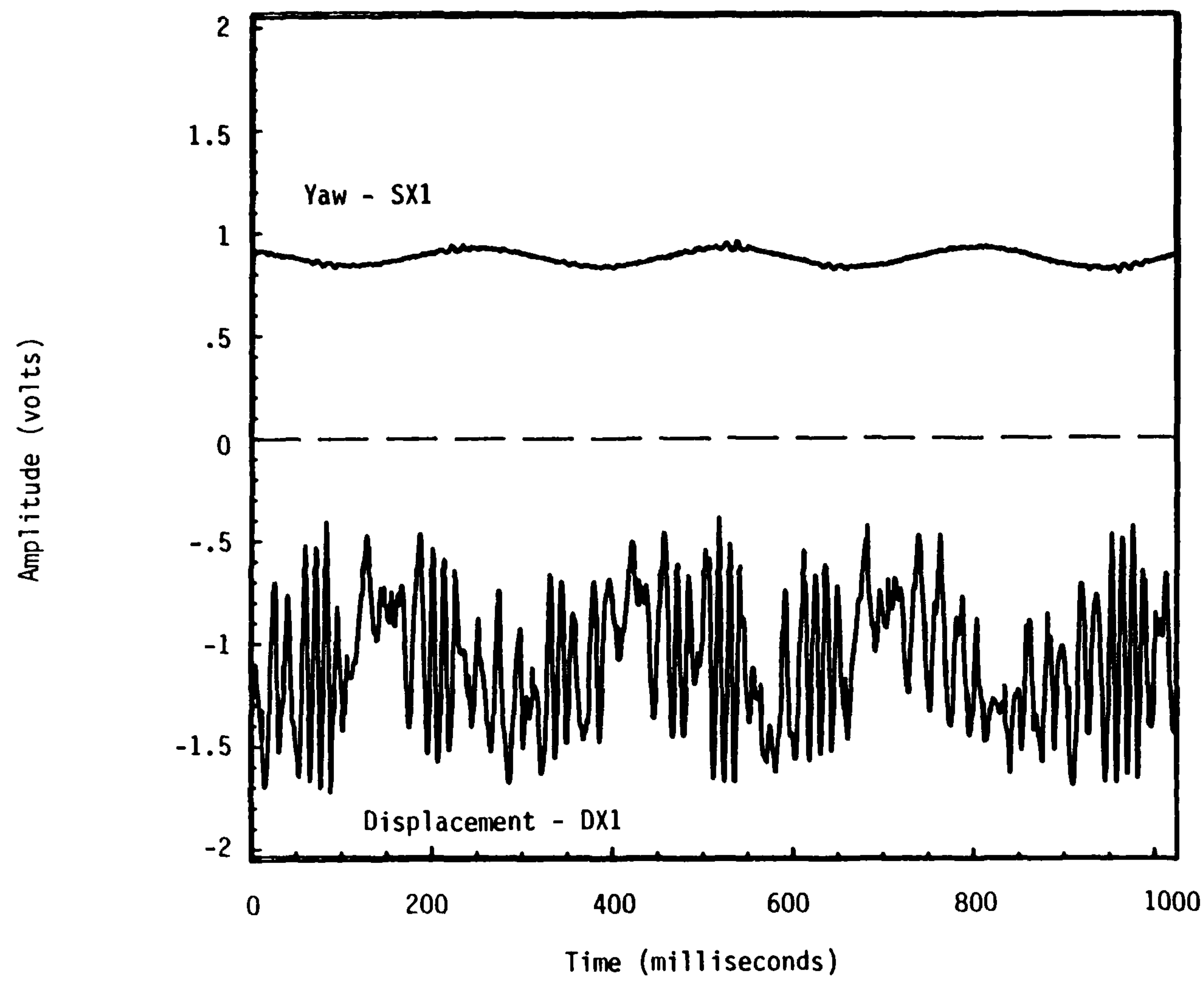

Figure A6a. Typical raw analog data for an octagonal shaft at small yaw amplitudes (p = 75 Hz, $\dot{\phi}_1$ = 3.81 Hz).

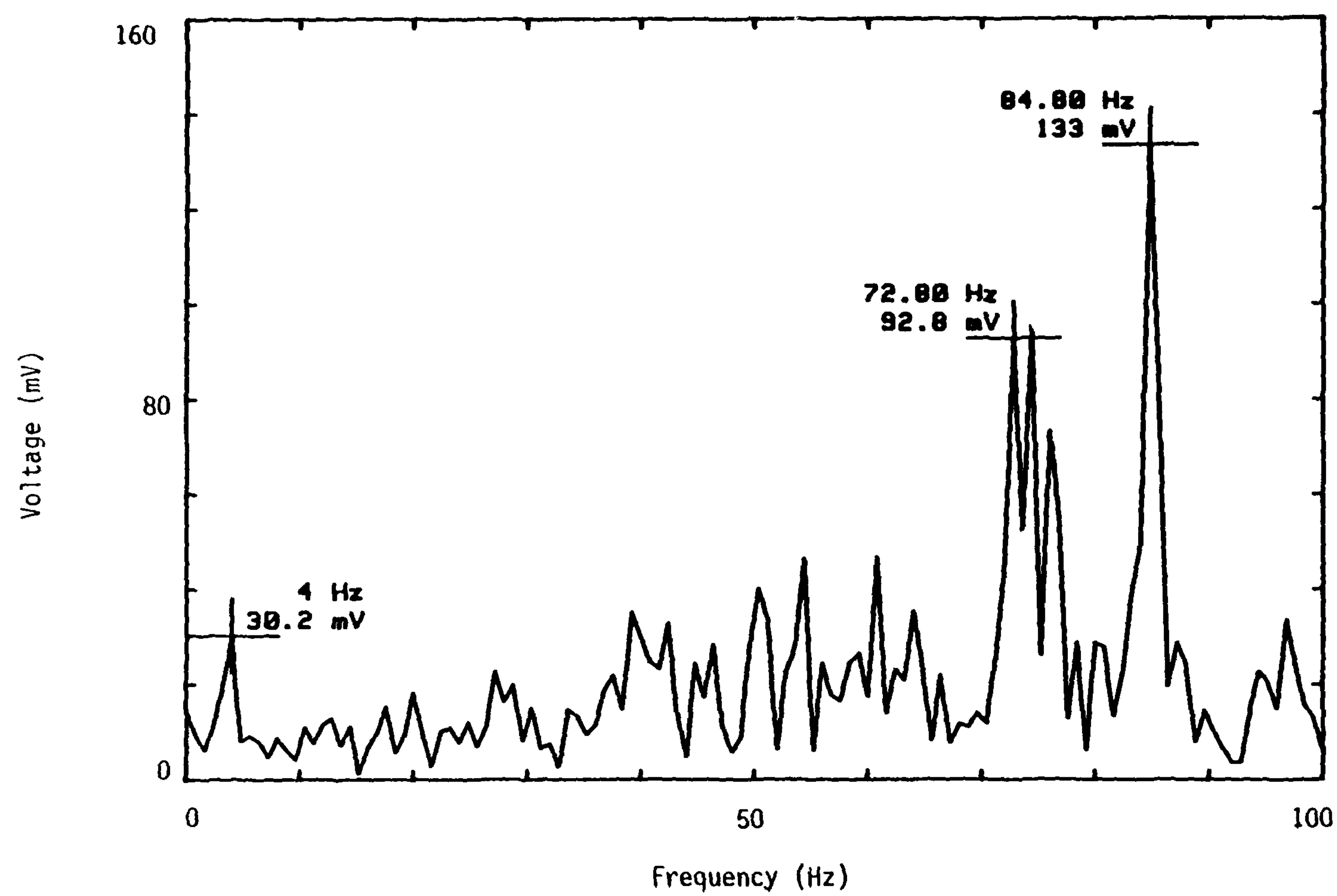

Figure A6b. Frequency spectrum for displacement transducer (DX1).

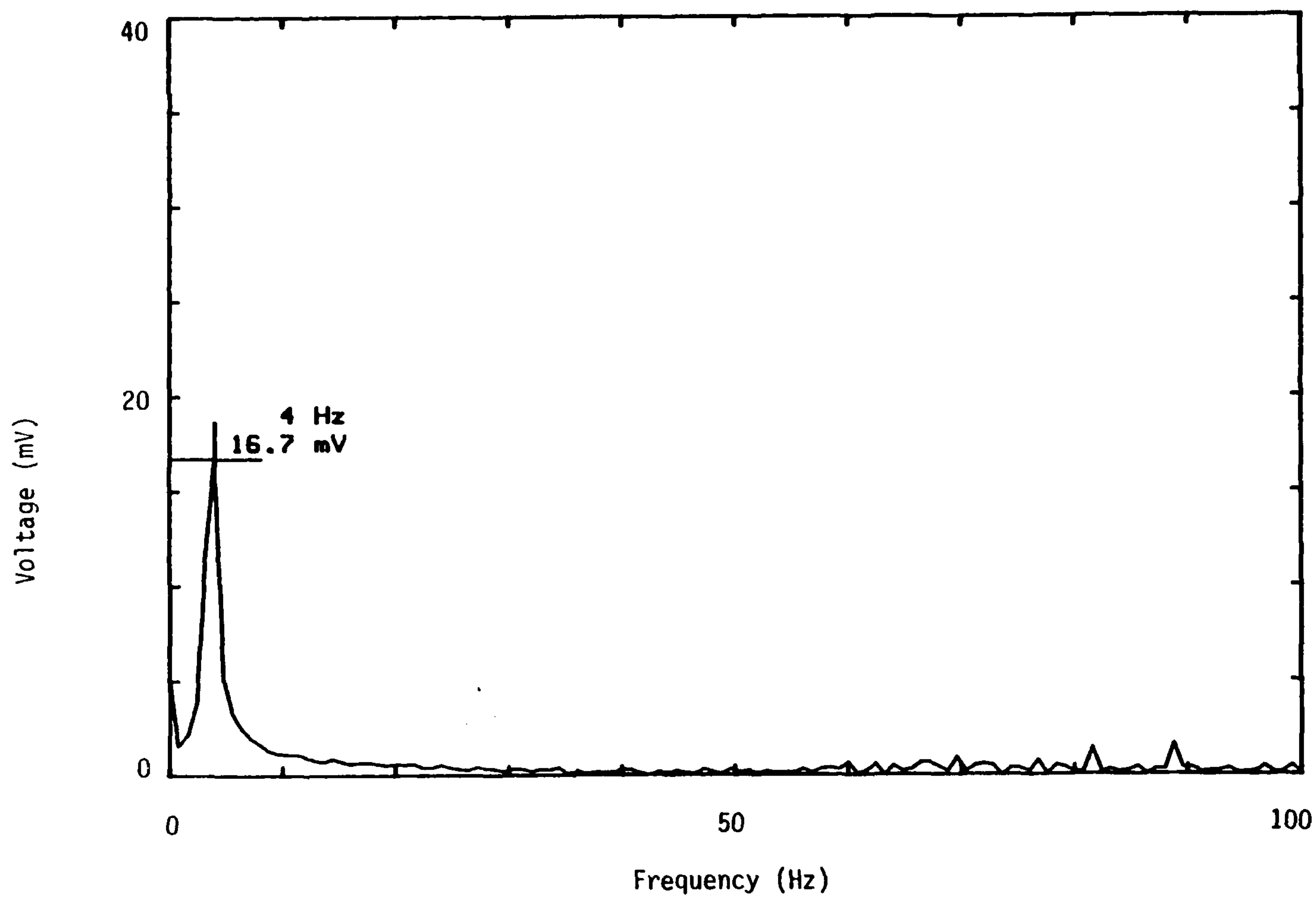

Figure A6c. Frequency spectrum for a flexural pivot (SX).

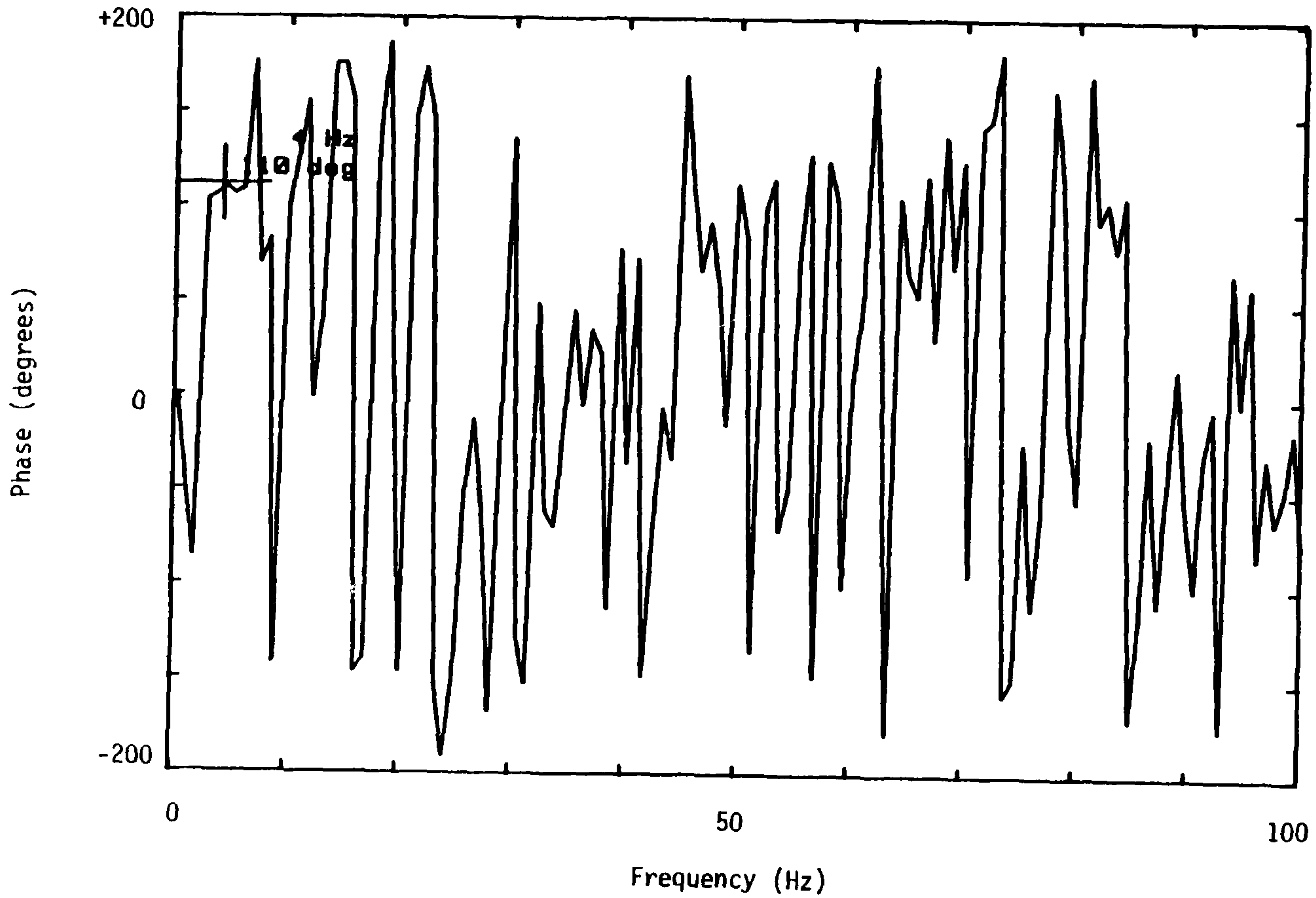

Figure A6d. Phase of DX1 relative to SX via transfer function method.

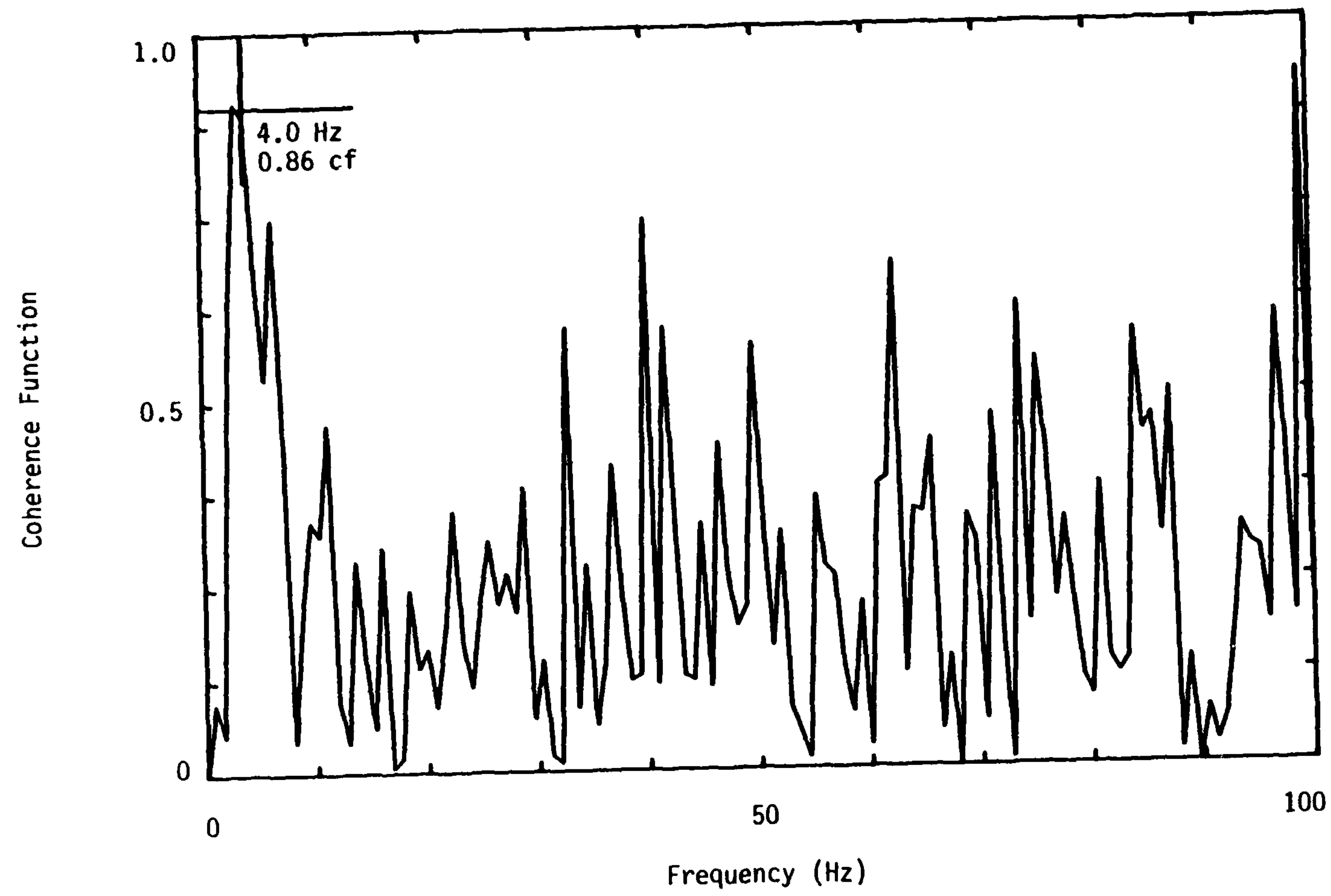

Figure A6e. Coherence function.

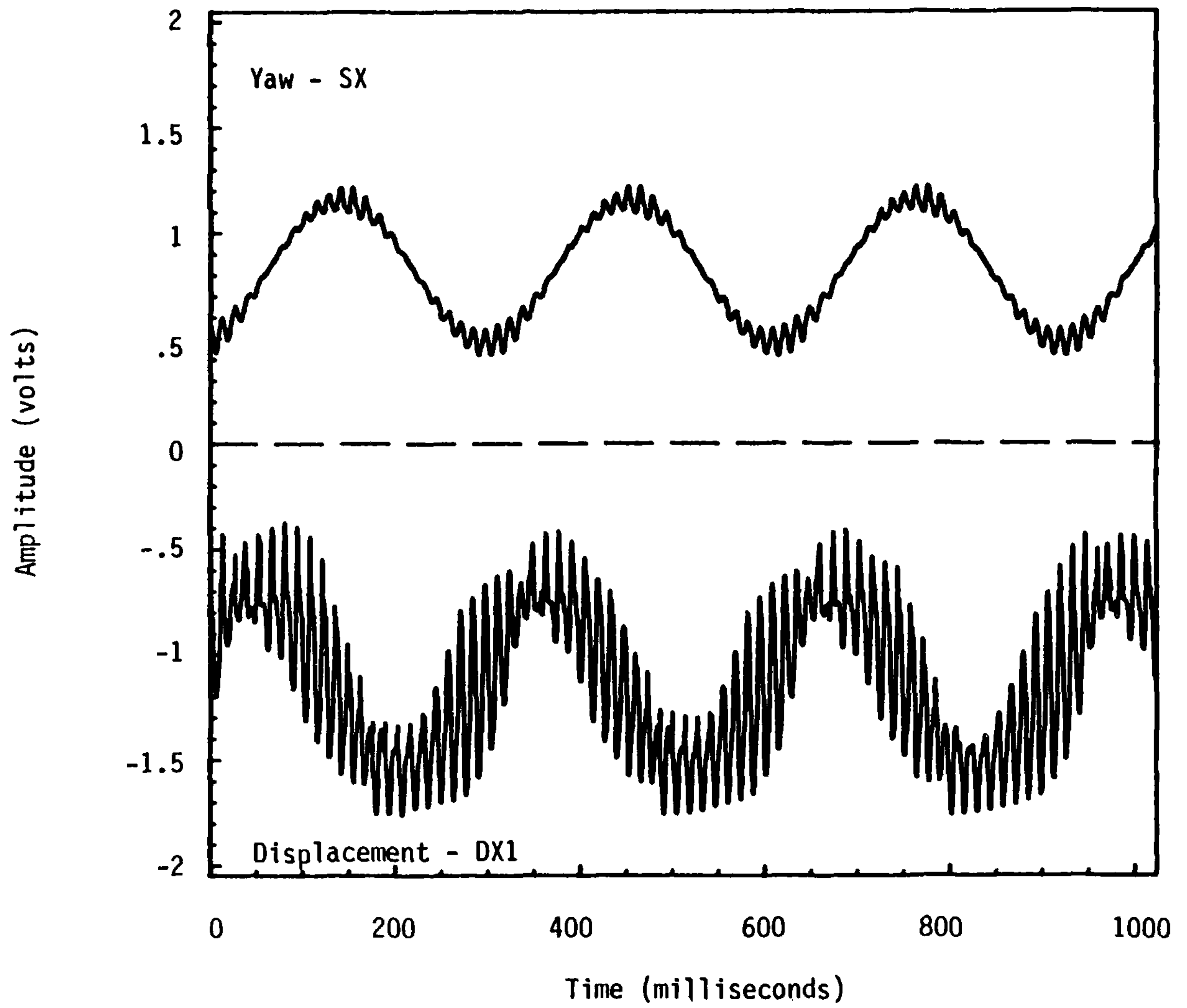

Figure A7a. Typical raw analog data for an octagonal shaft at large yaw amplitudes ($p = 75$ Hz, $\dot{\phi}_1 = 3.81$ Hz).

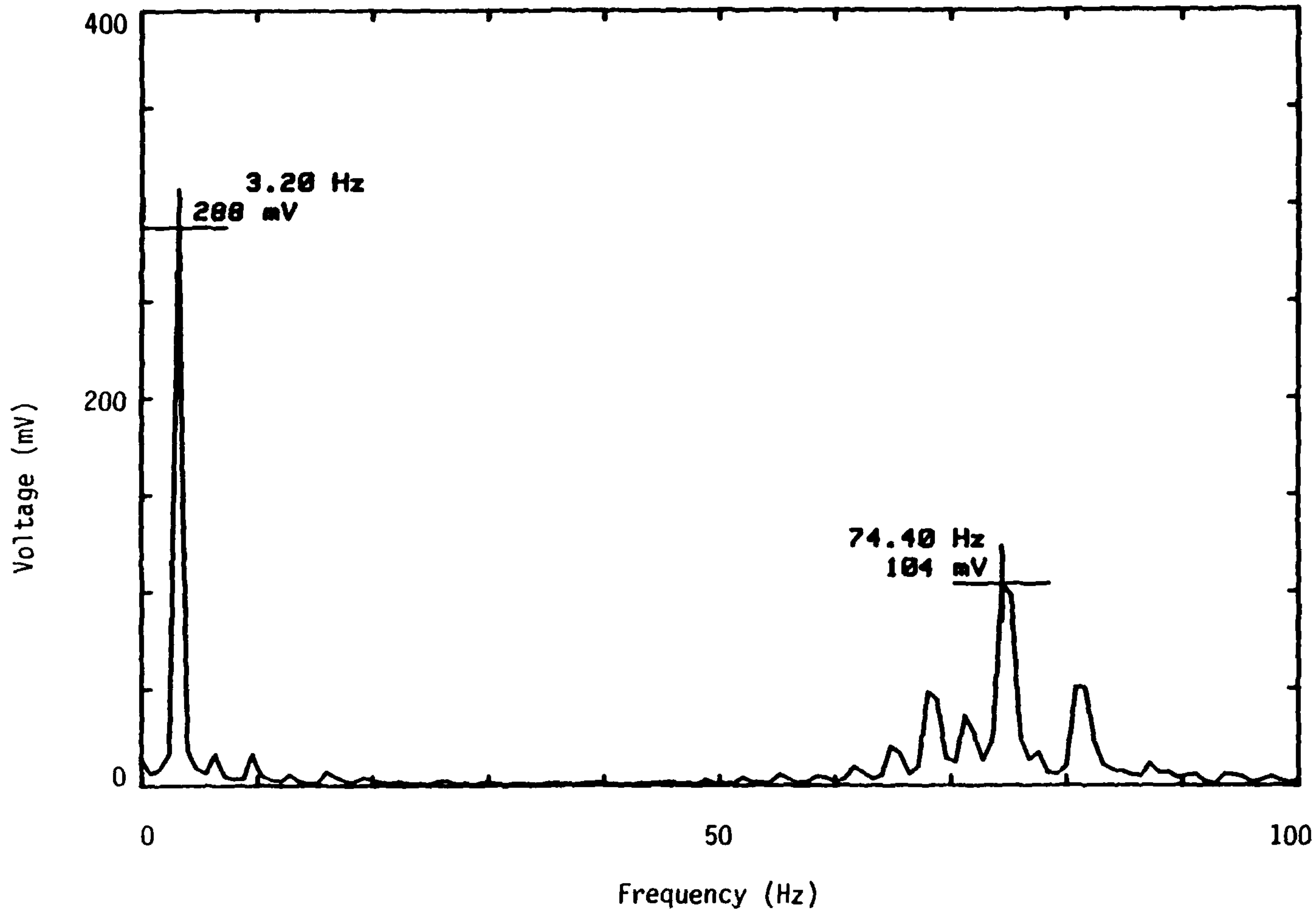

Figure A7b. Frequency spectrum for a displacement transducer (DX1).

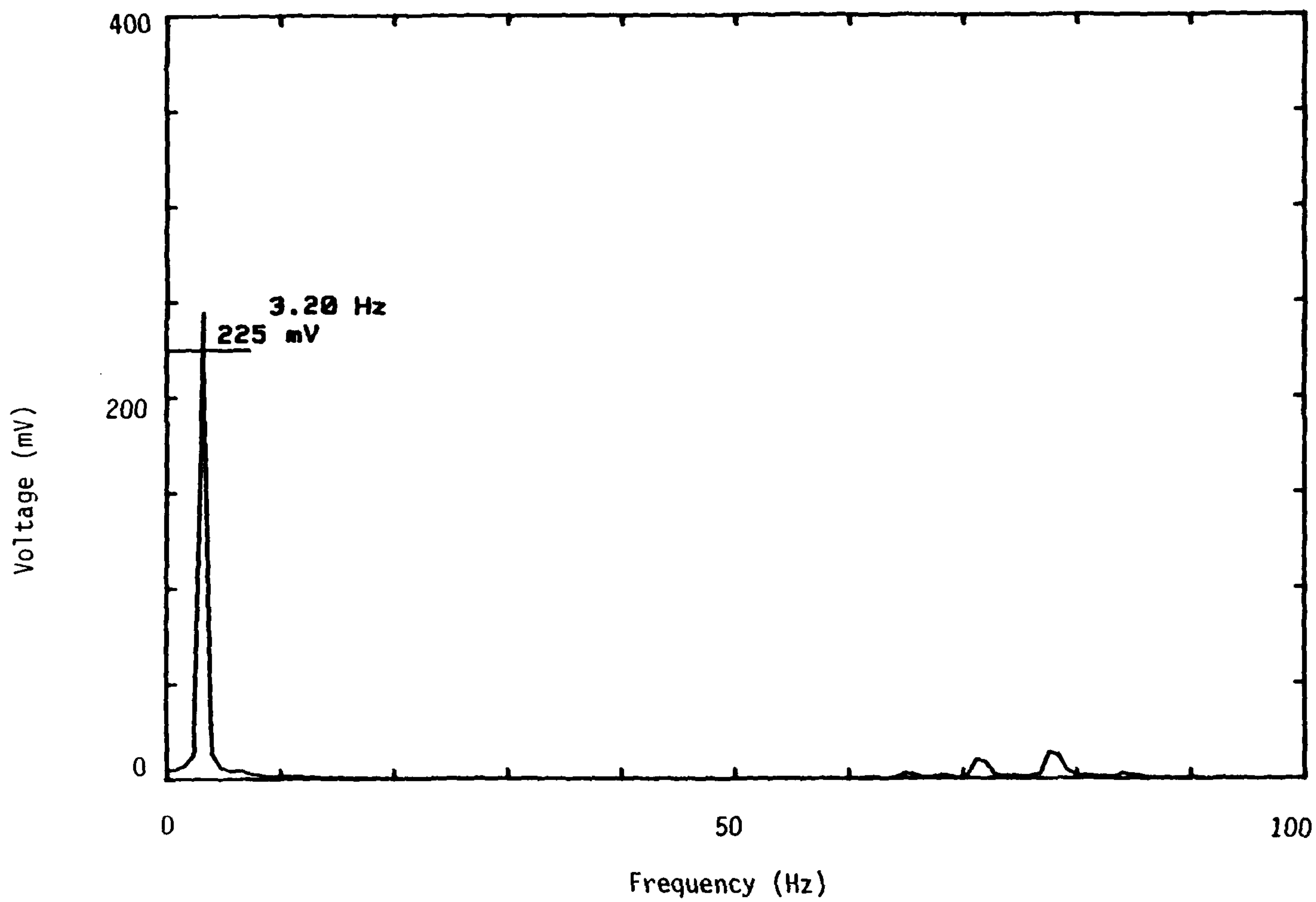

Figure A7c. Frequency spectrum for a flexural pivot (SX).

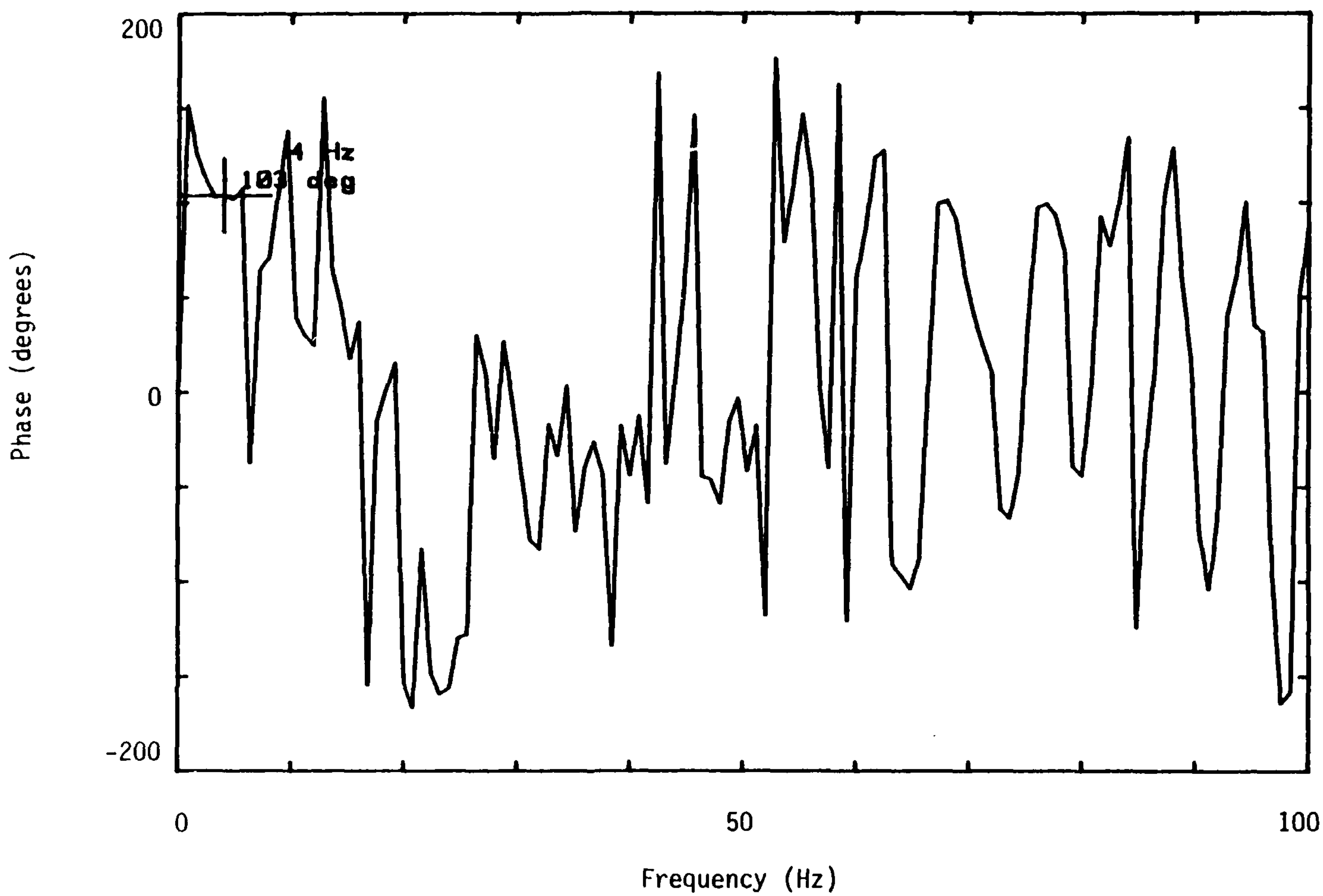

Figure A7d. Phase of DX1 relative to SX via transfer function method.

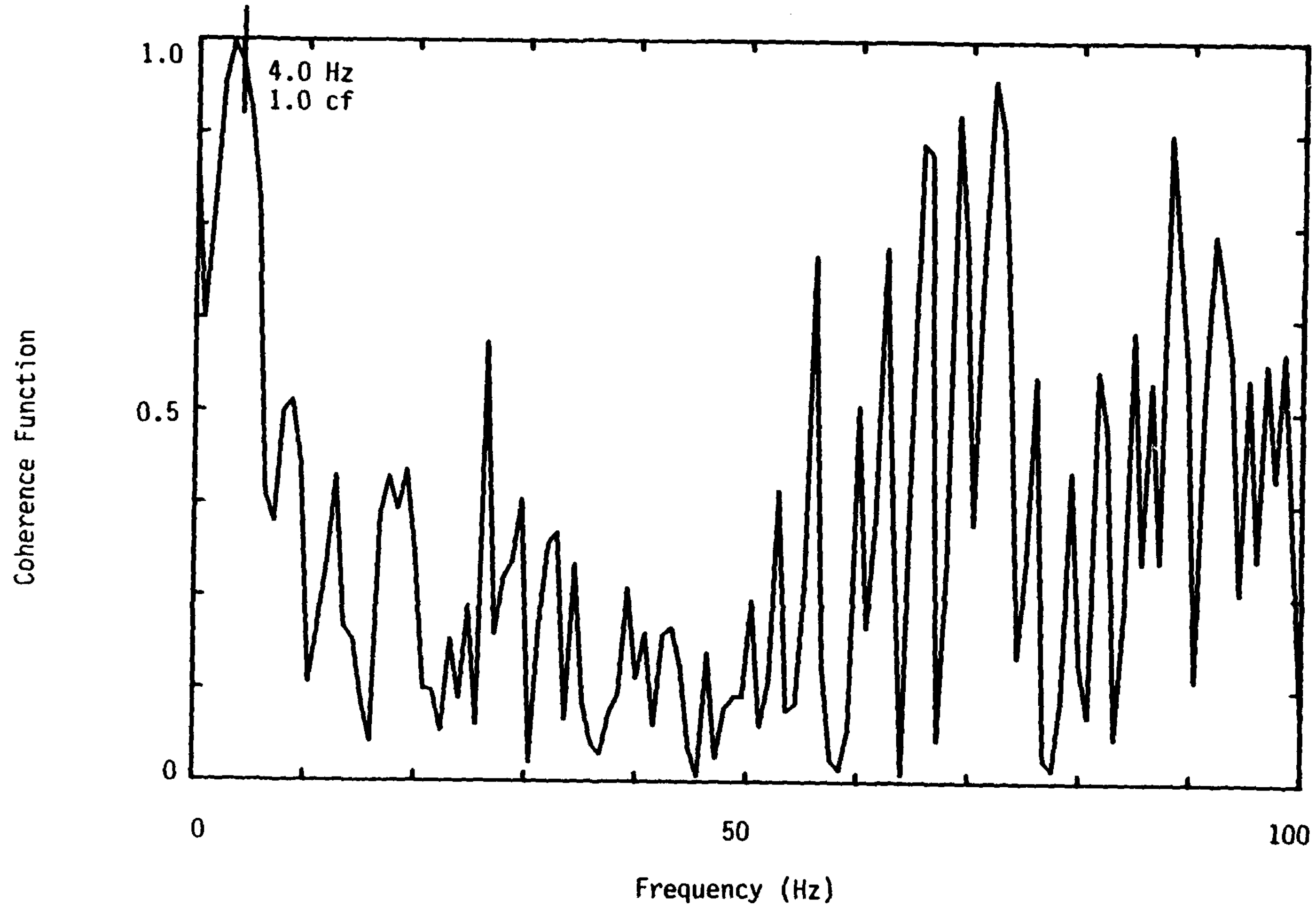

Figure A7e. Coherence function.

APPENDIX B

TARE DATA

APPENDIX B. TARE DATA

Typical tare amplitude/time histories (unfiltered and filtered) are shown in Figures 4 and 5. A determination of tare damping is shown in Figure B1. The tare data were usable only at low spin rates. For spin frequencies above 75 Hz, mechanical vibrations occurred, and the tare damping values were not used. (The PRIM which had been temporarily shimmed and glued to a round shaft had become loose at these higher spin rates.) Trends from lower spin rate data were extrapolated for higher spin rates (Figures B1, B2, and B3). The ratio of the rigid body (or tare) coning and spin frequencies ($\dot{\phi}_{1r}/p$) should be approximately equal to I_a/I_t for a small gravity moment. For the counterweight located at the middle position, $I_a/I_t = 0.0429$. Measured values of $\dot{\phi}_{1r}$ and p (for $p > 70$ Hz) yielded an average value for $\dot{\phi}_{1r}/p$ of 0.0435.

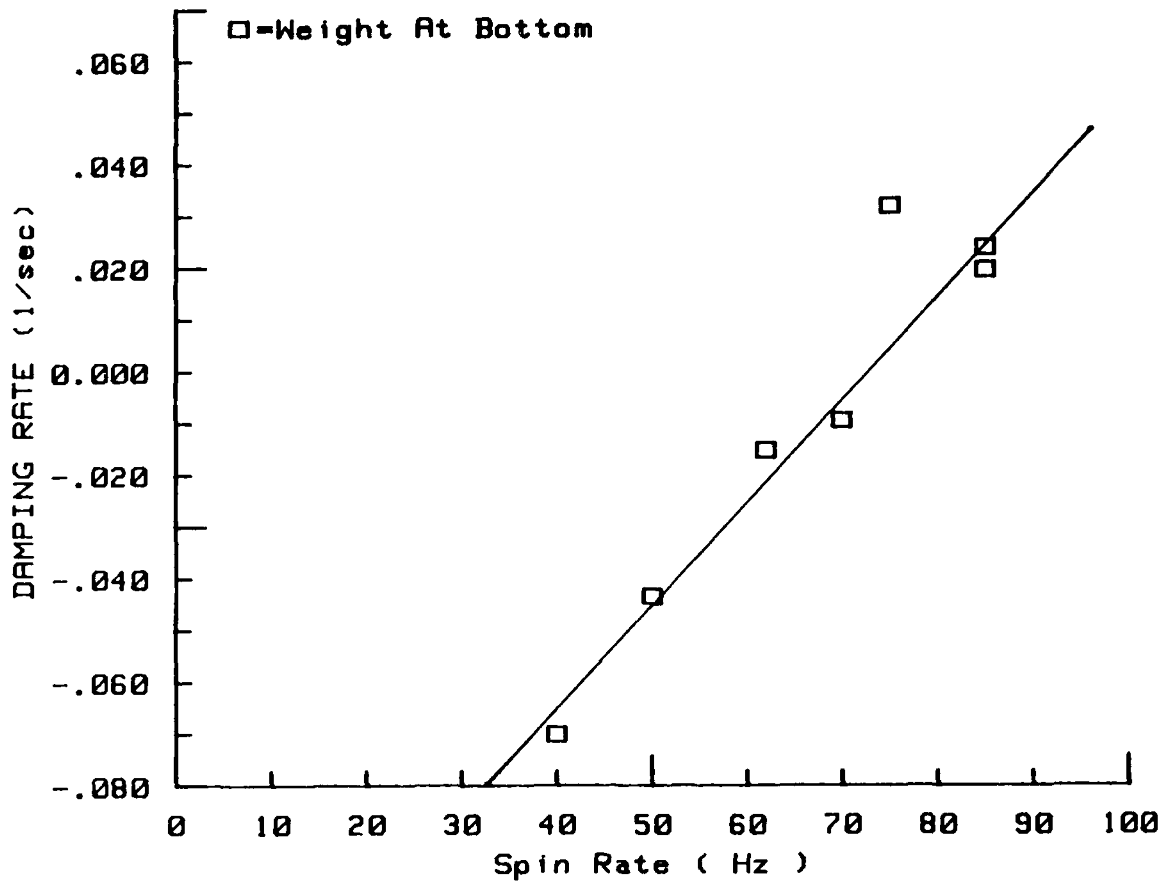

Figure B1. Tare damping for weight at bottom.

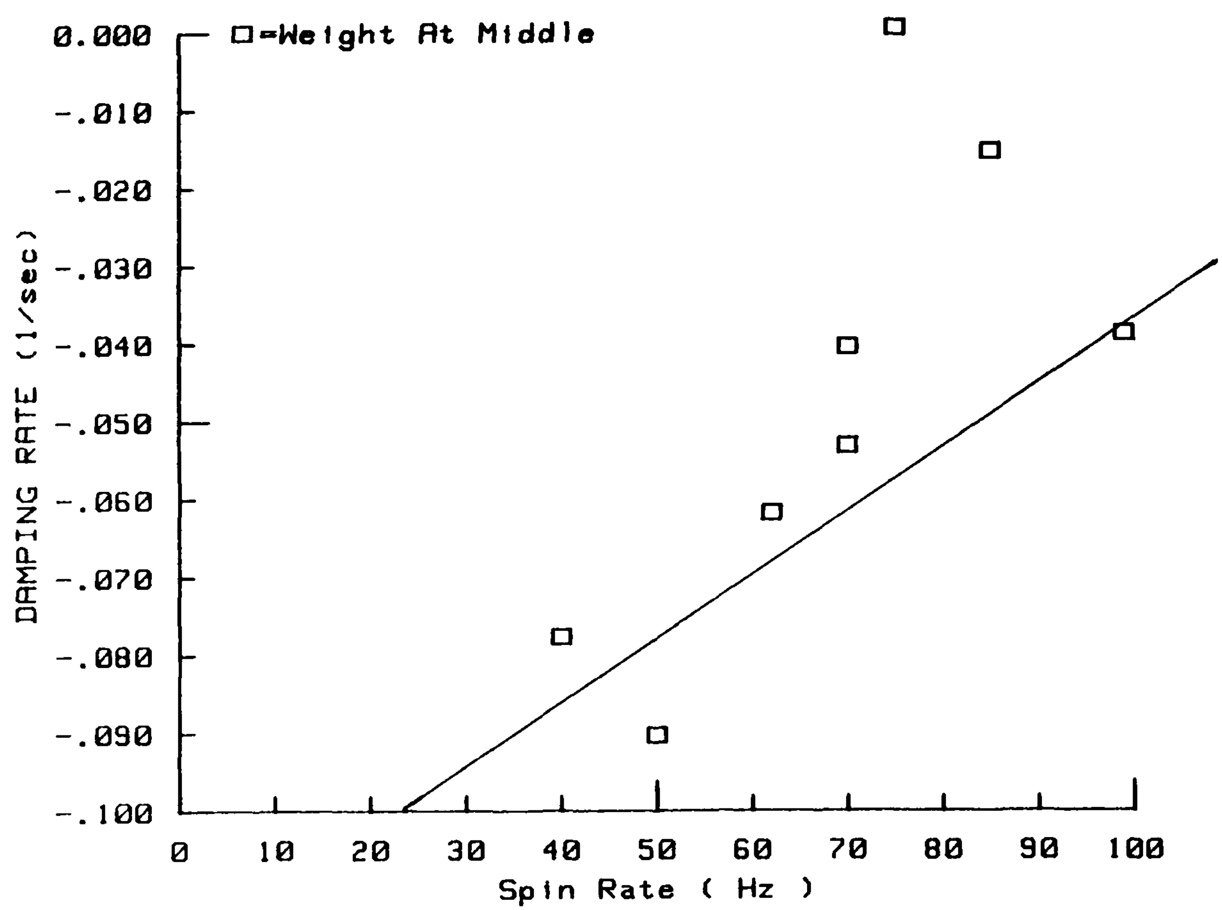

Figure B2. Tare damping for weight at middle.

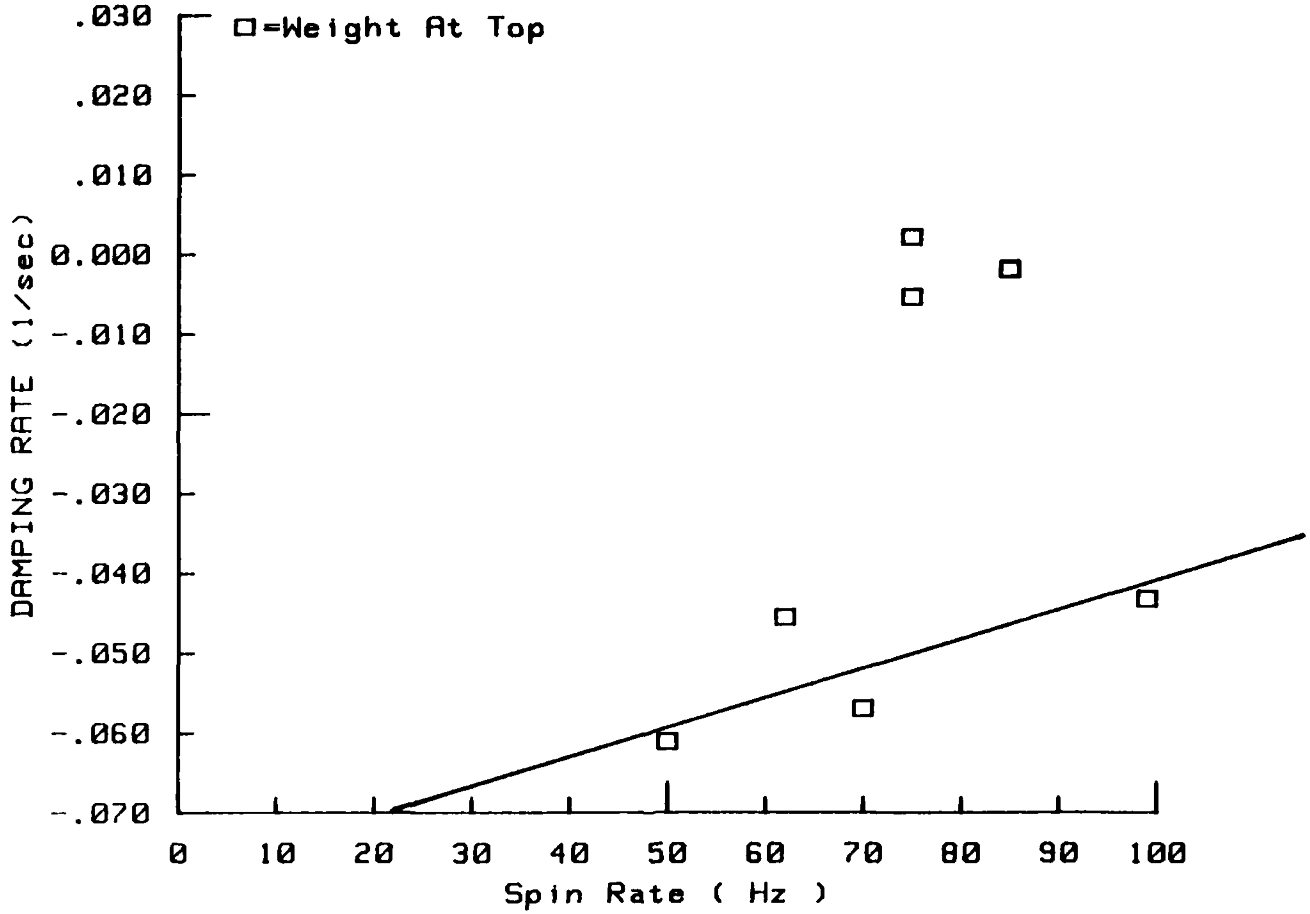

Figure B3. Tare damping for weight at top.

APPENDIX C

DESCRIPTION OF EXPERIMENTS

APPENDIX C. DESCRIPTION OF EXPERIMENTS

Run Name	Shaft/Weight	Clearance (cm/in)	Spin Rate (Hz)	Coning Rate (Hz)	Yaw Record Stable/Unstable
4P0	Round/M	0.0127/0.005	71.5	3.31	Unstable
4P0A	Round/M	0.0127/0.005	71.5	3.40	Unstable
4P1	Round/M	0.0127/0.005	62.0	2.79	Stable
4P2	Round/M	0.0127/0.005	86.0	3.82	Unstable
4P2A	Round/M	0.0127/0.005	86.0	3.87	Unstable
5P0	Round/B	0.0127/0.005	62.0	3.67	Stable
5P1	Round/B	0.0127/0.005	75.0	NA	Unstable
5P1A	Round/B	0.0127/0.005	75.0	3.58	Unstable
5P2	Round/B	0.0127/0.005	85.0	4.03	Unstable
5P2A	Round/B	0.0127/0.005	86.0	3.96	Unstable
6P0	Round/T	0.0127/0.005	62.0	2.50	Stable
6P0A	Round/T	0.0127/0.005	62.0	2.50	Stable
6P1	Round/T	0.0127/0.005	75.0	3.15	Unstable
6P1A	Round/T	0.0127/0.005	75.0	NA	Unstable
6P2	Round/T	0.0127/0.005	85.0	3.45	Unstable
6P2A	Round/T	0.0127/0.005	85.0	3.29	Unstable
7P0	Round/T	0.0254/0.010	62.0	2.86	Stable
7P0A	Round/T	0.0254/0.010	62.0	2.71	Stable
7P1	Round/T	0.0254/0.010	50.0	2.03	Stable
7P1A	Round/T	0.0254/0.010	50.0	2.00	Stable
7P2A	Round/T	0.0254/0.010	70.0	2.80	Unstable
7P2B	Round/T	0.0254/0.010	70.0	2.84	Unstable
8P0	Round/B	0.0254/0.010	50.0	2.43	Stable
8P0A	Round/B	0.0254/0.010	50.0	2.45	Stable
8P1	Round/B	0.0254/0.010	62.0	NA	Unstable
8P1A	Round/B	0.0254/0.010	62.0	3.14	Unstable
8P2	Round/B	0.0254/0.010	70.0	3.33	Unstable
8P2A	Round/B	0.0254/0.010	70.0	3.55	Unstable
9P0	Round/M	0.0254/0.010	50.0	2.20	Stable
9P0A	Round/M	0.0254/0.010	50.0	2.24	Stable
9P1	Round/M	0.0254/0.010	62.0	2.89	Unstable
9P1A	Round/M	0.0254/0.010	62.0	2.67	Unstable
9P2	Round/M	0.0254/0.010	70.0	3.08	Unstable
9P2A	Round/M	0.0254/0.010	70.0	3.02	Unstable
9P3	Round/M	0.0254/0.010	80.0	4.65	Unstable
10P0	Round/M	0.0381/0.015	40.0	1.79	Stable
10P0A	Round/M	0.0381/0.015	40.0	1.80	Stable
10P1	Round/M	0.0381/0.015	50.0	NA	Unstable
10P1A	Round/M	0.0381/0.015	50.0	2.39	Unstable
10P2	Round/M	0.0381/0.015	60.0	NA	Stable
10P3	Round/M	0.0381/0.015	65.0	2.87	Unstable
10P3A	Round/M	0.0381/0.015	65.0	2.96	Unstable
11P0	Round/B	0.0381/0.015	40.0	NA	Stable
11P0A	Round/B	0.0381/0.015	40.0	2.02	Stable
11P1	Round/B	0.0381/0.015	50.0	2.53	Unstable
11P1A	Round/B	0.0381/0.015	50.0	2.62	Unstable
11P2	Round/B	0.0381/0.015	65.0	NA	Unstable

Run Name	Shaft/Weight	Clearance (cm/in)	Spin Rate (Hz)	Coning Rate (Hz)	Yaw Record Stable/Unstable
12P0	Round/T	0.0381/0.015	40.0	NA	Stable
12P0A	Round/T	0.0381/0.015	40.0	1.65	Stable
12P1	Round/T	0.0381/0.015	50.0	NA	NA
12P2	Round/T	0.0381/0.015	65.0	NA	NA
13P0	Octagon/B	0.0127/0.005	62.0	3.00	Stable
13P0A	Octagon/B	0.0127/0.005	62.0	NA	Stable
13P1	Octagon/B	0.0127/0.005	75.0	3.58	Unstable
13P1A	Octagon/B	0.0127/0.005	75.0	NA	Unstable
13P2	Octagon/B	0.0127/0.005	85.0	NA	Unstable
13P2A	Octagon/B	0.0127/0.005	85.0	4.38	Unstable
14P0	Octagon/M	0.0127/0.005	62.0	2.72	Stable
14P0A	Octagon/M	0.0127/0.005	62.0	2.59	Stable
14P1	Octagon/M	0.0127/0.005	75.0	NA	NA
14P1A	Octagon/M	0.0127/0.005	75.0	NA	NA
14P2	Octagon/M	0.0127/0.005	85.0	3.81	Unstable
14P2A	Octagon/M	0.0127/0.005	85.0	NA	Unstable
15P0	Octagon/T	0.0127/0.005	85.0	2.69	Stable
15P0A	Octagon/T	0.0127/0.005	85.0	NA	Stable
15P1	Octagon/T	0.0127/0.005	75.0	NA	NA
15P1A	Octagon/T	0.0127/0.005	75.0	NA	NA
15P2	Octagon/T	0.0127/0.005	85.0	3.38	Unstable
15P2A	Octagon/T	0.0127/0.005	85.0	3.27	Unstable

APPENDIX D-I

ROUND SHAFT RAW DATA

APPENDIX D-I. ROUND SHAFT RAW DATA

4P0 Round/.005/M/71.5

Time (sec)	Yaw (deg)	ϕ_γ (deg)	Orbit (mm)	Orbit (in)	Spin (Hz)	Coning (Hz)	Wt Pos	Growth Rates (1/s) exp	Growth Rates (1/s) tare	Tare Con (Hz)
23	.47	168	.0635	.0025	71.5	3.312	M	.0870	-.0532	3.039
34	1.30	167	.0254	.0010	71.5	3.312	M	.1292	-.0532	3.039
42	3.05	164	.0635	.0025	71.5	3.312	M	.0333	-.0405	3.039
54	5.10	168	.0889	.0035	71.5	3.312	M	.0109	-.0405	3.039
60	5.25	169	.0889	.0035	71.5	3.312	M	.0109	-.0405	3.039

4P2A Round/.005/M/86.0

Time (sec)	Yaw (deg)	ϕ_γ (deg)	Orbit (mm)	Orbit (in)	Spin (Hz)	Coning (Hz)	Wt Pos	Growth Rates (1/s) exp	Growth Rates (1/s) tare	Tare Con (Hz)
10	.25	133	.0762	.0030	86.0	3.868	M	.2549	-.0096	3.671
18	1.50	156	.0381	.0015	86.0	3.868	M	.1658	-.0096	3.671
22	2.75	156	.0508	.0020	86.0	3.868	M	.0680	-.0096	3.671
26	3.75	168	.0762	.0030	86.0	3.868	M	.0680	-.0096	3.671
29	4.50	178	.0711	.0028	86.0	3.868	M	.0680	-.0096	3.671

5P1A Round/.005/B/75.0

Time (sec)	Yaw (deg)	ϕ_γ (deg)	Orbit (mm)	Orbit (in)	Spin (Hz)	Coning (Hz)	Wt Pos	Growth Rates (1/s) exp	Growth Rates (1/s) tare	Tare Con (Hz)
11	.225	175	.0051	.0002	75.0	3.578	B	.1383	-.0096	3.585
14	.365	184	.0076	.0003	75.0	3.578	B	.1383	-.0096	3.585
22	.550	148	.0102	.0004	75.0	3.578	B	.2078	-.0096	3.585
30	2.850	163	.0610	.0024	75.0	3.578	B	.1120	-.0096	3.585
39	4.600	173	.0940	.0037	75.0	3.578	B	.0221	-.0096	3.585

5P2 Round/.005/B/85.0

Time (sec)	Yaw (deg)	ϕ_γ (deg)	Orbit (mm)	Orbit (in)	Spin (Hz)	Coning (Hz)	Wt Pos	Growth Rates (1/s) exp	Growth Rates (1/s) tare	Tare Con (Hz)
13	1.50	150	.0457	.0018	85.0	4.033	B	.1960	-.0096	4.058
17	2.30	155	.0559	.0022	85.0	4.033	B	.0833	-.0096	4.058
25	4.15	172	.0813	.0032	85.0	4.033	B	.0306	-.0096	4.058
29	4.90	171	.0864	.0034	85.0	4.033	B	.0306	-.0096	4.058

6P1 Round/.005/T/75.0

Time	Yaw	ϕ_Y	Orbit		Spin	Coning	Wt	Growth Rates (1/s)		Tare Con
(sec)	(deg)	(deg)	(mm)	(in)	(Hz)	(Hz)	Pos	exp	tare	(Hz)
5	0.26	150	.0025	.0001	75.0	3.145	T	.1163	-.0514	2.976
17	1.00	180	.0559	.0022	75.0	3.145	T	.1163	-.0514	2.976
34	1.75	159	.0406	.0016	75.0	3.145	T	.0743	-.0514	2.976
45	4.50	168	.0762	.0030	75.0	3.145	T	.0311	-.0514	2.976

6P2 Round/.005/T/85.0

Time	Yaw	ϕ_Y	Orbit		Spin	Coning	Wt	Growth Rates (1/s)		Tare Con
(sec)	(deg)	(deg)	(mm)	(in)	(Hz)	(Hz)	Pos	exp	tare	(Hz)
15	0.45	170	.0076	.0003	85.0	3.454	T	.2392	-.0469	3.378
19	1.15	138	.0305	.0012	85.0	3.454	T	.1259	-.0469	3.378
27	2.75	153	.0584	.0023	85.0	3.454	T	.0526	-.0469	3.378
30	3.50	168	.0660	.0026	85.0	3.454	T	.0526	-.0469	3.378

8P1A2 Round/.010/B/62.0

Time	Yaw	ϕ_Y	Orbit		Spin	Coning	Wt	Growth Rates (1/s)		Tare Con
(sec)	(deg)	(deg)	(mm)	(in)	(Hz)	(Hz)	Pos	exp	tare	(Hz)
10	2.90	161	.0635	.0025	62.0	3.141	B	.1216	-.0153	3.002
16	4.60	177	.0965	.0038	62.0	3.141	B	.0707	-.0153	3.002
20	5.70	167	.1473	.0058	62.0	3.141	B	.0183	-.0153	3.002
28	6.70	168	.1702	.0067	62.0	3.141	B	.0183	-.0153	3.002

8P2A2 Round/.010/B/70.0

Time	Yaw	ϕ_Y	Orbit		Spin	Coning	Wt	Growth Rates (1/s)		Tare Con
(sec)	(deg)	(deg)	(mm)	(in)	(Hz)	(Hz)	Pos	exp	tare	(Hz)
5	0.15	92	.0102	.0004	70.0	3.551	B	.0463	-.0096	3.373
45	0.95	134	.0254	.0010	70.0	3.551	B	.0678	-.0096	3.373
51	2.40	132	.0635	.0025	70.0	3.551	B	.2573	-.0096	3.373
60	5.70	167	.1626	.0064	70.0	3.551	B	.0886	-.0096	3.373

9P12 Round/.010/M/62.0

Time	Yaw	ϕ_Y	Orbit		Spin	Coning	Wt	Growth Rates (1/s)		Tare Con
(sec)	(deg)	(deg)	(mm)	(in)	(Hz)	(Hz)	Pos	exp	tare	(Hz)
5	2.00	149	.0457	.0018	62.0	2.886	M	.1177	-.0618	2.756
15	4.75	155	.1067	.0042	62.0	2.886	M	.0449	-.0618	2.756
21	5.20	165	.1295	.0051	62.0	2.886	M	.0289	-.0618	2.756
28	6.50	163	.1549	.0061	62.0	2.886	M	.0289	-.0618	2.756

9P22 Round/.010/M/70.0

Time (sec)	Yaw (deg)	ϕ_Y (deg)	Orbit (mm)	Orbit (in)	Spin (Hz)	Coning (Hz)	Wt Pos	Growth Rates (1/s) exp	Growth Rates (1/s) tare	Tare Con (Hz)
15	2.15	116	.0127	.0005	70.0	3.075	M	.1125	-.0532	3.093
30	2.00	145	.0025	.0001	70.0	3.075	M	.1125	-.0532	3.093
44	6.50	162	.1803	.0071	70.0	3.075	M	.0259	-.0532	3.093
46	6.60	168	.1702	.0067	70.0	3.075	M	.0259	-.0532	3.093

9P32 Round/.010/M/80.0

Time (sec)	Yaw (deg)	ϕ_Y (deg)	Orbit (mm)	Orbit (in)	Spin (Hz)	Coning (Hz)	Wt Pos	Growth Rates (1/s) exp	Growth Rates (1/s) tare	Tare Con (Hz)
10	0.45	145	.0203	.0008	80.0	4.652	M	.1484	-.0524	3.628
20	4.50	166	.1981	.0078	80.0	4.652	M	.0278	-.0524	3.628
25	5.10	170	.1956	.0077	80.0	4.652	M	.0278	-.0524	3.628
30	6.20	169	.1981	.0078	80.0	4.652	M	.0278	-.0524	3.628

10P32 Round/.015/M/65.0

Time (sec)	Yaw (deg)	ϕ_Y (deg)	Orbit (mm)	Orbit (in)	Spin (Hz)	Coning (Hz)	Wt Pos	Growth Rates (1/s) exp	Growth Rates (1/s) tare	Tare Con (Hz)
18	0.40	106	.0203	.0008	65.0	2.865	M	.1198	-.0661	2.798
25	0.80	113	.0635	.0025	65.0	2.865	M	.1198	-.0661	2.798
28	1.25	126	.0559	.0022	65.0	2.865	M	.1198	-.0661	2.798
32	1.60	145	.0381	.0015	65.0	2.865	M	.1166	-.0661	2.798

APPENDIX D-II

OCTAGON SHAFT RAW DATA

APPENDIX D-II. OCTAGON SHAFT RAW DATA

13P11 Octagon/.005/B/75.0

Time (sec)	Yaw (deg)	ϕ_Y (degs)	Orbit (mm)	Orbit (in)	Spin (Hz)	Coning (Hz)	Wt Pos	Growth Rates (1/s) exp	Growth Rates (1/s) tare	Tare Con (Hz)
21	0.60	65	.1270	.0050	75.0	3.584	B	.1150	-.0096	3.599
34	1.20	50	.1067	.0042	75.0	3.584	B	.1728	-.0096	3.599
38	2.50	17	.1219	.0048	75.0	3.584	B	.1728	-.0096	3.599
41	3.65	11	.1219	.0048	75.0	3.584	B	.0758	-.0096	3.599
45	5.00	00	.1168	.0046	75.0	3.584	B	.0758	-.0096	3.599

13P12 Octagon/.005/B/75.0

Time (sec)	Yaw (deg)	ϕ_Y (degs)	Orbit (mm)	Orbit (in)	Spin (Hz)	Coning (Hz)	Wt Pos	Growth Rates (1/s) exp	Growth Rates (1/s) tare	Tare Con (Hz)
21	0.60	38	.0051	.0002	75.0	3.584	B	.1150	-.0096	3.599
34	1.20	63	.0102	.0004	75.0	3.584	B	.1728	-.0096	3.599
38	2.50	58	.0305	.0012	75.0	3.584	B	.1728	-.0096	3.599
41	3.65	60	.0356	.0014	75.0	3.584	B	.0758	-.0096	3.599
45	5.00	49	.0127	.0005	75.0	3.584	B	.0758	-.0096	3.599

13P2A1 Octagon/.005/B/85.0

Time (sec)	Yaw (deg)	ϕ_Y (degs)	Orbit (mm)	Orbit (in)	Spin (Hz)	Coning (Hz)	Wt Pos	Growth Rates (1/s) exp	Growth Rates (1/s) tare	Tare Con (Hz)
15	.27	-18	.1118	.0044	85.0	4.379	B	.0304	-.0096	4.058
23	1.30	24	.1067	.0042	85.0	4.379	B	.2227	-.0096	4.058
31	3.85	8	.1194	.0047	85.0	4.379	B	.0870	-.0096	4.058
39	5.20	8	.1143	.0045	85.0	4.379	B	.0172	-.0096	4.058
47	5.20	6	.1143	.0045	85.0	4.379	B	.0172	-.0096	4.058
56	0.00	4	.1194	.0047	85.0	4.379	B	.0172	-.0096	4.058

14P21 Octagon/.005/M/85.0

Time (sec)	Yaw (deg)	ϕ_Y (degs)	Orbit (mm)	Orbit (in)	Spin (Hz)	Coning (Hz)	Wt Pos	Growth Rates (1/s) exp	Growth Rates (1/s) tare	Tare Con (Hz)
15	.54	27	.1168	.0046	85.0	3.810	M	.1579	-.0096	3.295
20	1.40	24	.1067	.0042	85.0	3.810	M	.1871	-.0096	3.295
25	2.75	16	.1194	.0047	85.0	3.810	M	.1712	-.0096	3.295
35	6.00	13	.1194	.0047	85.0	3.810	M	.0307	-.0096	3.295
45	7.40	12	.1194	.0047	85.0	3.810	M	.0148	-.0096	3.295

15P2A Octagon/.005/T/85.0

Time (sec)	Yaw (deg)	ϕ_Y (degs)	Orbit (mm)	Orbit (in)	Spin (Hz)	Coning (Hz)	Wt Pos	Growth Rates (1/s) exp	Growth Rates (1/s) tare	Tare Con (Hz)
23	0.53	34	.1194	.0047	85.0	3.268	T	.0306	-.0021	3.378
30	1.10	37	.1194	.0047	85.0	3.268	T	.0459	-.0021	3.378
38	1.75	35	.1168	.0046	85.0	3.268	T	.0796	-.0021	3.378
46	3.85	26	.1067	.0042	85.0	3.268	T	.0796	-.0021	3.378
55	7.20	26	.1143	.0045	85.0	3.268	T	.0000	-.0021	3.378
63	9.20	25	.1270	.0050	85.0	3.268	T	.0000	-.0021	3.378

APPENDIX E-I

REDUCED DATA FOR ROUND SHAFTS

APPENDIX E-I. REDUCED DATA FOR ROUND SHAFTS

4PO Round/.005/M/71.5

Time (sec)	Yaw Angle (deg)	Yaw Growth Rate x 10^3 Theory	Yaw Growth Rate x 10^3 Experiment	Fast Prec Freq/Tare Freq Theory	Fast Prec Freq/Tare Freq Experiment
23*	0.465	0.162	0.055	1.093	1.089
34*	1.300	0.070	0.199	1.013	1.089
42	3.050	0.215	0.189	1.014	1.089
54	5.100	0.227	0.220	1.011	1.089
60	5.250	0.208	0.226	1.011	1.089

4P2A Round/.005/M/86.0

Time (sec)	Yaw Angle (deg)	Yaw Growth Rate x 10^3 Theory	Yaw Growth Rate x 10^3 Experiment	Fast Prec Freq/Tare Freq Theory	Fast Prec Freq/Tare Freq Experiment
10*	0.250	0.723	0.047	1.154	1.053
18	1.500	0.201	0.189	1.017	1.053
22	2.750	0.268	0.153	1.012	1.053
26	3.750	0.205	0.209	1.014	1.053
29	4.500	0.032	0.251	1.011	1.054

5P1A Round/.005/B/75.0

Time (sec)	Yaw Angle (deg)	Yaw Growth Rate x 10^3 Theory	Yaw Growth Rate x 10^3 Experiment	Fast Prec Freq/Tare Freq Theory	Fast Prec Freq/Tare Freq Experiment
11*	0.225	0.006	0.026	1.017	0.998
14*	0.365	-0.007	0.042	1.016	0.998
22*	0.550	0.075	0.093	1.012	0.998
30	2.850	0.248	0.269	1.016	0.998
39	4.600	0.159	0.113	1.016	0.998

5P2 Round/.005/B/85.0

Time (sec)	Yaw Angle (deg)	Yaw Growth Rate x 10^3 Theory	Yaw Growth Rate x 10^3 Experiment	Fast Prec Freq/Tare Freq Theory	Fast Prec Freq/Tare Freq Experiment
13*	1.500	0.321	0.212	1.021	0.993
17*	2.300	0.332	0.147	1.017	0.993
25	4.150	0.159	0.115	1.015	0.993
29	4.900	0.190	0.136	1.014	0.993

6P1 Round/.005/T/75.0

Time (sec)	Yaw Angle (deg)	Yaw Growth Rates x 10^3 Theory	Yaw Growth Rates x 10^3 Experiment	Fast Prec Freq/Tare Freq Theory	Fast Prec Freq/Tare Freq Experiment
5*	0.260	0.016	0.039	1.006	1.056
17*	1.000	0.000	0.148	1.040	1.056
34	1.750	0.184	0.194	1.015	1.056
45	4.500	0.200	0.328	1.012	1.056

6P2 Round/.005/T/85.0

Time (sec)	Yaw Angle (deg)	Yaw Growth Rates x 10^3 Theory	Yaw Growth Rates x 10^3 Experiment	Fast Prec Freq/Tare Freq Theory	Fast Prec Freq/Tare Freq Experiment
15*	0.450	0.018	0.104	1.012	1.022
19*	1.150	0.274	0.160	1.015	1.022
27	2.750	0.357	0.220	1.014	1.022
30	3.500	0.185	0.280	1.014	1.022

8P1A2 Round/.010/B/62.0

Time (sec)	Yaw Angle (deg)	Yaw Growth Rates x 10^3 Theory	Yaw Growth Rates x 10^3 Experiment	Fast Prec Freq/Tare Freq Theory	Fast Prec Freq/Tare Freq Experiment
10*	2.900	0.255	0.351	1.014	1.046
16	4.600	0.268	0.350	1.014	1.046
20	5.700	0.409	0.169	1.017	1.046
28	6.700	0.437	0.199	1.017	1.046

8P2A2 Round/.010/B/70.0

Time (sec)	Yaw Angle (deg)	Yaw Growth Rates x 10^3 Theory	Yaw Growth Rates x 10^3 Experiment	Fast Prec Freq/Tare Freq Theory	Fast Prec Freq/Tare Freq Experiment
5	0.150	0.125	0.007	1.001	1.052
45	0.950	0.225	0.058	1.013	1.052
51	2.400	0.582	0.501	1.012	1.052
60	5.700	0.451	0.438	1.019	1.052

9P12 Round/.010/M/62.0

Time (sec)	Yaw Angle (deg)	Yaw Growth Rates x 10^3 Theory	Yaw Growth Rates x 10^3 Experiment	Fast Prec Freq/Tare Freq Theory	Fast Prec Freq/Tare Freq Experiment
5*	2.000	0.286	0.346	1.013	1.047
15*	4.750	0.548	0.488	1.014	1.047
21	5.200	0.407	0.454	1.016	1.047
28	6.500	0.550	0.567	1.015	1.047

9P22 Round/.010/M/70.0

Time (sec)	Yaw Angle (deg)	Yaw Growth Rates x 10^3 Theory	Yaw Growth Rates x 10^3 Experiment	Fast Prec Freq/Tare Freq Theory	Fast Prec Freq/Tare Freq Experiment
15*	2.150	0.155	0.322	1.002	0.994
30*	2.000	0.198	0.299	1.008	0.994
44	6.500	0.757	0.464	1.020	0.994
46	6.600	0.480	0.472	1.019	0.994

9P32		Round/.010/M/80.0			
Time (sec)	Yaw Angle (deg)	Yaw Growth Rates x 10^3 Theory	Yaw Growth Rates x 10^3 Experiment	Fast Prec Freq/Tare Freq Theory	Fast Prec Freq/Tare Freq Experiment
10*	0.450	0.096	0.054	1.017	1.282
20	4.500	0.394	0.215	1.020	1.282
25	5.100	0.279	0.244	1.017	1.282
30	6.200	0.311	0.297	1.014	1.282

10P32		Round/.015/M/65.0			
Time (sec)	Yaw Angle (deg)	Yaw Growth Rates x 10^3 Theory	Yaw Growth Rates x 10^3 Experiment	Fast Prec Freq/Tare Freq Theory	Fast Prec Freq/Tare Freq Experiment
18*	0.400	0.263	0.072	1.010	1.023
25*	0.800	0.788	0.144	1.023	1.023
28*	1.250	0.610	0.225	1.020	1.023
32*	1.600	0.295	0.283	1.015	1.023

*Conditions and assumptions of theory not satisfied.

APPENDIX E-II

REDUCED DATA FOR OCTAGON SHAFTS

APPENDIX E-II. REDUCED DATA FOR OCTAGON SHAFTS

13P11 Octagon/.005/B/75.0

Time (sec)	Yaw Angle (deg)	Yaw Growth Rates x 10^3 Theory	Yaw Growth Rates x 10^3 Experiment	Fast Prec Freq/Tare Freq Theory	Fast Prec Freq/Tare Freq Experiment
21*	0.600	1.313	0.058	0.941	0.995
34*	1.200	0.951	0.170	0.961	0.995
38*	2.500	0.408	0.353	0.969	0.995
41*	3.650	0.266	0.242	0.978	0.995
45*	5.000	0.000	0.331	0.984	0.995

13P12 Octagon/.005/B/75.0

Time (sec)	Yaw Angle (deg)	Yaw Growth Rates x 10^3 Theory	Yaw Growth Rates x 10^3 Experiment	Fast Prec Freq/Tare Freq Theory	Fast Prec Freq/Tare Freq Experiment
21*	0.600	0.043	0.058	0.994	0.995
34*	1.200	0.125	0.170	0.996	0.995
38*	2.500	0.358	0.353	0.994	0.995
41*	3.650	0.426	0.242	0.996	0.995
45*	5.000	0.133	0.331	0.998	0.995

13P2A1 Octagon/.005/B/85.0

Time (sec)	Yaw Angle (deg)	Yaw Growth Rates x 10^3 Theory	Yaw Growth Rates x 10^3 Experiment	Fast Prec Freq/Tare Freq Theory	Fast Prec Freq/Tare Freq Experiment
15*	0.270	-0.343	0.007	0.776	1.079
23*	1.300	0.436	0.192	0.956	1.079
31*	3.850	0.164	0.236	0.982	1.079
47*	5.200	0.120	0.088	0.987	1.079

14P21 Octagon/.005/M/85.0

Time (sec)	Yaw Angle (deg)	Yaw Growth Rates x 10^3 Theory	Yaw Growth Rates x 10^3 Experiment	Fast Prec Freq/Tare Freq Theory	Fast Prec Freq/Tare Freq Experiment
15*	0.540	0.576	0.066	0.880	1.156
20*	1.400	0.476	0.201	0.956	1.156
25*	2.750	0.355	0.362	0.974	1.156
35*	6.000	0.290	0.176	0.988	1.156
45*	7.400	0.268	0.132	0.990	1.156

15P2A1 Octagon/.005/T/85.0

Time (sec)	Yaw Angle (deg)	Yaw Growth Rates x 10^3 Theory	Yaw Growth Rates x 10^3 Experiment	Fast Prec Freq/Tare Freq Theory	Fast Prec Freq/Tare Freq Experiment
23*	0.530	0.829	0.015	0.867	0.967
30*	1.100	0.892	0.045	0.938	0.967
38*	1.750	0.837	0.122	0.960	0.967
46*	3.850	0.581	0.267	0.982	0.967

*Conditions and assumptions of theory not satisfied.

DISTRIBUTION LIST

No. of Copies	Organization
12	Administrator Defense Technical Information Center ATTN: DTIC-FDAC Cameron Station, Bldg. 5 Alexandria, VA 22304-6145
1	HQDA DAMA-ART-M Washington, DC 20310
1	Commander US Army Materiel Command ATTN: AMCDRA-ST 5001 Eisenhower Avenue Alexandria, VA 22333-0001
1	Commander US Army ARDEC ATTN: SMCAR-TDC Dover, NJ 07801-5001
1	Commander U.S. Armament RD&E Center US Army AMCCOM ATTN: SMCAR-MSI Dover, NJ 07801-5001
1	Commander U.S. Armament RD&E Center US Army AMCCOM ATTN: SMCAR-LC Dover, NJ 07801-5001
1	Commander U.S. Armament RD&E Center US Army AMCCOM ATTN: SMCAR-CAWS-AM Mr. DellaTerga Dover, NJ 07801-5001
1	OPM Nuclear ATTN: AMCPM-NUC COL. W. P. Farmer Dover, NJ 07801-5001
1	AFWL/SUL Kirtland AFB,NM 87117-6008

No. of Copies	Organization
4	Commander U.S. Armament RD&E Center US Army AMCCOM ATTN: SMCAR-AET-A Mr. D. Mertz Mr. A. Loeb SMCAR-AET Mr. F. Scerbo Mr. J. Bera Dover, NJ 07801-5001
1	Commander US Army Armament, Munitions and Chemical Command ATTN: AMSMC-IMP-L Rock Island, IL 61299-7300
1	Commander U.S. AMCCOM ARDEC CCAC Benet Weapons Laboratory ATTN: SMCAR-CCB-TL Watervliet, NY 12189-4050
1	Commander US Army Aviation Systems Command ATTN: AMSAV-ES 4300 Goodfellow Blvd St. Louis, MO 63120-1798
1	Director US Army Aviation Research and Technology Activity Ames Research Center Moffett Field, CA 94035-1099
1	Commander US Army Communications - Electronics Command ATTN: AMSEL-ED Fort Monmouth, NJ 07703-5000
1	Commander CECOM R&D Technical Library ATTN: AMSEL-IM-L, (Reports Section) B. 2700 Fort Monmouth, NJ 07703-5000

DISTRIBUTION LIST

No. of Copies	Organization
10	C. I. A. OIC/DB/Standard GE47 HQ Washington, DC 20505
1	Commandant US Army Infantry School ATTN: ATSH-CD-CS-OR Fort Benning, GA 31905-5400
1	Commander US Army Missile Command Research Development and Engineering Center ATTN: AMSMI-RD Redstone Arsenal, AL 35898-5230
1	Commander US Army Missile Command ATTN: AMSMI-RDK, Mr. R. Deep Redstone Arsenal, AL 35898-5230
1	Director US Army Missile and Space Intelligence Center ATTN: AIAMS-YDL Redstone Arsenal, AL 35898-5500
1	Commander US Army Tank Automotive Command ATTN: AMSTA-TSL Warren, MI 48397-5000
1	Director US Army TRADOC Analysis Center ATTN: ATOR-TSL White Sands Missile Range NM 88002-5502
1	Commander US Army Development & Employment Agency ATTN: MODE-ORO Fort Lewis, WA 98433-5000
1	Commandant US Army Field Artillery School ATTN: ATSF-GD Fort Sill, OK 73503

No. of Copies	Organization
1	Director National Aeronautics and Space Administration Langley Research Center ATTN: Tech Library Langley Station Hampton, VA 23365
1	Director US Army Field Artillery Board ATTN: ATZR-BDW Fort Sill, OK 73503
1	Commander US Army Dugway Proving Ground ATTN: STEDP-MT Mr. G. C. Travers Dugway, UT 84022
1	Commander US Army Yuma Proving Ground ATTN: STEYP-MTW Yuma, AZ 85365-9103
2	Director Sandia National Laboratories ATTN: Dr. W. Oberkampf Dr. W. P. Wolfe Division 1636 Albuquerque, NM 87185
1	AFATL/DLODL (Tech Info Center) Eglin AFB, FL 32542-5438
2	Raytheon Company Hartwell Road ATTN: Mr. V.A.Grosso Bedford, MA 01730
1	Martin-Marietta Corporation ATTN: S.H. Maslen 1450 S. Rolling Road Baltimore, MD 21227
1	Carco Electronics 195 Constitution Drive Menlo Park, CA 94025

DISTRIBUTION LIST

No. of Copies	Organization
1	Aerospace Corporation Aero-Engineering Subdivision ATTN: Walter F. Reddall El Segundo, CA 90245
1	Commander Naval Surface Weapons Center ATTN: Dr. W. Yanta Aerodynamics Branch K-24, Building 402-12 White Oak Laboratory Silver Spring, MD 20910
1	Director National Aeronautics and Space Administration Marshall Space Flight Center ATTN: Dr. W. W. Fowlis Huntsville, AL 35812
1	Director National Aeronautics and Space Administration Ames Research Center ATTN: Dr. T. Steger Moffett Field, CA 94035
1	Calspan Corporation ATTN: W. Rae P.O. Box 400 Buffalo, NY 14225
2	Rockwell International Science Center ATTN: Dr. V. Shankar Dr. S. Chakravarthy 1049 Camino Dos Rios Thousand Oaks, CA 91360
1	University of Santa Clara Department of Physics ATTN: R. Greeley Santa Clara, CA 95053
1	Arizona State University Department of Mechanical and Energy Systems Engineering ATTN: G.P. Neitzel Tempe, AZ 85281

No. of Copies	Organization
1	Massachusetts Institute of Technology ATTN: H. Greenspan 77 Massachusetts Avenue Cambridge, MA 02139
1	North Carolina State University Mechanical and Aerospace Engineering Department ATTN: F.F. DeJarnette Raleigh, NC 27607
1	Northwestern University Department of Engineering Science and Applied Mathematics ATTN: Dr. S.H. Davis Evanston, IL 60201
1	University of Colorado Department of Astro-Geophysics ATTN: E.R. Benton Boulder, CO 80302
2	Univeristy of Maryland ATTN: W. Melnik J.D. Anderson College Park, MD 20740
1	University of Maryland - Baltimore County Department of Mathematics ATTN: Dr. Y.M. Lynn 5401 Wilkens Avenue Baltimore, MD 21228
1	Rensselaer Polytechnic Institute Department of Math Sciences Troy, NY 12181
1	University of Tennessee Department of Physics ATTN: Tech. Library Knoxville, TN 37916

DISTRIBUTION LIST

No. of Copies	Organization
2	Director Lawrence Livermore National Laboratory ATTN: Mail Code L-35 Mr. T. Morgan Mr. R. Cornell P.O. Box 808 Livermore, CA 94550
1	University of Wisconsin-Madison Mathematics Research Center ATTN: Dr. John Strikwerda 610 Walnut Street Madison, WI 53706
2	Virginia Polytechnic Institute and State University Department of Aerospace Engineering ATTN: Tech Library Dr. Thorwald Herbert Blacksburg, VA 24061
2	University of Southern California Department of Aerospace Engineering ATTN: T. Maxworthy P. Weidman Los Angeles, CA 90007
1	University of Virginia Department of Mechanical Aerospace Engineering ATTN: W. E. Scott Charlottesville, VA 22904
1	University of Notre Dame Aerospace and Mechanical Engineering Department ATTN: Prof. Thomas J. Mueller South Bend, Indiana 46556
1	Commander David W. Taylor Naval Ship Research and Development Center ATTN: Dr. William K. Blake Bethesda, MD 20084-5000
1	Illinois Institute of Technology ATTN: Mr. Simon Rosenblat 3300 South Federal Chicago, Illinois 60616

Aberdeen Proving Ground

Director, USAMSAA
ATTN: AMXSY-D
AMXSY-RA, R. Scungio

Commander, USATECOM
ATTN: AMSTE-SI-F
AMSTE-TE-F, W. Vomocil

PM-SMOKE, Bldg. 324
ATTN: AMCPM-SMK-M
Mr. J. Callahan

Cdr, CRDC, AMCCOM
ATTN: SMCCR-MU
Mr. W. Dee
Mr. C. Hughes
Mr. F. Dagostin
Mr. D. Bromley
Mr. C. Jeffers
Mr. L. Shaft
ATTN: SMCCR-RSP-A
Mr. Miles Miller
ATTN: SMCCR-SPS-IL
SMCCR-RSP-A
SMCCR-MU

USER EVALUATION SHEET/CHANGE OF ADDRESS

This Laboratory undertakes a continuing effort to improve the quality of the reports it publishes. Your comments/answers to the items/questions below will aid us in our efforts.

1. BRL Report Number________________________Date of Report__________

2. Date Report Received____

3. Does this report satisfy a need? (Comment on purpose, related project, or other area of interest for which the report will be used.)__________

4. How specifically, is the report being used? (Information source, design data, procedure, source of ideas, etc.)______________________________

5. Has the information in this report led to any quantitative savings as far as man-hours or dollars saved, operating costs avoided or efficiencies achieved, etc? If so, please elaborate.______________________________________

6. General Comments. What do you think should be changed to improve future reports? (Indicate changes to organization, technical content, format, etc.)

CURRENT ADDRESS

Name

Organization

Address

City, State, Zip

7. If indicating a Change of Address or Address Correction, please provide the New or Correct Address in Block 6 above and the Old or Incorrect address below.

OLD ADDRESS

Name

Organization

Address

City, State, Zip

(Remove this sheet, fold as indicated, staple or tape closed, and mail.)

— — — — — — — — — FOLD HERE — — — — — — — — — —

Director
US Army Ballistic Research Laboratory
ATTN: DRXBR-OD-ST
Aberdeen Proving Ground, MD 21005-5066

NO POSTAGE
NECESSARY
IF MAILED
IN THE
UNITED STATES

OFFICIAL BUSINESS
PENALTY FOR PRIVATE USE, $300

BUSINESS REPLY MAIL
FIRST CLASS PERMIT NO 12062 WASHINGTON,DC

POSTAGE WILL BE PAID BY DEPARTMENT OF THE ARMY

Director
US Army Ballistic Research Laboratory
ATTN: DRXBR-OD-ST
Aberdeen Proving Ground, MD 21005-9989

— — — — — — — — — FOLD HERE — — — — — — — — — —